UNIVERSITÀ DEGLI STUDI DI TRIESTE

XXX CICLO DEL DOTTORATO DI RICERCA IN NANOTECNOLOGIE

NANOOPTOMECHANICAL SILICON DEVICES FOR SENSING APPLICATIONS

Settore scientifico-disciplinare: **FIS/03**

DOTTORANDO
SILVIO MARIO LUCIANO GRECO

COORDINATORE
PROF. LUCIA PASQUATO

SUPERVISORE DI TESI
PROF. MARCO LAZZARINO

TUTOR DI TESI
DR. SIMONE DAL ZILIO

ANNO ACCADEMICO 2016/2017

Abstract

The interest in the field of plasmonics is growing steadily in the last two decades; from the ability to transmit and receive information at very high speed with greatly reduced losses to the enhancement of very weak signals for chemical and biological analysis, its range of applicability is boundless. The understanding of plasmonic phenomena is also increasing, and with this comes the ability to tune plasmonic properties to the designer's will. Among other approaches, the use of MicroElectroMechanical Systems (MEMS) for the modulation of plasmonic properties has been recently reported in literature, but no practical application, such as Raman spectroscopy, has been reported beside the field of Tip-Enhanced Raman Spectroscopy, a powerful approach that demonstrated nanometric chemical spatial resolution, but which remains confined the research laboratory benches due to its intrinsic experimental complexity.

In this project, we propose to explore the coupling between mechanical and plasmonic properties of micro and nanosensors in order to realize a mechanical resonator capable of turning on and off a frequency modulated hot spot.

Different strategies have been tried to achieve the desired result: the first version of the optomechanical device was based on a vertical resonator (pillar) put in close proximity with a steady structure, 100 nm apart from each other. The devices are fabricated using electron-beam lithography for the high resolution required for the sub-micron gap and ICP-RIE to obtain an inverted tapered structure of the pillar walls; the evaporation of a gold layer on top of the devices ensures a plasmonic activity of the upper surface during the actuation of the devices. Optical lever techniques and Rayleigh scattering mapping have been used for the mechanical characterization and the onset of an impact oscillation condition is discussed. The Raman scattering intensification due to the formation of a plasmonic hot spot in the contact region has been studied functionalizing the devices with pentacene and an enhancing factor for the Raman signal during actuation can be estimated. However, severe drawbacks have been identified in this configuration, since pillars tilt and bend nanometrically during the motion, causing the hot spots to be randomly localized along the gap and reducing their field enhancement capabilities.

The problems arisen with the first version of the device have been solved through the careful design of a new geometry: the vertical resonator has been changed into a horizontally-oscillating cantilever tuning the width-to-height ratio, and a tip has been added to the design for a well-defined contact point. This new device has been characterized using sample scanning confocal microscopy, both in its mechanical properties and in the surface distribution of the chosen Raman

dye, benzotriazole azo (BT-Azo), after the functionalization. Finally, the plasmonic behaviour has been investigated and the signal coming from the hot spot has been successfully isolated using a combination of polarization-dependent excitation light and lock-in deconvolution of the signal at higher harmonics, thus demonstrating the successful realization of a frequency modulated hot spot for Raman spectroscopy applications. This plasmomechanical resonating device with a well-defined hot spot location and precise resonant behaviour can allow synchronized excitation of delicate analytes to reduce power on the sample and increase the signal-to-noise ratio for molecules with small Raman cross-section.

As a side activity, a wire scanner sensor with nanofabricated bridges suspended over a wide window has been fabricated, for the characterization of high-energy electron or light beams. The test of this device has been performed at the BEAR beamline of the Elettra Synchrotron and in the FERMI FEL-1 Free-Electron Laser facility; the performances of this sensor have been proved to be comparable, when not superior, to those of the commercially available devices.

Index

Abstract 3

Index 5

Overview of the thesis 9

1 Plasmonic devices for SERS applications 11

1.1 Raman spectroscopy and SERS 11

1.1.1 Spectroscopy overview 11

1.1.2 Raman spectroscopy 12

1.1.3 Surface-Enhanced Raman Scattering principles 15

1.2 Principles of plasmonics 16

1.2.1 The Drude-Lorentz model for the dielectric function of metals 16

1.2.2 Surface plasmon polaritons and LSPR in single particles 19

1.2.3 Hot spots in coupled nanostructures 21

1.2.4 The effect of surface roughness 23

1.3 Hot spot control in SERS systems 24

1.3.1 Colloid-based substrates 24

1.3.2 Nanofabrication-based substrates 26

1.4 Dynamic control of plasmonic properties 27

1.4.1 Controlling plasmonic properties with MEMS 29

1.5 Objective of the research project 31

References 33

2 Fabrication and characterization of nanooptomechanical devices 38

2.1 Fabrication processes 38

2.1.1 Silicon and SOI wafers 39

2.1.2 Thin film deposition 40

2.1.3 Lithography 42

2.1.3.1 Optical lithography 42

2.1.3.2 Electron beam lithography 44

2.1.4 Lift-off 44

2.1.5 Wet and dry etching 45

2.1.6 Suspended structure release – supercritical point drying 48

2.2 Surface functionalization 48

2.2.1 Evaporation 48

2.2.2 Immersion and dip coating 49

2.3 Characterization methods 50

2.3.1 Morphological characterization of devices 51

2.3.2 Mechanical characterization of devices 52

2.4 Fabrication and functionalization protocols 56

2.4.1 Fabrication of the devices 57

2.4.2 Functionalization of the devices 58

2.4.3 Characterization of the devices 59

2.4.3.1 Mechanical characterization of the pillar device 59

2.4.3.2 Mechanical characterization of the cantilever device 61

2.4.3.3 Rayleigh and Raman measurements 63

References 65

3 A micromechanical switchable hot spot for SERS applications 67

3.1 Fabrication of the device 67

3.2 Mechanical characterization 68

3.2.1 Preliminary calculations and finite element analysis 68

3.2.2 Mechanical characterization in vacuum 69

3.2.3 Mechanical characterization in air 73

3.2.4 Metallic layer characterization 73

3.3 SERS effect detection ... 74

3.3.1 Effects of the laser polarization ... 78
3.3.2 Modulability of the enhancement ... 79
3.3.3 Signal enhancement evaluation ... 80

3.4 Critical points and proposed solutions ... 81
References ... 83

4 Optomechanical devices for frequency-modulated plasmonic hot spot ... 84

4.1 Finite-element modelling ... 84

4.1.1 Mechanical modelling ... 84
4.1.2 Plasmonic modelling ... 87

4.2 Fabrication of the devices ... 90
4.3 Preliminary characterization ... 92

4.3.1 Rayleigh scattering mapping ... 92
4.3.2 Mechanical characterization ... 93
4.3.3 BT-Azo dye film characterization ... 96

4.4 Dynamic mode mapping ... 99

4.4.1 Parallel and perpendicular polarization ... 99
4.4.2 Lock-in signal deconvolution ... 100
4.4.3 Hot spot localization ... 104

4.5 Signal enhancement evaluation ... 107
References ... 109

5 Design, fabrication and characterization of nanofabricated wire scanner ... 110

5.1 Project background ... 110
5.2 Nanofabrication process of the devices ... 112
5.3 Intra-undulator chamber measurements at FERMI Free-Electron Laser ... 116

5.3.1 Simulations of ionizing radiation emission ... 116
5.3.2 Experimental setup ... 117

5.3.3 Experimental results 118

5.4 Focal spot characterization at BEAR beamline 120

5.4.1 Experimental setup 120
5.4.2 Experimental results 121

References 126

Conclusions 128

Overview of the thesis

The intrinsic property of nanostructured noble metals, such as silver or gold, of squeezing and amplifying an electromagnetic field has been exploited to increase the number of Raman scattered photons; Surface-Enhanced Raman Scattering (SERS) is an emerging feature of nanostructured substrates of noble metals which, when properly excited, exhibit plasmonic properties and are capable of increasing the Raman scattering intensity. Recently, quasi static tuneable hot spots have been designed and applied to surface-enhanced Raman spectroscopy (SERS).

Micro and nanomechanical sensors are spreading far and wide into different fields of application: this is due mainly to the flexibility of their design, which enables them to be used for different purposes. Their design intrinsically encourages the integration on different platforms, ranging from optics to chemistry, even biology and medicine; a multidisciplinary approach often requires unconventional solutions, and a promising strategy often adopted in the MEMS field is the coupling of different device properties which concur to the final result. Optomechanical devices that allow the modulation of plasmonic properties through a mechanical resonator have already been realized, but no application to Raman spectroscopy has been reported yet.

A device with a well-defined hot spot location and behaviour has multiple advantages: the reduction of the energy on the sample by synchronizing the excitation with the hot spot formation appropriately; the increased contrast that can be obtained through the demodulation can further decrease the limit of detection in SERS analysis; and the increase of the signal-to-noise ratio with simple post-processing.

The aim of the research work presented in this thesis is the realization of a microelectromechanical device with embedded plasmonic properties, capable of realizing the frequency modulation of the hot spot formation easily, efficiently and in well-defined positions. All the steps of the experiments the have been performed in the laboratories of the CNR-IOM, AREA Science Park Basovizza, Trieste.

In the first chapter, an overview of the theory behind Raman scattering and SERS is given, with a description of the state-of-the-art substrates for SERS analysis. The methods presented in literature to control the hot spot formation are briefly reviewed along with the different applications of MEMS to the field of plasmonics. The advantages of this combination of electromechanical systems with plasmonics are presented and the objectives of this project are outlined.

The second chapter described all the techniques used in the different steps of this project. An overview of the fabrication and functionalization techniques is given, followed by the description of the methods for the mechanical and spectroscopic characterization of the plasmomechanical

devices. The instrumentation and the processes used in the experiments are also explained, with details about the setup used in optical mapping.

Since the target has been reached in two steps, *i.e.* with two different versions of the device, those are presented consequentially in chapter 3 and 4. Both devices share the same basic configuration: an oscillator is realized at a fixed distance from a steady structure and, when actuated in resonance condition, the motion brings the top surface of the resonator in contact with the top surface of the steady structure (both plasmon-active and functionalized with Raman reporters) to create the conditions for the hot spot formation along the separation gap.

The third chapter describes the results of the fabrication of the first version of the device, which employs a micropillar as resonating part. After its mechanical characterization and the discussion of the impact oscillator conditions when actuated in vacuum, the enhancement of the Raman signal is tested along the gap between the pillar and the steady structure. Where this improved Raman signal is found, an enhancement factor is estimated. In the last paragraph, the weak points of this device are critically discussed.

The fourth chapter illustrates the experiments on a device with a completely redesigned geometry, which aims at solving the problems arisen with the previous configuration. The results of the simulation of the mechanical and plasmonic behaviour are described and used to choose the best parameters for the fabrication, whose results are presented afterwards. The mechanical characterization and the mapping of the device using Rayleigh and Raman scattered light are described and discussed, followed by the detailed explanation of the principles, processes, and results of the higher harmonics deconvolution of the signal. Finally, when the hot spot location has been isolated, an enhancement factor for this device is calculated.

The last chapter is about the fabrication and testing of a nanomechanical sensor for the characterization of high-energy beams, like those found in a synchrotron or free-electron laser facility. This project, although outside the field of plasmonic MEMS, shares the same approach and techniques common to MEMS devices, and therefore is worth mentioning in this thesis. After a brief background about the beam profile sensors and the advantages of the nanofabrication approach to this problem, the process used to fabricate the sensor is explained and the experimental setups for synchrotron and FEL experiments are described. The preliminary calculations and the results of the experiments, performed in collaboration with two research groups, are presented and discussed in the last section.

1 Plasmonic devices for SERS applications

In this chapter, an overview of the basic principles of Raman spectroscopy is presented, along with the most common methods for signal enhancement, focusing in particular on SERS and plasmonics. After reviewing the different approaches towards the control of the plasmonic properties of complex systems, state-of-the-art MEMS technologies applied to plasmonics and SERS are illustrated. In the end of the chapter, the context and aim of the research project is explained.

1.1 Raman spectroscopy and SERS

1.1.1 Spectroscopy overview

Spectroscopy is the study of the dependence of a material property from energy. The most common forms of spectroscopy involve the interaction between matter and electromagnetic radiation; this interaction can have the form of absorption, scattering, or emission of radiations and, depending on the relationship between the incoming radiation and the property measured, can be used to study the atomic or molecular structure of materials. The energy of the incident electromagnetic radiation can trigger different processes in the matter under examination, giving different information about the sample and requiring different detection and analysis methods.

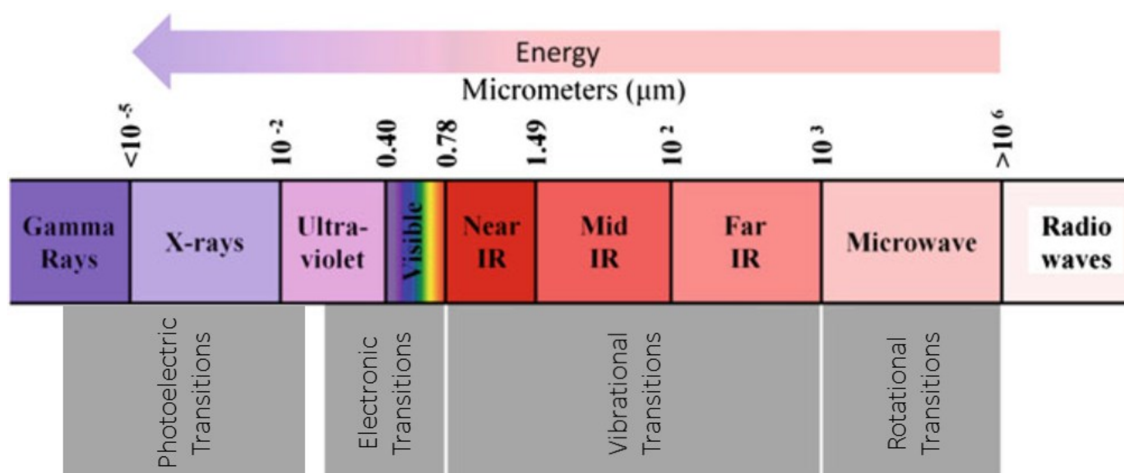

Figure 1.1 - Electromagnetic waves spectrum and atomic or molecular transitions. Different transitions are excited by electromagnetic radiation with different energy. Adapted from literature[1]*.*

Even though the electromagnetic spectrum is continuous, the transitions allowed for a material are not: the energy required for the transition from one state to another, independently from the kind of transition, has a well-defined value, *i.e.* the energy levels in a material are quantized. This

happens not only for photoelectric or electronic transitions, but also for vibrational and rotational transitions, each of them having its own characteristic energy. The transitions between two states are allowed only if a molecule is supplied with the exact amount of energy corresponding to the difference between the energies of the two involved states:

$$E_2 - E_1 = h\nu \quad \text{1.1}$$

E_1 and E_2 are the energies of the state 1 and 2 respectively, while h is the Planck's constant and ν the frequency of the incident radiation. The importance of this equation in spectroscopy is enormous: for example, when the absorption spectrum of a material illuminated with a broadband source is acquired, only the energy bands corresponding to allowed transitions will be absorbed, while the others will be transmitted without relevant changes in intensity. Since the energy of each transition is specific for an element, it is possible to gain important information about the atomic composition of a material. On the other side, emission spectroscopy is based on the complementary principle: the material is excited without the use of an electromagnetic radiation and the radiation emitted is then recorded. Usually, the emission and absorption spectrum of an element are complementary.

When more complex molecules or materials are involved, absorption or emission spectroscopies aren't usually able to provide many useful information; other spectroscopy techniques, such as Fourier-Transform Infrared (FT-IR) or Raman spectroscopy, can be used to probe the vibrational and rotational states of the molecules of interest, thus allowing the fingerprinting of a sample.

1.1.2 Raman spectroscopy

When a sample is exposed to a monochromatic or very narrow band light source, a small amount of the incident photons can be scattered. Most of those scattered photons maintain their original energy, so their wavelength is still the same, while others exchange part of their energy with the material. A tiny portion of them can exchange an amount of energy matching one of the allowed vibrational transitions and have different final energy, either higher or lower than the original one, carrying information about the material itself. In the quantum theory of radiation, these two different phenomena are compared to collisions and named accordingly, so the light which doesn't exchange energy with the material is *elastically* scattered, while the portion which exchanges energy undergoes *inelastic* scattering. The ratio between elastic and inelastic collision probability is typically in the order of $1:10^{-7}$ and this very small amount of inelastically scattered photons is called Raman scattered light. The amount of energy exchanged in these inelastic collisions is

coincident with vibrational and rotational transitions of the sample, thus making Raman scattering spectroscopy a vibrational and rotational spectroscopy technique.

The Raman scattered photons can be divided into two categories: those which have lower frequencies than the incident ones are called “Stokes”, while those which have higher frequencies are called “anti-Stokes” (Figure 1.2).

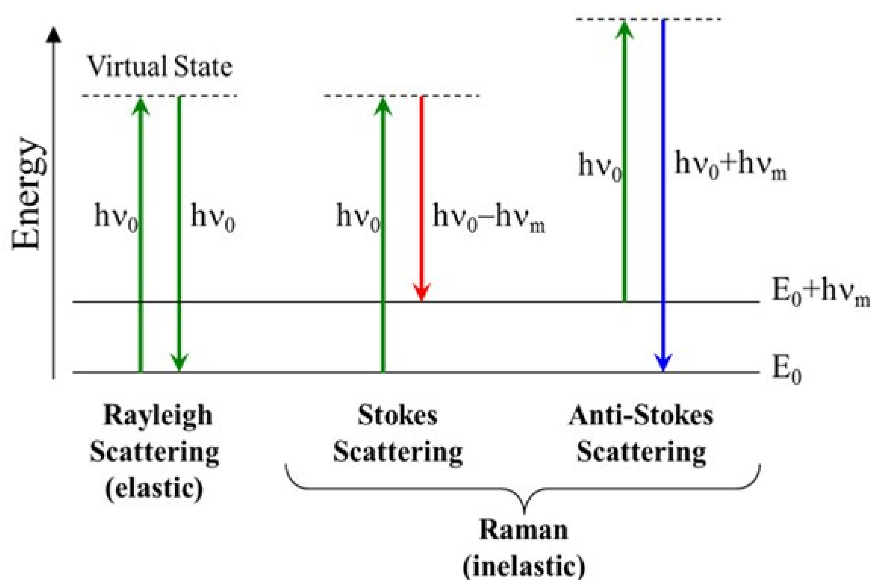

Figure 1.2 - Rayleigh and Raman scattering mechanism. The incident photon (green, energy hn0) excites a molecule to a non-stable virtual state, which can decay with the emission of a photon through elastic (Rayleigh) or inelastic (Raman) scattering.

When a molecule of polarizability α is exposed to an electromagnetic radiation of frequency ν, it experiences an induced dipole which oscillates according to the frequency of the incident radiation:

$$\mu = \alpha E = \alpha E_0 \sin(2\pi\nu t) \tag{1.2}$$

An oscillating dipole emits radiation with its same frequency ν: this is the basic principle behind the Rayleigh scattering. However, if the molecule is also experiencing other internal movements, such as vibrations or rotations, which change its polarizability over time, those oscillations can be superimposed on the oscillating dipole; by writing these changes of polarizability as

$$\alpha = \alpha_0 + q_0 \left(\frac{\partial\alpha}{\partial q}\right) \sin(2\pi\nu_{vr}t) = \alpha_0 + \beta \sin(2\pi\nu_{vr}t) \tag{1.3}$$

Where α_0 is the polarizability at equilibrium, ν_{vr} the vibrational or rotational motion frequency and $\beta = q_0 \left(\frac{\partial\alpha}{\partial q}\right)$ the change rate of the polarizability due to nuclear displacement during polarization; the linear dependence of the polarizability from the nuclear displacement is true for small

displacements, such as those imposed by an external excitation compatible with the energies involved in Raman scattering phenomena. Equation *1.2* can be rewritten as:

$$\mu = (\alpha_0 + \beta \sin(2\pi\nu_{vr}t))E_0 \sin(2\pi\nu t) \qquad 1.4$$

And, with simple trigonometry and expansion on Equation *1.4*, it becomes:

$$\mu = \alpha_0 E_0 \sin(2\pi\nu t) + \frac{1}{2}\beta E_0[\cos(\nu - \nu_{vr})t - \cos(\nu + \nu_{vr})t] \qquad 1.5$$

In this final form, the oscillation of the induced dipole in the material has a fundamental component of frequency ν and two more components of frequency $\nu - \nu_{vr}$ and $\nu + \nu_{vr}$: those represent Stokes and anti-Stokes Raman scattering, and therefore ν_{vr} can be also called Stokes shift. It is notable that, if the vibrational or rotational modes of interest have no effect on the polarizability of the molecule (*i.e.* $\beta = 0$), the Raman components of the oscillation are zero as well: this constitutes a selection rule for Raman spectroscopy, which requires the vibrational and rotational modes to have an effect on the polarizability of the material in order to be Raman-active. Even though both Stokes and anti-Stokes Raman scattering is possible, Stokes Raman scattering has a higher probability of happening because it involves the exchange of energy from the incident light to the sample, while anti-Stokes is less probable since the photons should receive energy from non-ground molecular states, less common at least in standard conditions of temperature, when the molecules under analysis are most commonly in their lowest vibrational state. In more rigorous terms, the ratio between the intensity of the Stokes and anti-Stokes scattering can be expressed using Boltzmann statistics[2]:

$$\frac{I(\nu + \nu_{vr})}{I(\nu - \nu_{vr})} = \exp\left(-\frac{h\nu_{vr}}{k_B T}\right) \qquad 1.6$$

All the symbols already used in previous equations have the same meaning explained before, while k_B is the Boltzmann's constant and T the absolute temperature.

A great concern about Raman scattering is the cross section of many analytes. The definition of scattering cross section can be derived from the ratio between the total scattered light (in terms of power) emitted from a molecule and the incident intensity as[3]:

$$\sigma_s = \frac{P_s}{I} = \frac{8\pi^3\bar{\alpha}^2}{3\epsilon_0^2\lambda^4} \qquad 1.7$$

$\bar{\alpha}$ is the mean polarizability of the analyte, ϵ_0 the dielectric constant of vacuum, and λ the wavelength of the incident light. While the contribution of the wavelength is at the fourth power,

$\bar{\alpha}$ is so small that strongly reduces the values of σ_S, thus explaining the low intensity of the Raman signal for many analytes. There are many different methods for enhancing the Raman signal, acting on different parameters influencing the Raman scattering; the most widespread, for its good performances and vast applicability, is SERS (Surface-Enhanced Raman Scattering).

1.1.3 Surface-Enhanced Raman Scattering principles

The amplification of the Raman signal in SERS is generated by the combined effect of two mechanisms: the electromagnetic field enhancement through the localization of optical fields in metallic nanostructures, and the chemical enhancement due to the increase of Raman cross section when the analyte is in contact with metal nanostructures[4].
The adsorption or close proximity of an analyte on a metal sample can change the polarizability of the molecule. The presence of atomic-scale roughness on a metal surface can create charge-transfer complexes between the metal and the molecule, as schematized in Figure 1.3. When the metal surface is excited by a photon, an electron of the metal can be excited (1) and then move to an electron affinity level of the adsorbed molecule (2). The electron then goes back to the metal (3) leaving the molecule in an excited state; this excitation event will now follow a different relaxation path from that of the non-adsorbed molecule leading to a net energy release when the electron is neutralized by a vacancy in the metal, and this energy can be released with the emission of a Raman photon[5].

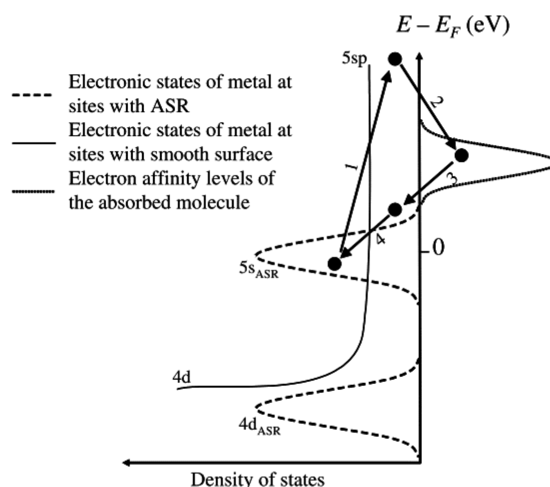

Figure 1.3 - Charge-transfer model for metal surfaces with atomic-scale roughness (ASR) and adsorbed molecules[4].

Although this is the most well-known, it is only one of many phenomena involved in the so-called chemical enhancing factor of SERS, along with inelastic Mie scattering[6], microensemble[7], modulation of the metal surface reflectivity[8], coherent parametric excitation[9], cooperative effects[10], surface-polarizability contribution[11], and forbidden bands[12]; many of them have been

proposed throughout the years and sometimes are not fully understood yet, while some may be present only with specific molecules or molecule-structure combinations. The listed phenomena are all concurrently enhancing the Raman signal without affecting the electromagnetic field, thus they all fall into the category of chemical enhancing factors.

In the vicinity of metallic structures, the electromagnetic field undergoes strong modifications; if the structures are nanometric in size, the frequency of the electromagnetic field can match that of the plasmon resonance of the metal structures. When nanostructures of noble metals are exposed to an incident electromagnetic field with the correct frequency, the field can be concentrated in very small regions called *hot spots*: these are sub-wavelength regions of space where the plasmons of the metal nanostructures are put in resonant conditions and, when the polarization of the incident field is oriented along the interstructure separation direction, a strong concentration of the field is obtained.

While the chemical enhancing of the Raman signal in SERS is poorly understood, and sometimes its existence is still debated, the electromagnetic enhancement of an incident field from metal nanostructures is part of a well-established field called plasmonics.

1.2 Principles of plasmonics

The study of the optical properties of metals (such as gold, silver, copper, or aluminium) have since long underlined their difference from other dielectric materials; from their exceptional electric and thermal conductivity to their unique optical properties, their strength is in the presence of free conduction electrons. These electrons can move over a background of positively charged ions, which balance the electronic negative charge and ensure neutrality of the material, and are usually called “free-electron plasma” or “solid-state plasma”, since it can exist in solid state materials.

The behaviour of this solid-state plasma can be described with different degrees of detail, but for the purpose of this work the simplest, yet not less accurate, will be presented.

1.2.1 The Drude-Lorentz model for the dielectric function of metals

The Drude model for the optical response of a free-electron plasma grounds on the Lorentz model of polarizability for a single atom or molecule[13].

The basic concept of the Lorentz model is the Lorentz oscillator. A Lorentz oscillator is a physical model which describes the interaction of an electromagnetic wave with a specific electronic state as a damped oscillator, similar to those described by classical physics, with natural frequency ω_0; this approximation is valid because the interaction described by the Lorentz model are much

smaller than the electronic interactions experienced by an atom or molecule. The equation describing the small perturbations from ground state of electrons immersed in an external field $\boldsymbol{E}$ can be written, for a coordinate $\boldsymbol{r}$, as:

$$m\left(\frac{d^2\boldsymbol{r}}{dt^2}+\omega_0^2\boldsymbol{r}+\Gamma\frac{d\boldsymbol{r}}{dt}\right)=-e\boldsymbol{E} \qquad 1.8$$

Γ is a dissipative term which accounts for all the interactions, internal or external, of the electrons with everything except the field, m and e the (effective) mass and charge of the electrons. Equation 1.8 as a classical forced damped harmonic oscillator, it can be solved conventionally. Considering $\mathbf{E}=\mathrm{Re}(\mathbf{E_0}\exp(-i\omega t))$, the expected solution is in the form of $\mathbf{r}=\mathrm{Re}(\mathbf{r_0}\exp(-i\omega t))$, which becomes:

$$\boldsymbol{r_0}=-\frac{e/m}{(\omega_0^2-\omega^2-i\Gamma\omega)}\boldsymbol{E_0} \qquad 1.9$$

The induced electric dipole moment is a complex quantity given by $\boldsymbol{p_0}=-e\boldsymbol{r_0}$ and, together with the definition of linear optical polarizability as $\boldsymbol{p_0}=\alpha_L(\omega)\boldsymbol{E_0}$, we can deduce an expression for the classical linear optical polarizability:

$$\alpha_L(\omega)=\frac{e^2/m}{(\omega_0^2-\omega^2-i\Gamma\omega)} \qquad 1.10$$

From this parameter, it is possible to derive an expression for the dielectric function of n molecules or atoms, given that the total polarization is $\boldsymbol{P}=(\epsilon_r(\omega)-1)\epsilon_0\boldsymbol{E}=n\alpha_L(\omega)\boldsymbol{E}$:

$$\epsilon_r(\omega)=1+\frac{n}{\epsilon_0}\alpha_L(\omega)=1+\frac{ne^2/m\epsilon_0}{(\omega_0^2-\omega^2-i\Gamma\omega)} \qquad 1.11$$

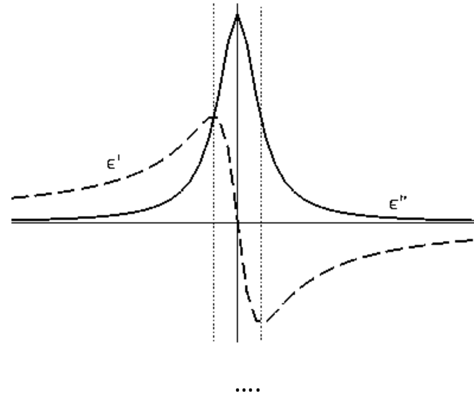

….

Figure 1.4 – Frequency response of the real (ε′) and imaginary (ε") part of the dielectric function from Equation 1.11.

The real and imaginary part of $\epsilon_r(\omega)$ can be plotted as a function of the ratio $\frac{\omega}{\omega_0}$ (Figure 1.4). In resonant conditions, *i.e.* when $\omega_0 = \omega$, the system behaves as a classical damped oscillator.

The Drude model for the dielectric function of noble metals takes over from the Lorentzian oscillator, considering that the particles are a cloud of free electrons, thus assuming $\omega_0 \cong 0$ and ignoring the optical response of the positive ions in the crystal. With this modification, Equation 1.11 becomes:

$$\epsilon_r(\omega) = 1 - \frac{ne^2}{m\epsilon_0}\frac{1}{\omega^2 + i\gamma_0\omega} \qquad 1.12$$

In this form, n is the number of electrons per unit volume, m their mass, and γ_0 is a damping term which corresponds to the collision rate of the free electrons with the crystal impurities, usually small if compared with ω. The previously ignored optical response from the ions in the crystal can be, as a first approximation, included in the model as a contribution to a constant, real background dielectric function $\epsilon_\infty \geq 1$, which results in a modified Equation 1.12 in the form of:

$$\epsilon_r(\omega) = \epsilon_\infty\left(1 - \frac{\omega_p^2}{\omega^2 + i\gamma_0\omega}\right) \qquad 1.13$$

The term $\omega_p = \sqrt{\left(\frac{ne^2}{m\epsilon_0\epsilon_\infty}\right)}$ is called plasma frequency and defined to be the natural oscillation frequency of the free electron plasma. The real and imaginary part of $\epsilon_r(\omega)$ can be separated:

$$Re\big(\epsilon_r(\omega)\big) = \epsilon_\infty\left(1 - \frac{\omega_p^2}{\omega^2 + \gamma_0^2}\right) \qquad 1.14$$

$$Im\big(\epsilon_r(\omega)\big) = \left(\frac{\epsilon_\infty\omega_p^2\gamma_0}{\omega(\omega^2 + \gamma_0^2)}\right) \qquad 1.15$$

It's evident, still keeping in mind that $\gamma_0 \ll \omega$, that for $\omega < \omega_p$ there is a region where $Re\big(\epsilon_r(\omega)\big)$ is negative and, if ω is not too small, also $Im\big(\epsilon_r(\omega)\big)$ is greatly reduced: in this region the absorption, which is related to the value of $Im\big(\epsilon_r(\omega)\big)$, is also small, thus allowing unconventional optical effects, plasmon resonance included. More interesting, since typical values for the plasma frequency of metals fall in the UV range (e.g. $\omega_p \cong 1.4 \times 10^{16}\,\frac{rad}{s}$ for both silver and gold has been derived experimentally and agrees quite well with the prediction of the Drude model – corresponding to a wavelength of about 135 nm), this region of interest falls in the visible part of the spectrum and close proximities (NUV or NIR).

From the Drude-Lorentz model is then possible to conclude that, to have good plasmonic properties, a metal should have:

- $Re(\epsilon_r(\omega)) < 0$ in the wavelength range of interest (typically from NUV to NIR);
- $Im(\epsilon_r(\omega))$ as small as possible in the same wavelength range.

Few materials satisfy both these conditions at once: among all the different metals, only copper, lithium, silver, and gold are good candidates for plasmonics. Lithium, however, is a rare element and it is highly reactive in water, so it has been discarded for practical reasons; the use of copper in plasmonics is not very common as well, due to its cost combined with the difficulty to be used in the form of nanostructures and therefore the lower performances with respect to another candidate with the same range of applicability (*i.e.* gold). Gold and silver, instead, are the most widespread materials for plasmonics: while gold is ideal for applications at wavelengths higher than 600 nm, up to the NIR, silver has the lowest absorption in the visible range, in particular for wavelengths below 600 nm, making those two metals complementary for the applications in plasmonics.

1.2.2 Surface plasmon polaritons and LSPR in single particles

The term plasmon is defined as a quantum quasi-particle representing the elementary excitations, or modes, of the charge density oscillations in a plasma[13,14]. It is called "quasi-particle" since, even though it is quantised (like a photon for electromagnetic field), it must be maintained through an external excitation otherwise it will rapidly decay. When the oscillations described by a plasmon are confined over a metal/dielectric interface in thin films, are supported by a transverse electromagnetic field, and their propagation direction is longitudinal, they are called surface plasmon polaritons.

When dealing with plasmonics, the relationship between the properties of the free-electron plasma and the optical properties of the material must always be considered; the dielectric function of the metal considered, as described in the previous paragraph, can be used in plasmonics, and even more in SERS, to predict and understand the optical response of the system. However, when the size of the metal structures considered becomes smaller to the point to be comparable with, or smaller than, the wavelength of the incident field, new phenomena arise.

The simplest example of metal nanostructure interacting with an external electromagnetic field is a metallic nanoparticle of dielectric function $\epsilon(\omega)$ and radius r illuminated by a monochromatic light of wavelength λ (with $r \ll \lambda$). The choice of this example is due to the availability of an

analytical solution of the electromagnetic problem in the form of the Mie theory for a sphere, which can be used to justify simpler approximations that will be used hereafter.
The electrostatic approximation used in this paragraph considers the incident electric field as a *constant* field $\boldsymbol{E_{inc}}$. It can be demonstrated in many textbooks[15] that the solution of the electromagnetic problem inside a metallic sphere immersed in a non-absorbing infinite dielectric medium of dielectric constant ϵ_M is:

$$\boldsymbol{E_{in}} = \frac{3\epsilon_M}{\epsilon + 2\epsilon_M}\boldsymbol{E_{inc}} = (1 - \beta_S)\boldsymbol{E_{inc}} \qquad 1.16$$

Where the term $\beta_S = \frac{\epsilon(\omega) - \epsilon_M}{\epsilon(\omega) + 2\epsilon_M}$ has been introduced. The resulting electromagnetic field is then constant inside the sphere, where it is also possible to calculate the electric polarization $\boldsymbol{P_M}$ with respect to the surrounding medium from the already known relation $\boldsymbol{P_M} = \epsilon_0(\epsilon - \epsilon_M)\boldsymbol{E}$. Using Equation 1.16 to calculate $\boldsymbol{P_M}$ we obtain:

$$\boldsymbol{P_M} = 3\epsilon_0\epsilon_M\beta_S\boldsymbol{E_{inc}} \qquad 1.17$$

When integrated over the volume $V_S = \frac{4}{3}\pi r^3$ of the sphere, the constant polarization inside the sphere can be considered equivalent to a dipole $\boldsymbol{p_M} = \alpha_S\boldsymbol{E_{inc}}$ where the polarizability can be rewritten as:

$$\alpha_S = 3\epsilon_0\epsilon_M V_S\beta_S = 4\pi\epsilon_0\epsilon_M r^3\frac{\epsilon(\omega) - \epsilon_M}{\epsilon(\omega) + 2\epsilon_M} \qquad 1.18$$

With these assumptions, the electromagnetic field outside the sphere can be considered equivalent to the sum of the incident field plus the electromagnetic field of the induced dipole. This is correct because interaction of the incident electromagnetic field with the metallic sphere induces a polarization across the sphere itself, which can be modelled with a point dipole, called induced dipole, with equivalent effects. The equations obtained up to now can be used to calculate the localized surface plasmon on the same sphere, making the same assumptions and approximations. The parameter introduced earlier, β_S, can be considered as the non-dimensional polarizability of the sphere; this parameter is frequency (and conversely wavelength) dependent and complex since the dielectric function itself is complex ($\epsilon(\omega) = \epsilon'(\omega) + i\epsilon''(\omega)$). When the electromagnetic response of the sphere is resonant, a resonance condition for β_S should also be found: a resonance occurs when the denominator of $|\beta_S|$ tends to zero, *i.e.* for $\epsilon(\omega) = -2\epsilon_M$. Since ϵ_M is real and positive for a non-absorbing medium and $\epsilon''(\omega) \neq 0$ for metals, the resonant condition for β_S is

approximately reached for $\epsilon'(\omega) = -2\epsilon_M$ and the corresponding frequency (or wavelength) is considered the localized plasmon resonance. It can be demonstrated[13] that this resonance condition is valid for one wavelength only, and that this wavelength is red-shifted for higher values of ϵ_M. This frequency also corresponds to the peak in the extinction coefficient $Q_{Ext}(\omega_L)$ of the particle, a very important property when experimentally characterizing a substrate, which accounts for the "strength" of the optical response of the system; the extinction coefficient accounts for both the absorbing and scattering of light, which are difficult to evaluate separately, and can be written as $Q_{Ext}(\omega_L) = \log_{10}\frac{I_0}{I(\omega_L)}$, where I_0 is the intensity of the incident light and $I(\omega_L)$ the intensity of the light beam after the interaction with the system. Moreover, in the electrostatic approximation, the localized plasmon resonance frequency doesn't depend on the radius of the particle considered.

The particle radius is instead of primary importance for the quantification of the SERS enhancement factor for molecules at a distance d from the surface of a metallic nanospheres. From theory, it can be demonstrated that the electric field amplitude decays as a $(r + d)^{-3}$ and, given the fourth-power dependence of the SERS enhancement from the scattered electric field, the enhancement should scale down with $(r + d)^{-12}$. This very steep decrease in the enhancement suggests that only the first layer of adsorbed molecules benefits from the SERS effect; however, considering the ratio between r and d, and the typical values of r for nanoparticles used in SERS experiments, it has been experimentally evaluated that the distance at which a SERS enhancement is still relevant is much larger than a monolayer, so the SERS effect can be considered a "long range" effect (with respect to the typical monolayer dimension).

1.2.3 Hot spots in coupled nanostructures

The frequency, intensity and spatial extensions of the enhanced EM field depend on several parameters, such as the size and the shape of the noble metal and its dielectric surrounding[16]. By using isolated nanoparticles, enhancements of the order of 10^3 can be obtained[17]. However, when more particles get in close proximity the constructive interference of the EM fields from different surface plasmons, enhances enormously the field in the gaps[18]. These nanometric regions characterized by highly enhanced fields are known as hot spots[19]. In a hot spot both the intensity and the wavelength of the plasmon resonance frequency depend on the size, shape and separation between the nanoparticles; this property has been used in the development of "plasmonic rulers", nanometric-sized systems where the interparticle distance can be converted into a shift in the extinction spectrum peak[20].

As for the isolated particle, it is convenient to consider a case study (summarized in Figure 1.5 (a)): a dimer of two identical metal spheres with dielectric function $\epsilon(\omega)$ and radius r, separated by a gap of width g and dimer axis along the z direction, illuminated by an incident electromagnetic field travelling along the x axis and polarized in the z direction (parallel to the dimer axis, to achieve maximum coupling[21]), immersed in a non-absorbing medium of dielectric constant ϵ_M. The coupling of these two particles creates a system with new LSPR values for the extinction coefficient, different from the case of the single particle and varying with the gap width g (Figure 1.5 (b)); the most important of them for the SERS effect is the one with lower frequency (*i.e.* higher wavelength) which exhibit a strong dependence from the g (Figure (c)). The peaks of the SERS enhancement factor can be easily related to the peaks in the extinction coefficient, except for the intensity[22].

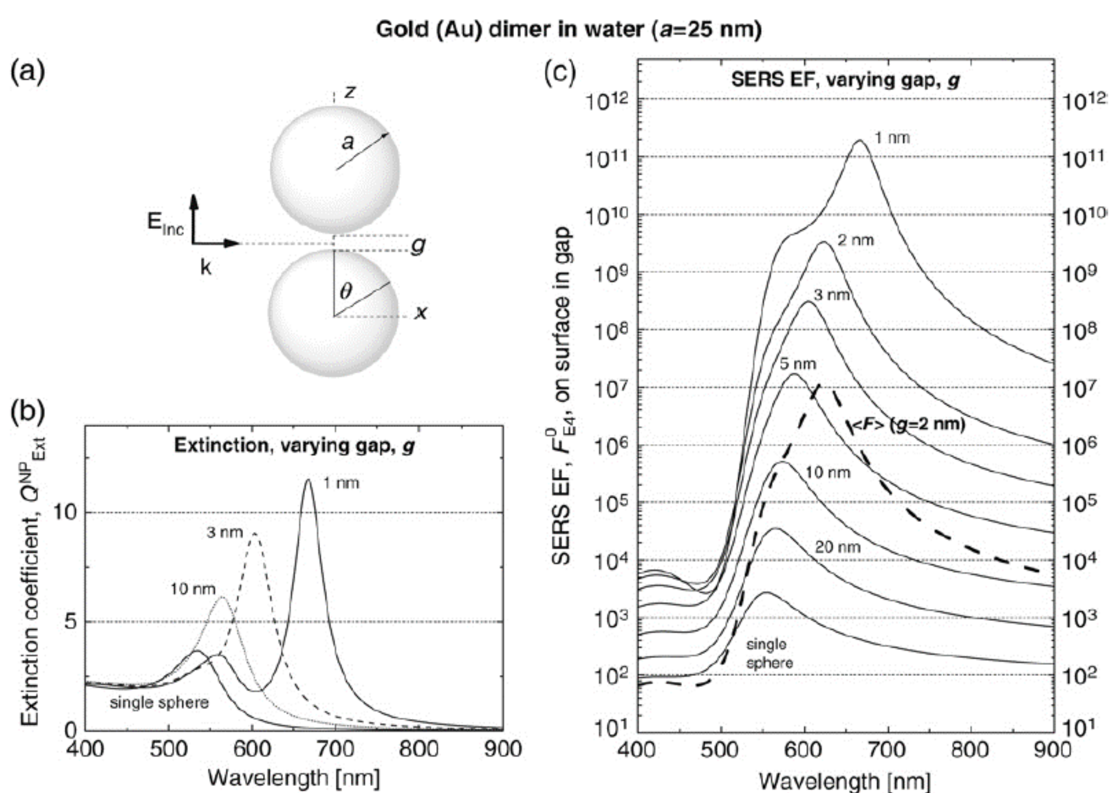

Figure 1.5 - Example of case study for a dimer of nanoparticles. (a) Schematics of the dimer for nanoparticles of radius a, gap width g, with dimer axis along the z direction, incident field traveling along x and polarized along z. (b) Extinction spectra for varying values of g and for a single nanosphere. (c) SERS enhancement factor for a single nanosphere and for dimers with varying gap widths calculated on the surface of the single nanosphere or in the middle of the gap. The black dotted line is the average SERS enhancement around the dimer for g = 2 nm. Reproduced from Le Ru, Etchegoing[13].

What happens with a dimer is that the local field effects, and therefore the SERS enhancement factor, is extremely increased in the gap when the polarization direction of the incident wave is correct and the interparticle distance is very small, thus creating the hot spots (Figure 1.6). From analytical calculations, it can be predicted that values of the SERS enhancement factor for a single molecule in a hot spot region with $g = 1\ nm$ can be as high as 5×10^{11}. The premise to this very

high number is important, since the average SERS enhancement factor is much lower than the enhancement for a single molecule in a precise position of space: the hot spot creates a region of highly localized enhanced field confined in the gap between the nanoparticles, a condition that requires the analyte molecules to be precisely positioned exactly in the gap and exactly along the dimer axis, something that cannot be easily nor reasonably achieved in the most common SERS systems.

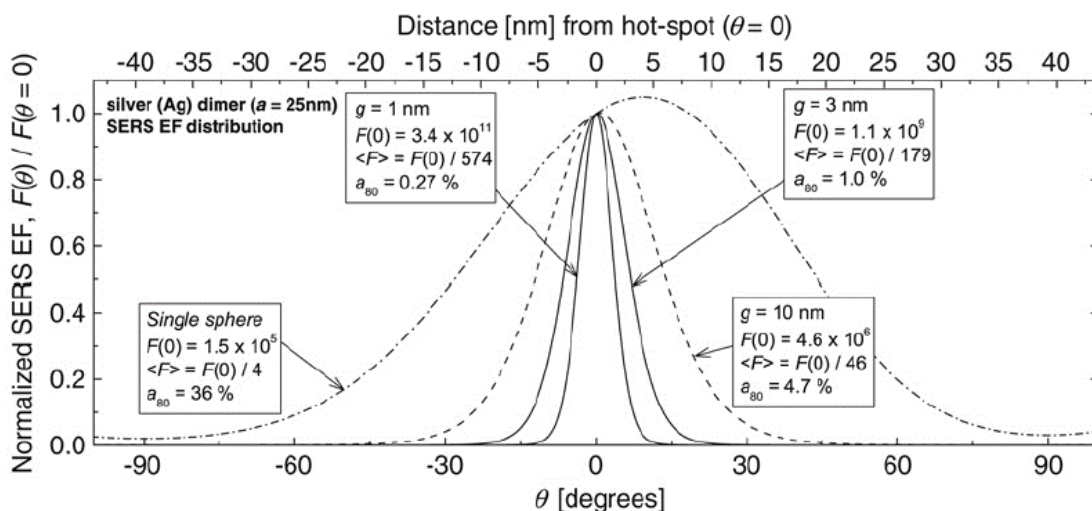

Figure 1.6 - Normalized SERS enhancement factor as a function of the angular distance θ from the polarization direction (lower axis) or the hot spot axis (upper axis). Data are plotted for a single silver particle of radius 25 nm and for a dimer of equivalent particles at $g = 1, 3, 10\ nm$. Reproduced from Le Ru, Etchegoing[13].

This consideration can be useful to read the values of SERS enhancement factor for different systems critically, since in most systems the enhancement of single dimers or coupled nanostructures cannot be evaluated and therefore only an averaged value is obtained; this averaged value is almost 600 times lower than the single-molecule, gap-localized enhancement factor which is theoretically (and sometimes impossibly) achievable.

1.2.4 The effect of surface roughness

The case of rough metallic surface is worth separate considerations, since the first SERS studies have been done on the roughened surface of silver electrodes[16] and this kind of substrates remained the most widespread for a long time. The theory underlying the SERS effect on roughened surface is too complex for the purpose of this work, but something that must be underlined is the effect of the introduction of roughness on flat surfaces: momentum conservation is broken and otherwise forbidden coupling with surface plasmon polaritons at the interface are allowed. The result of nanometric scale roughness on flat metallic surface is an increase in the SERS enhancement factor, which can amount to 10^3-10^4, still a lower value than that of coupled nanostructures but still

a good signal enhancement for experimental purposes; given the ease of fabrication of rough surfaces with respect to nanostructures, this kind of substrate is still widely used for practical applications of SERS.

1.3 Hot spot control in SERS systems

As already mentioned, the SERS enhancement is caused by two concurrent factors: the chemical enhancement and the electromagnetic field enhancement. While the former depends strongly on the relationship between the metal surface and the analyte of interest, making it difficult to control its behaviour on multi-purpose systems, the latter can give a molecule-independent enhancement which can be engineered to enhance the SERS signal of different analytes.

The plasmonic phenomena responsible for the electromagnetic enhancement of the SERS signal are dominated by the effect of the hot spots between nanostructures; for this reason, different kinds of SERS substrates have been designed, with different approaches and results.

1.3.1 Colloid-based substrates

Silver and gold colloids, especially citrate-reduced colloids, are the most commonly used SERS substrates because they are easily prepared and can be well characterized. The shape and size of their particles can also be controlled by inexpensive, versatile approaches. The first realization of SERS in colloidal solutions of metal particles is reported in 1979: in this fundamental work by Creighton and coworkers[6], the absorption, extinction, and scattering spectra of silver and gold colloidal solutions were measured, along with the Raman spectrum of pyridine before and after the mixing with the colloids. This work was followed shortly by the work of Wetzel and Gerischer in 1980[23], which confirmed the signal enhancement by gold and silver colloids. More recently, very high enhancements (in the order of 10^{14}-10^{16}) have been obtained in the first demonstration of single-molecule SERS experiments[24,25].

Stable gold colloids with narrow size distributions were recently synthesized by a reduction with citrate[26]. Improved shape/size control of silver particles - along with the preparation of uniform, stable silver colloids - has become an active research area. Citrate-reduced silver colloids can be prepared by reducing silver nitrate with sodium citrate at its boiling point, according to Lee and Meisel[27], wherein citrate also stabilizes the dispersion. In contrast to gold colloids, silver colloids can exist as prisms, rods, and disks of varying size, though spherical particles are the most common. Methods for controlling particle morphologies include adding stabilizers, adjusting heating and stirring rates, changing the citrate/silver nitrate ratio, and adjusting the pH[28,29]. Stable,

monodisperse sols can be obtained by such methods. However, some added substances decrease the SERS activity of silver particles in substrates used for diagnosing and characterizing analytes. This is attributable to competitive adsorption of the analyte and added substance[30].

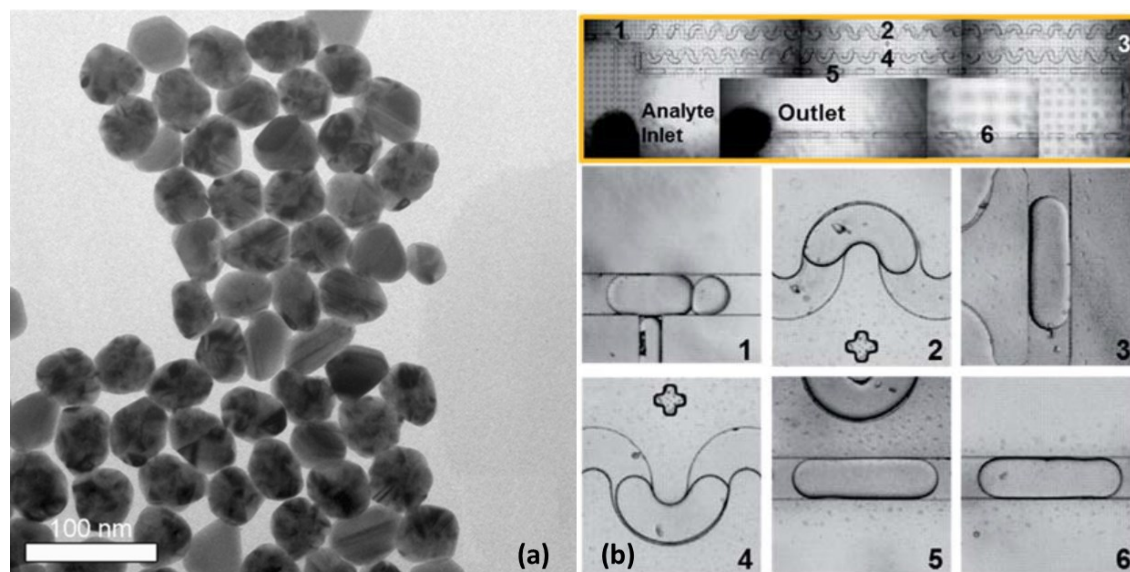

Figure 1.7 - (a) TEM image of stabilized colloidal silver nanoparticles[30]. (b) Optical images of the integrated microchannel with in situ synthesis of nanoparticles for SERS analysis; the channel depicted is 200 µm wide, while the side channel at the bottom of b.1 is 100 µm wide. Reproduced from literature[31].

Another advantage of colloidal SERS solutions is the possibility to inject them in microchannels for direct mixing with the analyte near the sensing region; the group of Gao *et al.* tried to solve the problem of the nanoparticle stability during microfluidic transfer by synthetizing them directly into a microchannel prior to the mixing[31]. While the approach was successful, at least in their application, it didn't solve the main drawback of this approach: to achieve interparticle distances of less than 10 nanometres, the concentration of the nanoparticles should be very high, thus leading to a waste of expensive material, and to undesired aggregation, which can reduce the SERS efficiency of the system and, if not properly addressed, clog the microchannel.

Even though the enhancement factor of colloid-based SERS substrates is really high, the main drawback of this solution is the low control over the orientation of the hot spots exposed to the field; since the hot spot activity is not only distance-dependent but also polarization-dependent, if the dimers or aggregates of nanoparticles are oriented in unfavourable directions the enhancement is greatly reduced. Moreover, the analyte quantity subject to the enhancement is strongly dependent on the affinity with the metal surface of the nanoparticles and the presence of enhancement regions where the molecules are bound; this problem is more relevant for the analysis of a very limited number of molecules, as reported even in the single molecule detection experiments.

1.3.2 Nanofabrication-based substrates

The modification of surfaces to act as SERS substrate has a very wide range of different methods. The generation of hot spots on metal surfaces can be engineered either with a top-down or a bottom-up approach, or sometimes with a combination of both.

The basic requirement for a surface to demonstrate SERS activity is the presence of nanometric features, either isolated or grouped in different fashions. The simplest method to create a metallic structure with nanometric roughness is to directly evaporate a noble metal onto another material. The substrate for the evaporation must have good affinity with the metal and shouldn't exhibit appreciable damping of the plasmonic properties of the thin film[32] and, if possible, already have micro- or nanometric features that can already create localized hot spots[33]. With this very simple approach it is possible to create large samples, but the total enhancement obtained is relatively small. The fabrication of nanoparticles with built-in hot spots using a bottom-up approach has been reported recently from many groups[34–37]; while the approach is promising because of its relative simplicity and versatility of application, the enhancing performances are still not optimized and stability issues often arise. The low enhancement of these substrates is mainly due to the random distribution of the plasmonic features: to increase the performance of surface-based structures, control over the presence and position of the nanometric features is required.

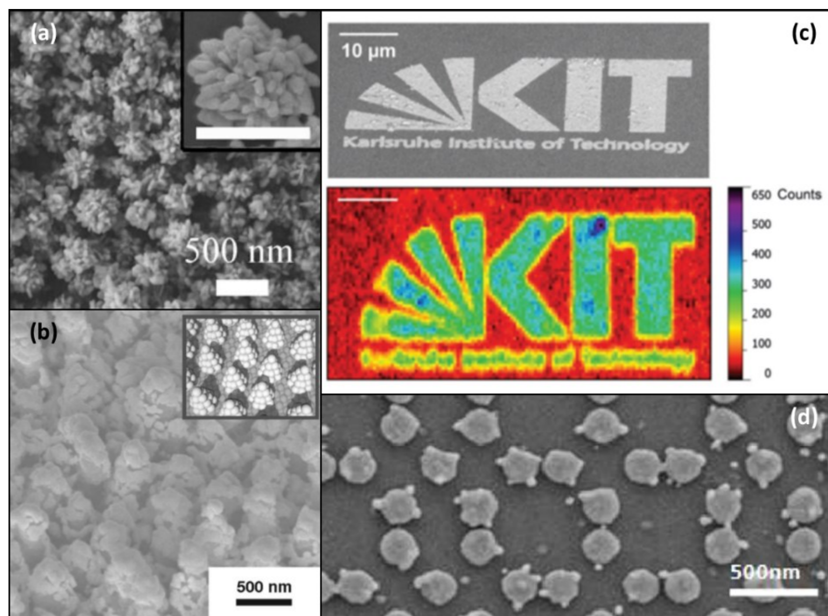

Figure 1.8 - (a) SEM image of citrate-stabilized silver nanosphere with controlled surface roughness[34]. (b) Nanostructured substrate with silver coating obtained with femtosecond-pulsed laser lithography[38]. (c) SEM image (top) and Raman mapping (bottom) of a SERS pattern obtained with laser-induced aggregation of gold nanoparticles[39]. (d) Gold nanocylinders decorated with in situ synthetized gold nanoparticles[40].

To address more effectively the hot spot location problem, micro- and nanofabrication techniques have been used to create well-defined zones of electromagnetic field enhancement. Conventional optical and electronic lithographic techniques can be applied to the fabrication of precisely-placed hot spots. Recently, the creation of controlled hot spot through femtosecond-pulsed laser exposure of Ag-covered silicon nanostructures has been reported[38,41] with a high density of nanostructures and good enhancement factor; this method requires femtosecond laser for the fabrication, increasing greatly the manufacturing cost. Other kinds of structures have been fabricated with optical lithography[42], obtaining bowtie optical antennas which are capable of creating enhanced field regions in a more straightforward way. The achievement of higher resolution with electron beam lithography (EBL) has been reported in other works in the past decade[43,44], but the process speed is much slower, thus making large-scale substrate fabrication more challenging. The modification of a glass surface with nanoparticles functionalised with photochemical-active molecules has been reported[45]: scanning the surface of a glass substrate immersed in a solution of nanoparticles modified with Diels-Adler cycloaddition[46] with a NIR laser, a controlled arrangement of nanoparticles has been created, with interparticle distance compatible with the hot spot activity range. This technique has been further improved using direct laser writing (DLW) to create more closely-packed and ordered arrangements of nanoparticles with enhanced Raman scattering activity[39].

The association of top-down and bottom-up approach has also been tried for the creation of controlled SERS substrates. The group of Gopinath reported the fabrication of aperiodic nanocylinder arrays using e-beam lithography followed by evaporation of gold to create larger nanoparticles, and then an *in-situ* growth of smaller gold nanoparticles creates the hot spots region[40]. The position of the bigger particles is easily controlled by changing the nanofabrication pattern, while the growth of the smaller particles is responsible for the density of the hot spots.

1.4 Dynamic control of plasmonic properties

All the substrates presented in the previous chapter showed SERS activity and hot spots in localized or distributed regions obtained with different approach. However, in recent years the interest of the researchers has moved also on the control of the activity of the hot spots. The creation of SERS substrates with on-off switchable, or intensity-tuneable, hot spots has been, and still is, a dominant research topic.

The modification of the nanoparticle surface has been exploited to control the interparticle distance and thus the activity of hot spots in a colloidal solution. The interaction of DL-penicillamine (PEN) and its amine protected counterpart N-acetyl-DL-penicillamine (NAP) with citrate stabilized metal

nanoparticles has recently demonstrated to be dependent from the pH of the solution; by changing the acidity of the solution, a reversible assembly of the modified nanoparticles has been obtained, where a SERS effect has been measured when aggregation of the particles was maximum[47].

A self-assembly of superparamagnetic Fe_3O_4@Au nanoparticles at a liquid-liquid interface has shown tuneable behaviour by exposing the particles to an external magnetic field; the balancing between the magnetic attraction and the electrostatic repulsion leads to aggregation of the particles which is reversible if the magnetic field is removed[48]. While this system showed good SERS activity, the dependence from the water-hexane interface for the formation of the monolayer can be a serious limit to the applicability of this technique.

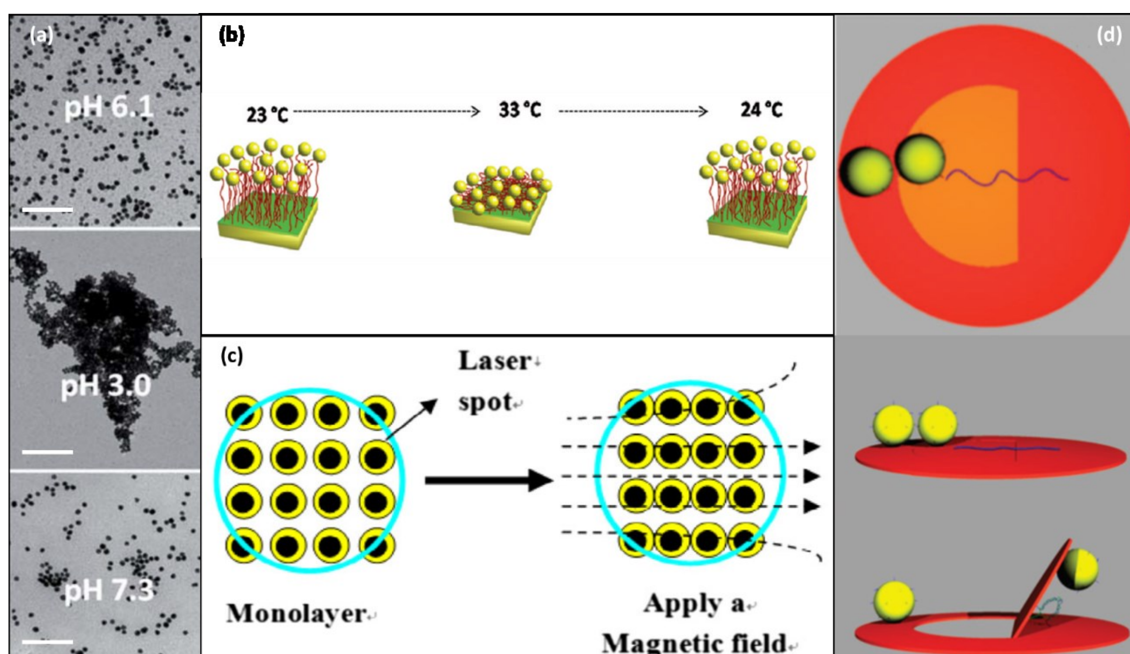

Figure 1.9 - (a) TEM images of the modulation of plasmonic activity through pH-based control of nanoparticles aggregation in solution[49] (scale bar: 200 nm). (b) Schematics of a reversible thermo-induced aggregation of gold nanoparticles on a functionalized gold substrate[50]. (c) Schematics of the magnetic field-dependent aggregation of a monolayer of Fe_3O_4@Au nanoparticles at a water-hexane interface[48]. (d) Drawing of the DNA origami framework for reversible tuning of interparticle distance mediated by biomolecular recognition processes. Top and side view of the closed structure and side view of the opened structure are represented[51].

A thermal approach to the switching of plasmonic hot spot-rich surfaces has been tried with a polymer as intermediate agent by Gehan and coworkers; in a research article[50], they report the temperature-mediated change of the distance between a gold surface, functionalized with brushes of poly(*N*-isopropylacrylamide) (PNIPAM) using click chemistry, and gold nanoparticles. The polymeric linker undergoes conformational changes depending on the temperature, with a limit called lower critical solution temperature at which the distance between the nanoparticles and the surface is compatible with hot spot formation. The enhancement of this substrate is limited by the steric hindrance of the linker, which limits the surface-particle distance to a minimum of ~20 nm even in the most packed configuration, thus reducing the overall SERS performances. The same

principle of thermal tuning of hot spot formation has been used in the work of Yiping *et al.*, where the same polymer (PNIPAM) has been used to create thermosensitive nanospheres decorated with silver nanoparticles. Sweeping the temperature of the system between 20 °C and 55 °C, the shrinking and swelling of the nanospheres change the distance between the silver nanoparticles from tens of nanometres to less than ten nanometres, in the useful distance range for the formation of plasmonic hot spots. The swelling of the nanospheres should allow the adsorption of a larger number of analyte molecules on the surface of the silver nanoparticles, whereas the shrinking enables the plasmonic enhancement of the Raman signal. This system, although promising, has shown only limited enhancement factor between the swollen and shrunken configuration, less than 10^3.

Another way to tune the plasmonic response of nanostructures exploits the interaction between biomolecules: Moskovits and coworkers have also used short single-stranded DNA chains, or aptamers, which form a stem-loop linked to Au nanospheres to reversibly control the formation of electromagnetic hot spots. In their experiments DNA was used to assemble 80 nm and 20 nm nanoparticles, but also exploited for its conformational change to indirectly probe the presence of adenosine by monitoring the SERS intensity of 4-amino-benzenethiol[52]. Alternatively, the decoration of a DNA-origami framework with two gold nanoparticles, placed across a movable hatch and a fixed structure, at nanometric interparticle distance. The hybridization of a target DNA strand with a complementary strand which links the tip of the hatch and the fixed structure opens the hatch, thus changing the interparticle distance and causing a shift in the LSPR behaviour of the dimer[51]. The hybridization event is demonstrated to be reversible with the addition of a competitor with higher affinity towards the linker[53], and its potential applications range from the characterization of DNA hybridization to tuneable plasmonic platform, although they haven't been explored yet.

1.4.1 Controlling plasmonic properties with MEMS

Micro- and NanoElectroMechanical Systems (MEMS/NEMS) are devices which incorporate integrated mechanical and electronic components with micron and/or nanometric size; since their appearance in the early 1970s, the applications of MEMS/NEMS have been innumerable. Their strength is in the combination of very high performances (e.g. they can have very high sensitivity when used as sensing or transducing devices or very low power consumption when compared to similar, bigger devices), the ability to integrate different functions in a small space, and the opportunity to be fabricated with mature, well-known techniques in very large scale, up to thousands of devices over a single silicon wafer. Resonating devices in particular have shown

promising results in the tuning of plasmonic properties using the coupling with mechanical motion of the devices and vice versa.

The coupling between an atomic force microscope (AFM) metalized tip and a surface has been exploited in scanning near-field optical microscopy (SNOM); the first authors of this technique demonstrated that it is possible to separate the light components scattered by an AFM tip in contact with a dielectric surface from the background using higher harmonics demodulation, which experimentally demonstrated the nonlinearity of the hot spot formation process[54]. The demodulation of the scattered signal recorded in the gap between the AFM tip and the dielectric surface demonstrated increasing contrast for increasing harmonics, with the highest spatial resolution obtained for third harmonic demodulation. Following their lead, this technique has been applied in the IR[55–57] and visible[58,59] range of light for the visualization of the near-field distribution in plasmonic nanostructures, but no attempt of extending the technique to Raman spectroscopy has been reported yet.

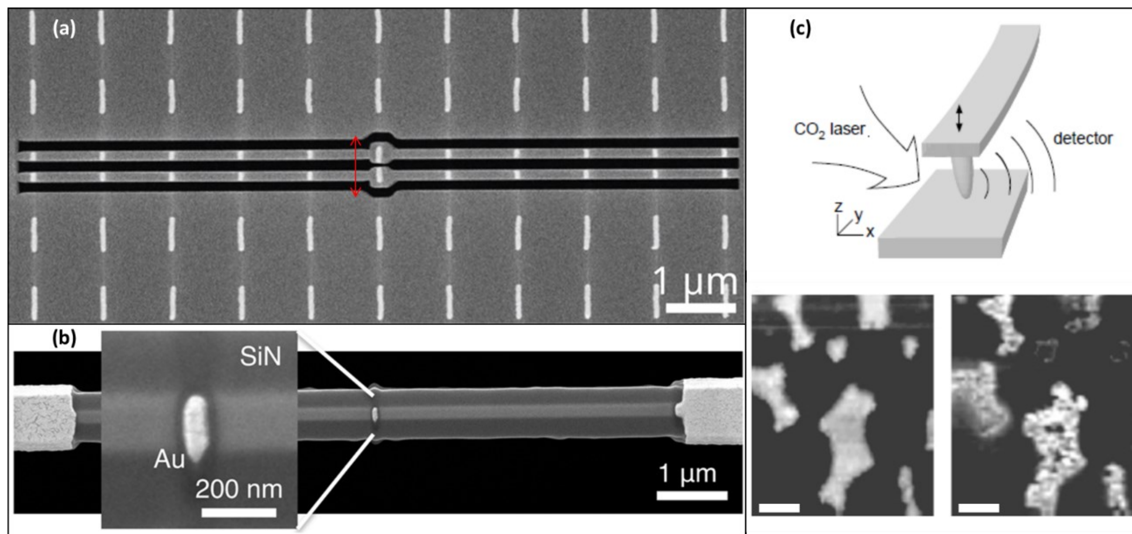

Figure 1.10 - (a) Coupled nanobridges for the modulation of the plasmonic dimer nanoantenna for the modulation of the plasmon resonance using mechanical coupling[60] (the red arrow shows the in-plane direction of the motion). (b) Nanostring with plasmonic nanorod for the characterization of photothermal effects in plasmonic structures[61]. (c) Schematics of the setup with the oscillating AFM tip illuminated from the side by an IR source (top); comparison between AFM topography (bottom, left) and infrared SNOM imaging (bottom, right) of gold nanoislands[62] demonstrating a resolution of <100 nm. Scalebars are 200 nm.

The first report of the coupling between a nanomechanical resonator and a gold nanostructure was published in 2013 by the group of Thijssen and coworkers. They fabricated a double bridge suspended structure from a silicon nitride membrane coated with a thin film of gold; actuating the device at the resonant frequencies of the bridges for three modes of oscillation (one in plane and two out of plane) the gap between the bridges is modulated, and so is the hot spot. The excitation laser polarization was changed for the different modes and the polarization dependence of the hot spot formation in this device has been demonstrated[63]. The same group realized the modulation of

the hot spot created by two plasmonic nanoantennas fabricated across two silicon nitride bridges; they measured the power spectral density illuminated by a laser spot while raster scanning the surface of the device, thus allowing for the localization of the hot spot[60]. Addressing the problem from another point of view, Silvan Schmid and coworkers measured the heat generation and diffusion around plasmonic hot spots by coupling nanoslits of different orientation made on gold patches, and isolated nanorods, with a suspended silicon nitride nanostring. The plasmon-driven photothermal effect has been successfully measured in both kinds of structures by photothermal mapping of the resonator surface[61]. Even though the results of these two approaches to the coupling between mechanical and plasmonic properties using MEMS have been encouraging, no devices have been yet reported exploiting this coupling for Raman spectroscopy or SERS purpose.

1.5 Objective of the research project

The growing interest in the mechanical modulation of plasmonic properties has opened the path to many different ways of integrating mechanical and plasmonic properties of MEMS/NEMS. However, at the beginning of this project, no attempt had been done towards the application of plasmomechanical devices to Raman spectroscopy and SERS studies. The aim of the presented research is to realize a plasmon-active optomechanical device capable of enhancing the Raman signal of analytes through the creation of frequency-modulated plasmonic hot spots which can be switched on and off depending on the actuation of the resonating component.

With the application of micro- and nanofabrication techniques, two different approaches to this goal have been tried. In the first part of the work, micropillars as resonating elements facing a steady wall has been used to obtain a switchable hot spot region along the separation gap between the two structures; although an enhancement has been observed, different problems have arisen towards the realization of a well-performing device. The second part of the research has been dedicated to the realization of another kind of structure exploiting a horizontal suspended cantilever equipped with a tip and engineered to have its first resonance mode in plane with the surface of the device: with this configuration, the issues evidenced by the pillar-based device have been successfully overcome, thus demonstrating the realization of a frequency-modulated hot spot with SERS capabilities in a well-defined position. The advantages of precisely controlling the presence and position of a hot spot are multiple. First, the modulation of the hot spot allows the reduction of the energy on the sample even more than the traditional SERS effect by synchronizing the excitation with the hot spot formation appropriately; this is exceptionally important for the study of delicate analytes, liquid samples, or biological specimens. Second, the increased contrast that can be obtained through the demodulation of a frequency-modulated hot spot can further

decrease the limit of detection in SERS analysis, thus allowing the analysis of smaller or very diluted samples. Finally, if the position of the hot spot can be determined *a priori*, the signal-to-noise ratio can be increased subtracting the contribution from regions outside the field enhancement area.

References

(1) Stedwell, C. N.; Polfer, N. C. Laser Photodissociation and Spectroscopy of Mass-Separated Biomolecular Ions. **2013**, *83*.

(2) Cardona, M. Resonance Phenomena. In *Light Scattering in Solids II: Basic Concepts and Instrumentation*; Cardona, M., Güntherodt, G., Eds.; Springer Berlin Heidelberg: Berlin, Heidelberg, 1982; pp 19–178.

(3) Bernath, P. F. Light Scattering and the Raman Effect. In *Spectra of Atoms and Molecules*; Oxford university press, 2015; pp 293–320.

(4) Yuen, C.; Zheng, W.; Huang, Z. Surface-Enhanced Raman Scattering: Principles, Nanostructures, Fabrications, and Biomedical Applications. *J. Innov. Opt. Health Sci.* **2008**, *1* (2), 267–284.

(5) Otto, A.; Billmann, J.; Eickmans, J.; Ertürk, U.; Pettenkofer, C. The "adatom Model" of SERS (Surface Enhanced Raman Scattering): The Present Status. *Surf. Sci.* **1984**, *138* (2–3), 319–338.

(6) Creighton, J. A.; Blatchford, C. G.; Albrecht, M. G. Plasma Resonance Enhancement of Raman Scattering by Pyridine Adsorbed on Silver or Gold Sol Particles of Size Comparable to the Excitation Wavelength. *J. Chem. Soc. Faraday Trans. 2* **1979**, *75*, 790.

(7) Robinson, G. Surface-Enhanced Raman Effect. *Chem. Phys. Lett.* **1980**, *76* (2), 191–195.

(8) McCall, S. L.; Platzman, P. M. Raman Scattering from Chemisorbed Molecules at Surfaces. *Phys. Rev. B* **1980**, *22* (4), 1660–1662.

(9) Ke-hsueh, L. A Model of Coherent Parametric Excitation for Giant Raman Effect. *Surf. Sci.* **1982**, *115* (3), 513–523.

(10) Hu, C.-K.; Huang, C.-Y. Cooperative Effects in Raman Scattering. *Opt. Commun.* **1982**, *43* (6), 395–400.

(11) Jha, S. S.; Kirtley, J. R.; Tsang, J. C. Intensity of Raman Scattering from Molecules Adsorbed on a Metallic Grating. *Phys. Rev. B* **1980**, *22* (8), 3973–3982.

(12) Brundle, C. R. *Vibrations at Surfaces*; Elsevier, 2000; Vol. 14.

(13) Le Ru, E.; Etchegoin, P. *Principles of Surfance Enhanced Raman Spectroscopy and Related Plasmonic Effets*; 2009; Vol. 1.

(14) Pines, D. Collective Energy Losses in Solids. *Rev. Mod. Phys.* **1956**, *28* (3), 184–198.

(15) Jackson, J. D. Classical Electrodynamics, 3rd Ed. *Am. J. Phys.* **1999**, *67* (9), 841–842.

(16) Fleischmann, M.; Hendra, P. J. J.; McQuillan, A. J. J. Raman Spectra of Pyridine Adsorbed at a Silver Electrode. *Chem. Phys. Lett.* **1974**, *26* (2), 163–166.

(17) Naumenko, D.; Zannier, V.; Grillo, V.; Cassese, D.; Priante, G.; Dal Zilio, S.; Rubini, S.; Lazzarino, M. Enhanced Plasmonic Properties of Gold-Catalysed Semiconductor Nanowires. *Nanoscale* **2014**, *6* (22), 13651–13659.

(18) Le Ru, E. C. C.; Meyer, M.; Etchegoin, P. G.; Le Ru, E. C. C.; Blackie, E.; Meyer, M.; Etchegoint, P. G.; Etchegoin, P. G. Surface Enhanced Raman Scattering Enhancement Factors: A Comprehensive Study. *J. Phys. Chem. C* **2007**, *111* (37), 13794–13803.

(19) Stockman, M. I.; Pandey, L. N.; George, T. F. Inhomogeneous Localization of Polar Eigenmodes in Fractals. *Phys. Rev. B* **1996**, *53* (5), 2183–2186.

(20) Sönnichsen, C.; Reinhard, B. M.; Liphardt, J.; Alivisatos, A. P. A Molecular Ruler Based on Plasmon Coupling of Single Gold and Silver Nanoparticles. *Nat. Biotechnol.* **2005**, *23* (6), 741–745.

(21) Etchegoin, P. G.; Galloway, C.; Le Ru, E. C. Polarization-Dependent Effects in Surface-Enhanced Raman Scattering (SERS). *Phys. Chem. Chem. Phys.* **2006**, *8* (22), 2624.

(22) Le Ru, E. C.; Galloway, C.; Etchegoin, P. G. On the Connection between Optical Absorption/extinction and SERS Enhancements. *Phys. Chem. Chem. Phys.* **2006**, *8* (26), 3083.

(23) Wetzel, H.; Gerischer, H. Surface Enhanced Raman Scattering from Pyridine and Halide Ions Adsorbed on Silver and Gold Sol Particles. *Chem. Phys. Lett.* **1980**, *76* (3), 460–464.

(24) Kneipp, K.; Wang, Y.; Kneipp, H.; Perelman, L. T.; Itzkan, I. Single Molecule Detection Using Surface-Enhanced Raman Scattering (SERS). *Phys. Rev. …* **1997**, *78* (9), 1667–1670.

(25) Nie, S. Probing Single Molecules and Single Nanoparticles by Surface-Enhanced Raman Scattering. *Science (80-.).* **1997**, *275* (5303), 1102–1106.

(26) Daniel, M. C. M.; Astruc, D. Gold Nanoparticles: Assembly, Supramolecular Chemistry, Quantum-Size Related Properties and Applications toward Biology, Catalysis and Nanotechnology. *Chem. Rev.* **2004**, *104*, 293–346.

(27) Lee, P. C.; Meisel, D. Adsorption and Surface-Enhanced Raman of Dyes on Silver and Gold Sols. *J. Phys. Chem.* **1982**, *86* (17), 3391–3395.

(28) Qin, Y.; Ji, X.; Jing, J.; Liu, H.; Wu, H.; Yang, W. Size Control over Spherical Silver Nanoparticles by Ascorbic Acid Reduction. *Colloids Surfaces A Physicochem. Eng. Asp.* **2010**, *372* (1–3), 172–176.

(29) Dong, X.; Ji, X.; Wu, H.; Zhao, L.; Li, J.; Yang, W. Shape Control of Silver Nanoparticles by Stepwise Citrate Reduction Shape Control of Silver Nanoparticles by Stepwise Citrate Reduction. **2009**, *113* (March), 6573–6576.

(30) Meng, W.; Hu, F.; Jiang, X.; Lu, L. Preparation of Silver Colloids with Improved Uniformity and Stable Surface-Enhanced Raman Scattering. *Nanoscale Res. Lett.* **2015**, *10* (1), 34.

(31) Gao, R.; Choi, N.; Chang, S.-I.; Lee, E. K.; Choo, J. Real-Time Analysis of Diaquat Dibromide Monohydrate in Water with a SERS-Based Integrated Microdroplet Sensor. *Nanoscale* **2014**, *6* (15), 8781–8786.

(32) Dieringer, J. A.; McFarland, A. D.; Shah, N. C.; Stuart, D. A.; Whitney, A. V.; Yonzon, C. R.; Young, M. A.; Zhang, X.; Van Duyne, R. P. Introductory Lecture : Surface Enhanced Raman Spectroscopy: New Materials, Concepts, Characterization Tools, and Applications. *Faraday Discuss.* **2006**, *132*, 9–26.

(33) Camden, J. P.; Dieringer, J. a; Zhao, J.; Van Duyne, R. P. Controlled Plasmonic Nanostructures for Surface-Enhanced Spectroscopy and Sensing. *Acc. Chem. Res.* **2008**, *41* (12), 1653–1661.

(34) Shen, X. S.; Wang, G. Z.; Hong, X.; Zhu, W. Nanospheres of Silver Nanoparticles: Agglomeration, Surface Morphology Control and Application as SERS Substrates. *Phys. Chem. Chem. Phys.* **2009**, *11* (34), 7450.

(35) Yang, M.; Alvarez-Puebla, R.; Kim, H. S.; Aldeanueva-Potel, P.; Liz-Marzán, L. M.; Kotov, N. A. SERS-Active Gold Lace Nanoshells with Built-in Hotspots. *Nano Lett.* **2010**, *10* (10), 4013–4019.

(36) Rodríguez-Lorenzo, L.; Álvarez-Puebla, R. A.; Pastoriza-Santos, I.; Mazzucco, S.; Stéphan, O.; Kociak, M.; Liz-Marzán, L. M.; De Abajo, F. J. G. Zeptomol Detection through Controlled Ultrasensitive Surface-Enhanced Raman Scattering. *J. Am. Chem. Soc.* **2009**, *131* (13), 4616–4618.

(37) Rodríguez-Lorenzo, L.; Álvarez-Puebla, R. A.; García de Abajo, F. J.; Liz-Marzán, L. M. Surface Enhanced Raman Scattering Using Star-Shaped Gold Colloidal Nanoparticles †. *J. Phys. Chem. C* **2010**, *114* (16), 7336–7340.

(38) Diebold, E. D.; Mack, N. H.; Doorn, S. K.; Mazur, E. Femtosecond Laser-Nanostructured Substrates for Surface-Enhanced Raman Scattering. **2009**, No. 7, 1790–1794.

(39) Naumenko, D.; Stolzer, L.; Quick, A. S.; Abt, D.; Wegener, M.; Barner-Kowollik, C.; Dal Zilio, S.; Marmiroli, B.; Amenitsch, H.; Fruk, L.; Lazzarino, M. Design of Broadband SERS Substrates by the Laser-Induced Aggregation of Gold Nanoparticles. *J. Mater. Chem. C* **2016**, *4* (25), 6152–6159.

(40) Gopinath, A.; Boriskina, S. V.; Premasiri, W. R.; Ziegler, L.; Reinhard, B. M.; Negro, L. D. Plasmonic Nanogalaxies: Multiscale Aperiodic Arrays for Surface-Enhanced Raman Sensing. *Nano Lett.* **2009**, *9* (11), 3922–3929.

(41) Diebold, E. D.; Peng, P.; Mazur, E. Isolating Surface-Enhanced Raman Scattering Hot Spots Using Multiphoton Lithography. *J. Am. Chem. Soc.* **2009**, *131* (45), 16356–16357.

(42) Sundaramurthy, A.; Schuck, P. J.; Conley, N. R.; Fromm, D. P.; Kino, G. S.; Moerner, W. E.

Toward Nanometer-Scale Optical Photolithography: Utilizing the near-Field of Bowtie Optical Nanoantennas. *Nano Lett.* **2006**, *6* (3), 355–360.

(43) Gunnarsson, L.; Bjerneld, E. J.; Xu, H.; Petronis, S.; Kasemo, B.; Käll, M. Interparticle Coupling Effects in Nanofabricated Substrates for Surface-Enhanced Raman Scattering. *Appl. Phys. Lett.* **2001**, *78* (6), 802–804.

(44) Atay, T.; Song, J. H.; Nurmikko, A. V. Strongly Interacting Plasmon Nanoparticle Pairs: From Dipole-Dipole Interaction to Conductively Coupled Regime. *Nano Lett.* **2004**, *4* (9), 1627–1631.

(45) Stolzer, L.; Quick, A. S.; Abt, D.; Welle, A.; Naumenko, D.; Lazzarino, M.; Wegener, M.; Barner-Kowollik, C.; Fruk, L. Photo-Induced Surface Encoding of Gold Nanoparticles. *Chem. Commun.* **2015**, *51* (16), 3363–3366.

(46) Stolzer, L.; Ahmed, I.; Rodriguez-Emmenegger, C.; Trouillet, V.; Bockstaller, P.; Barner-Kowollik, C.; Fruk, L. Light-Induced Modification of Silver Nanoparticles with Functional Polymers. *Chem. Commun.* **2014**, *50* (34), 4430–4433.

(47) Taladriz-Blanco, P.; Buurma, N. J.; Rodríguez-Lorenzo, L.; Pérez-Juste, J.; Liz-Marzán, L. M.; Hervés, P. Reversible Assembly of Metal Nanoparticles Induced by Penicillamine. Dynamic Formation of SERS Hot Spots. *J. Mater. Chem.* **2011**, *21* (42), 16880.

(48) Guo, Q.-H.; Zhang, C.-J.; Wei, C.; Xu, M.-M.; Yuan, Y.-X.; Gu, R.-A.; Yao, J.-L. Controlling Dynamic SERS Hot Spots on a Monolayer Film of Fe3O4@Au Nanoparticles by a Magnetic Field. *Spectrochim. Acta Part A Mol. Biomol. Spectrosc.* **2016**, *152*, 336–342.

(49) Taladriz-Blanco, P.; Buurma, N. J.; Rodríguez-Lorenzo, L.; Pérez-Juste, J.; Liz-Marzán, L. M.; Hervés, P.; Rodriguez-Lorenzo, L.; Perez-Juste, J.; Liz-Marzan, L. M.; Herves, P.; Rodríguez-Lorenzo, L.; Pérez-Juste, J.; Liz-Marzán, L. M.; Hervés, P. Reversible Assembly of Metal Nanoparticles Induced by Penicillamine. Dynamic Formation of SERS Hot Spots. *J. Mater. Chem.* **2011**, *21* (42), 16880.

(50) Gehan, H.; Fillaud, L.; Chehimi, M. M.; Aubard, J.; Hohenau, A.; Felidj, N.; Mangeney, C. Thermo-Induced Electromagnetic Coupling in Gold/Polymer Hybrid Plasmonic Structures Probed by Surface-Enhanced Raman Scattering. *ACS Nano* **2010**, *4* (11), 6491–6500.

(51) Piantanida, L.; Naumenko, D.; Torelli, E.; Marini, M.; Bauer, D. M.; Fruk, L.; Firrao, G.; Lazzarino, M. Plasmon Resonance Tuning Using DNA Origami Actuation. *Chem. Commun. Chem. Commun* **2015**, *51* (51), 4789–4792.

(52) Kim, N. H.; Lee, S. J.; Moskovits, M. Reversible Tuning of SERS Hot Spots with Aptamers. *Adv. Mater.* **2011**, *23* (36), 4152–4156.

(53) Marini, M.; Piantanida, L.; Musetti, R.; Bek, A.; Dong, M.; Besenbacher, F.; Lazzarino, M.;

Firrao, G. A Revertible, Autonomous, Self-Assembled DNA-Origami Nanoactuator. *Nano Lett.* **2011**, *11* (12), 5449–5454.

(54) Knoll, B.; Keilmann, F. Enhanced Dielectric Contrast in Scattering-Type Scanning near-Field Optical Microscopy. *Opt. Commun.* **2000**, *182* (4–6), 321–328.

(55) Hillenbrand, R.; Taubner, T.; Keilmann, F. Phonon-Enhanced Light–matter Interaction at the Nanometre Scale. *Nature* **2002**, *418* (6894), 159–162.

(56) Alonso-González, P.; Albella, P.; Schnell, M.; Chen, J.; Huth, F.; García-Etxarri, A.; Casanova, F.; Golmar, F.; Arzubiaga, L.; Hueso, L. E.; Aizpurua, J.; Hillenbrand, R. Resolving the Electromagnetic Mechanism of Surface-Enhanced Light Scattering at Single Hot Spots. *Nat. Commun.* **2012**, *3*, 684.

(57) Neuman, T.; Alonso-González, P.; Garcia-Etxarri, A.; Schnell, M.; Hillenbrand, R.; Aizpurua, J. Mapping the near Fields of Plasmonic Nanoantennas by Scattering-Type Scanning near-Field Optical Microscopy. *Laser Photonics Rev.* **2015**, *9* (6), 637–649.

(58) Zhou, Z.; Xue, J.; Zheng, Z.; Li, J.; Ke, Y.; Yu, Y.; Han, J.; Xie, W.; Deng, S.; Chen, H.; Wang, X. A Centimeter-Scale Sub-10 Nm Gap Plasmonic Nanorod Array Film as a Versatile Platform for Enhancing Light–matter Interactions. *Nanoscale* **2015**, *7* (37), 15392–15403.

(59) Dubrovkin, A. M.; Adamo, G.; Yin, J.; Wang, L.; Soci, C.; Wang, Q. J.; Zheludev, N. I. Visible Range Plasmonic Modes on Topological Insulator Nanostructures. *Adv. Opt. Mater.* **2017**, *5* (3), 1–4.

(60) Thijssen, R.; Kippenberg, T. J.; Polman, A.; Verhagen, E. Plasmomechanical Resonators Based on Dimer Nanoantennas. *Nano Lett.* **2015**, *15* (6), 3971–3976.

(61) Schmid, S.; Wu, K.; Larsen, P. E.; Rindzevicius, T.; Boisen, A. Low-Power Photothermal Probing of Single Plasmonic Nanostructures with Nanomechanical String Resonators. *Nano Lett.* **2014**, *14* (5), 2318–2321.

(62) Knoll, B.; Keilmann, F. Near-Field Probing of Vibrational Absorption for Chemical Microscopy. *Nature* **1999**, *399* (May), 134–137.

(63) Thijssen, R.; Verhagen, E.; Kippenberg, T. J.; Polman, A. Plasmon Nanomechanical Coupling for Nanoscale Transduction. *Nano Lett.* **2013**, *13* (7), 3293–3297.

2 Fabrication and characterization of nanooptomechanical devices

This chapter is entirely dedicated to the description of the methods used throughout this project to fabricate, functionalize and characterize the devices. After an overview of the fabrication techniques involved in the making of the nanomechanical resonators, the functionalization of the devices with Raman-active molecules will be illustrated along with the techniques used to evaluate the properties of the devices.

2.1 Fabrication processes

The technology and methods used for the fabrication of the devices are those commonly used in the MEMS (Micro Electro Mechanical Systems) micromachining technology. Due to the sensitivity of the materials used in micro and nanofabrication to the effect of environmental parameters such as humidity, temperature, light, and dust, all the fabrication processes are performed in clean rooms. Clean rooms are specific areas with controlled ambient parameters, a strict access policy to avoid external contamination being brought by untrained users, and filtered illumination to block undesired light which can tamper with the quality of the lithography. The air inside the clean rooms is pre-treated and filtered to remove dust particles, with different degrees of purity depending on the requirements. In Table 2.1 the air quality values for different regulatory agency classifications is summarized:

FED STD 209E classification	**ISO 14644-1 classification**	**maximum number of particles/m^3**					
		≥ 0.1 µm	**≥ 0.2 µm**	**≥ 0.3 µm**	**≥ 0.5 µm**	**≥ 1 µm**	**≥ 5 µm**
Class 1	ISO 3	1000	237	102	35	8.3	0.29
Class 10	ISO 4	10000	2370	1020	352	83	2.9
Class 100	ISO 5	100000	23700	10200	3520	832	29
Class 1000	ISO 6	1000000	237000	102000	35200	8320	293

Table 2.1 - Clean room classification for FED STD 209E (USA) and ISO 14644-1 (EU) standard

The clean room facility where the fabrication processes have been performed have been built following the ISO 5 and ISO 6 standards, depending on the specific zone.

2.1.1 Silicon and SOI wafers

The most popular substrates for MEMS microfabrication are semiconductors; among those, the most common is silicon and its compounds. Silicon is a crystalline semiconductor used for decades in the integrated circuitry industry, even before the birth of the MEMS field, and is predominant also in the latter due to many reasons: it is a pure and cheap material, well characterized in its physical and chemical properties, with a large number of fabrication techniques already well-established; its mechanical and electrical properties can be adapted during the fabrication of the substrates, before the beginning of microfabrication processes, and silicon with different properties is available directly on the market; its compounds with oxygen and nitrogen, mainly silicon dioxide (SiO_2) and silicon nitride (Si_3N_4), have many different applications in the MEMS industry.
Silicon is commonly used in the microfabrication of MEMS in the shape of single-crystal wafers, which are disks of uniform thickness and homogeneous characteristics; the typical thickness of a silicon wafer is 500 μm. Depending on the crystallographic plane of the top surface of the wafer and its doping, wafers are identifiable using conventionally-placed cuts along their edge; this kind of marking is used by automated wafer handlers to orient the wafer in the correct position, if required.

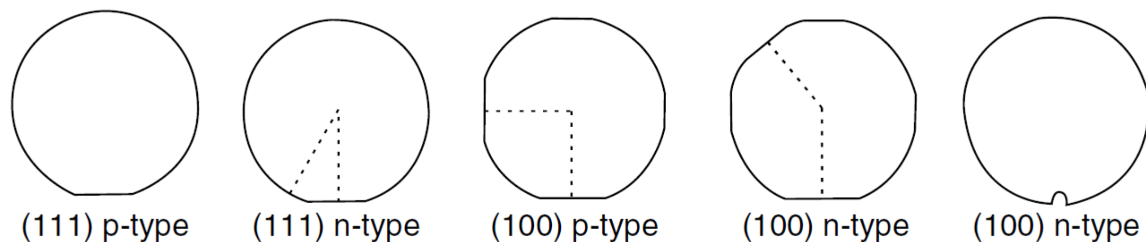

Figure 2.1 - Flat cuts and notches used to identify the doping and crystallographic orientation of a silicon wafer[1]*.*

On top of a silicon wafer, additional layers of materials can be added. For the use in MEMS micromachining, the most common additions are silicon dioxide and silicon nitride. A layer of silicon oxide is usually grown using thermal oxidation of the surface until the desired thickness is reached; silicon nitride, instead, is added to the surface of the silicon wafer using chemical vapour deposition (see § 2.1.2). Silicon wafers with silicon dioxide or nitride layers are used in the fabrication of MEMS with suspended or insulated structures and the typical thickness of these additional layers is in the range of 1 to 10 μm, even though values outside this range are possible. For this purpose, wafers with an oxide layer and an additional, thin layer of single-crystal silicon on top are also used; this kind of substrate is called Silicon-On-Insulator (SOI). The thickest layer of silicon, usually used as support or sacrificial layer, is called “handle”, while the thin layer of silicon on top is called “device”; silicon dioxide is found between these two silicon layers and is called BOX (Buried Oxide). The

handle layer thickness is usually comparable with the thickness of a conventional silicon wafer, while the thickness of the BOX and device layer are commonly in the range of 1 to 10 μm and 1.5 to 100 μm respectively, with lower and higher values possible for special applications.

2.1.2 Thin film deposition

After the selection of the appropriate substrate, one or both sides of the wafer must be covered with one or more layers of materials. Depending on the purpose, different materials can be used, each with its appropriate deposition method:

- *Spin coating* is a simple method for the deposition of polymeric uniform thin film. The sample is placed on a sample holder which holds it in position and coated with a solution of the polymer and its solvent; the holder can rotate at different angular speed (typically from 500 to 5000 rpm) causing the polymer solution to spread uniformly over the sample due to the centrifugal force. The thickness of the obtained film depends on different parameters (spin speed and acceleration, viscosity of the solution, volatility of the solvent, and wettability of the substrate) while the film quality is mainly determined by the cleanliness of the sample surface, its smoothness, the quality of the solution, the planarity of the sample holder during rotation, and the quality of the atmosphere. Dust particle in the air can deposit and be included into the spun film; therefore, the areas where samples are spin-coated should be those with higher clean room classes. After spin coating, the sample must be heated either on a hot plate or in an oven to evaporate part of the solvent and anneal the material stress of the polymer layer. Spin coating is the most used technique for the deposition of photoresists used in lithography.
- *Physical deposition methods* involve the removal of material from a solid source, either via evaporation or sputtering, and deposited onto the sample which is placed in high vacuum (below 10^{-6} torr) over or below the source. The material, usually inorganic, can be extracted from the source using evaporation: Joule heating from the flow of current through a metallic boat causes the thermal evaporation of the material, or an electron beam can be focused on the material source to cause localized heating and evaporation. Evaporation coating has deposition rates of 0.1-10 Å/s, which makes the roughness and thickness of the film highly controllable. The material can also be removed using DC or RF plasma for the physical milling of a target source, making it suitable for materials with too high melting point; the deposition rate is equal or higher than evaporation, but the quality of the film is less controllable. The films deposited with this method, called sputter coating, usually act

as masks or sacrificial layers for etching processes after the lithographic transfer of the pattern on the photoresist because they exhibit better adhesion than evaporated films.

- *Chemical deposition methods* involve the reaction of gaseous precursors of the material to be deposited over the surface of the sample in controlled conditions. The substrate is kept in high vacuum and the reaction is controlled changing the pressure, temperature, and gas flow. This technique allows the deposition of a wide range of materials, from dielectric materials (e.g. silicon nitride or silicon dioxide), to metals and simple polymers. To have a better control of the process and to lower the working temperature, the reactivity of the precursors with the surface of the substrate can be enhanced using inert or reactive plasma. This technique, known as plasma-enhanced chemical vapour deposition (PE-CVD), allows the deposition of materials with low melting points or on substrates with large differences in thermal expansion coefficient. Chemical vapour deposition methods create film that can be used as masks for etching processes or can directly be part of the final device.
- *Thermal oxidation* is the exploitation of the oxidability of silicon to obtain a controlled oxide (SiO_2) layer on top of a silicon wafer. Natural oxide layer aside, which is uncontrolled and a few nanometres thin only, an oxide layer above a silicon wafer is used in many fabrication processes as an insulating layer, a protective film, or a stopping layer for etching processes. The oxidation of silicon in presence of an oxygen-rich atmosphere at high temperature allows the growth of an oxide layer with controlled thickness and good uniformity. While the thickness of the oxide layer is time-dependent, the speed of the process can be controlled with two parameters, which can be changed together for the desired effect: reaction conditions and temperature. A higher temperature can enhance the speed of the process, but the stress introduced in the layer is higher, so more attention must be placed over the subsequent processes to reduce it e.g. annealing the oxidized wafer. The reaction speed can be also changed using dry or wet oxidation. Dry oxidation is obtained when only oxygen is flowed over the wafer, while for wet oxidation the addition of water vapor to the oxygen flow is required.

Dry oxidation reaction: $Si + O_2 \rightarrow SiO_2$

Wet oxidation reaction: $Si + 2H_2O \rightarrow SiO_2 + 2H_2$

Dry oxidation is slower and requires higher temperature, but the control over thickness is better and the film obtained is generally more uniform. Wet oxidation is a faster process, but the resulting oxide layer is more porous and less resistant to chemical treatments. The process to be used is selected depending on the purpose of the oxide layer.

2.1.3 Lithography

After the deposition of the appropriate film, the desired structure pattern must be transferred onto the substrate. The substrate is coated via spin coating with a material suited for the lithographic process of choice, pre-baked to improve the adhesion to the substrate and reduce material stress, exposed with the appropriate energy source (photons or electrons) and post-baked to evaporate the residual solvent, and improve the quality of the pattern. After post-baking, the photoresist must be developed to remove the coating from the appropriate areas and can then be used as a mask for the following fabrication steps. A schematic explanation of lithographic processes is shown in Figure 2.2.

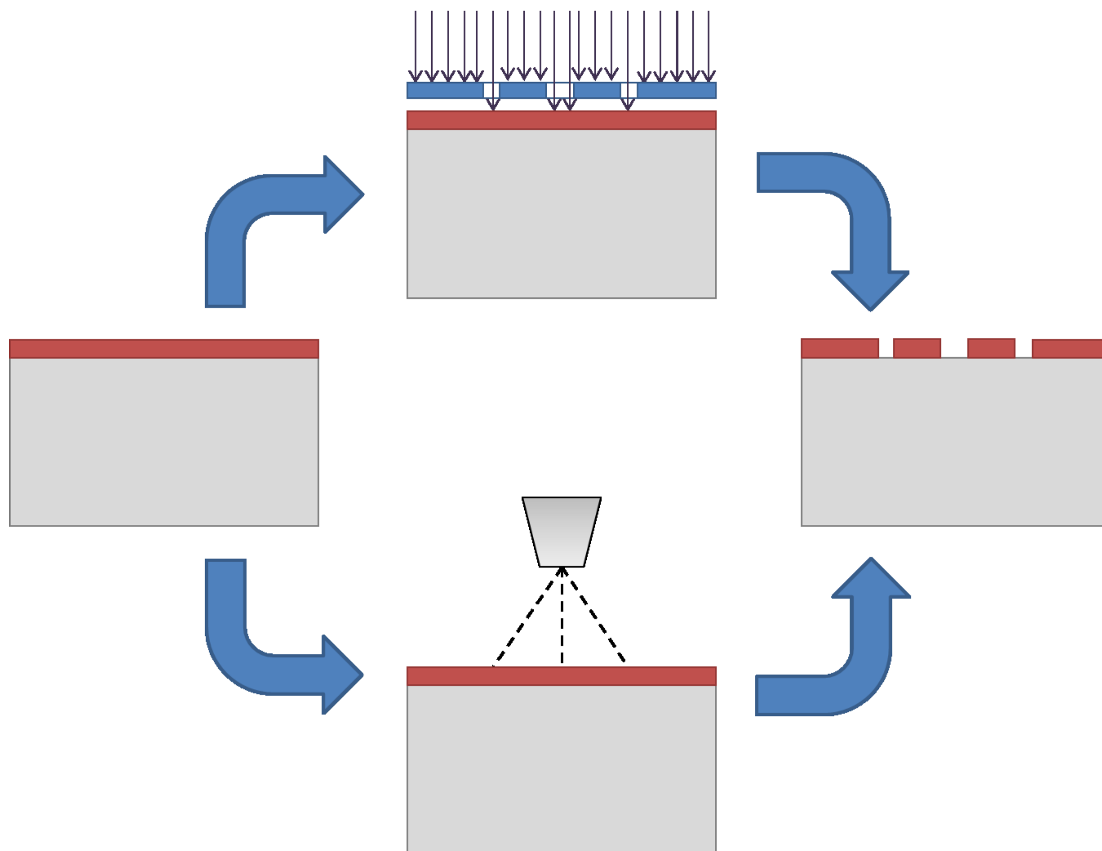

Figure 2.2 - Lithography schematic. The substrate (grey) is coated with photoresist (left, in red), exposed using optical (center top) or electron beam (center bottom) lithography and then developed to transfer the pattern to the resist (right).

2.1.3.1 Optical lithography

The most widespread technique for this purpose is optical lithography, in which the substrate is coated with a layer of light-sensitive material (photoresist), usually a polymer deposited via spin coating; a glass mask with a thin metallic pattern (either positive or negative, depending on the

photoresist and the following steps) is placed in close proximity or contact with the photoresist layer and exposed to light with the appropriate excitation wavelength to activate the resist. Using optical lithography and very high precision instrumentation it has been possible to achieve resolution as low as 10 nm for FinFET transistor technology[2].

The main classification for traditional optical lithography depends on the distance between the photoresist and the mask. When the mask is placed in close proximity with the photoresist we have *proximity exposure*: this way of patterning the photoresist has an intrinsic resolution limit that can be evaluated using the following equation:

$$R = 3\sqrt{\frac{\lambda}{n}\left(s + \frac{t}{2}\right)} \tag{2.1}$$

where R is the maximum resolution, expressed as the smallest feature that can be resolved, λ is the light wavelength, n the photoresist refractive index, s the separation between the mask and the photoresist and t the photoresist thickness. While all those parameters can be changed, they have different impacts on the overall feasibility of the process:

- The wavelength used to expose the resist can be reduced from the 435.8 nm of the highest band of a mercury lamp to less than 1 nm of X-rays; changing the light source from mercury lamps, to lasers for deep UV, to X-rays requires a huge economic and technological effort for the different instrumentation and mask design requirements and cannot be changed too much once the light source has been selected.
- The photoresist parameters (thickness and refractive index, t and n) can affect the resolution up to a certain degree and with enough flexibility to be changed according to the resolution required; while the smallest feature can be made bigger at will, it cannot be made smaller than the resolution limit of the optical system. Also, changing the photoresist can change the type of exposure required (positive or negative photoresist), in which negative or positive masks are needed.
- The separation distance between the mask and the photoresist (s) can change the resolution at the cost of process precision: the resolution of proximity exposure ($s > 0$) is lower and the alignment more difficult, but while contact lithography ($s = 0$) increases the resolution, it can cause sticking of the photoresist to the mask, introduce defects on the mask and scraping of the photoresist, all undesired phenomena that must be avoided.

More efficient techniques, such as immersion projection lithography, can increase the resolution of up to two orders of magnitude. The resolution doesn’t depend on Equation 2.1 anymore,

achieving the resolution limit of 10 nm mentioned earlier in this paragraph, but require special tools best suited for industrial mass production than research or prototyping. The biggest strength of the optical lithography relies in its scalability: with a single exposure a whole wafer can be patterned, thus shortening the fabrication process for large sample numbers.

2.1.3.2 Electron beam lithography

To overcome the limitations of conventional UV lithography without the need of more sophisticated light sources, electron beam lithography (EBL) has been implemented. Depending on the resist characteristics and stability of the apparatus, fabrication of nanostructures using EBL can have resolutions below the limit of 10 nm[3].

The protocol for EBL is similar to conventional UV lithography; after the spin coating of the substrate and the soft baking step, the sample is placed into the vacuum chamber of a scanning electron microscope (SEM) equipped with a pattern generator and a motorized XY stage. The patterning doesn’t require any kind of mask because the design of the structures is directly fed to the pattern generator which scans the sample under the electron beam. The main drawback of this process, which makes EBL unsuitable for mass production application, is the time required to transfer the pattern on the photoresist: the larger the pattern and the smaller the features, the higher the time required for the exposure. The patterning of a whole wafer can take up to several days of continued machine time, with all the related concerns, such as thermal stability of the resist, solvent evaporation, instrumental drift of the positioners, beam stability, and such. Nowadays, the most suitable application for EBL fabrication is research or prototyping, even though EBL-dedicated machines uncoupled from the SEM can achieve better performances in terms of total exposure time and repeatability.

2.1.4 Lift-off

After the development of the photoresist, the patterned area is made of zones covered and uncovered from the photoresist. One of the most effective techniques to obtain a mask on the uncovered parts of the substrate is the so-called lift-off. The patterned substrate is coated with a thin film of a sacrificial material, usually a metal such as chromium, which covers both the exposed and unexposed areas; by immersing the pattern into the appropriate solvent, the resist that persists below the sacrificial layer starts to be removed, bringing the metal along and leaving only unexposed areas covered. The resolution obtained with this technique is high, but the shape of sharp structures, such as triangle tips or rectangular corners, can be rounded in the process. Special care must be put into the agitation of the solvent and the timing, because improper procedures can

lead to redepositing of lifted material over random areas of the substrate, creating unwanted masked areas or even covering parts of the pattern.

2.1.5 Wet and dry etching

The etching process is the one which transfers the two-dimensional pattern of the surface to the three-dimensional substrate underneath. The pattern can be obtained removing material only from exposed parts of the substrate, while others are protected by a mask, usually made of metal or oxide. This result can be achieved with two different approach, depending on the physical state of the etchant.

Wet etching uses solutions that react selectively with the material that needs to be removed; those chemical solutions (etchants) should in principle remove the target material exposed by the pattern lithography without affecting the mask and the covered parts below it. Wet etching is most commonly used to transfer a pattern to a chromium mask, using a solution of ammonium cerium nitrate in diluted acetic acid or iron cyanide in diluted potassium hydroxide, or to etch silicon either isotropically or anisotropically.

The isotropy of the etching is an important parameter for the choice of the etchant: some solutions have different reaction speed depending on the crystalline plane of the material and this must be addressed properly during the design of the lithographic masks and patterns. Silicon, for example, can be etched isotropically using HNA, a solution of acetic, nitric and hydrofluoric acid, but isotropic etchants also cause underetching and loss of resolution; anisotropic etchants, like potassium hydroxide (KOH) or tetramethylammonium hydroxide (TMAH), on the other hand, follow the crystalline orientation of the silicon and avoid or strongly reduce underetching. Anisotropic etching of silicon can be used to obtain deep structures with steep walls, but the final dimension of the structure at the bottom of the etched portion depends on the depth of the structure itself and is always smaller than the starting pattern. The wet etching of thin films, like metals or oxides, is usually isotropic: due to the reduced thickness of these layers, underetching is either negligible or exploitable to obtain suspended structures.

Dry etching is a physical, more complex method of material removal. The sample is put in high vacuum and then exposed to a plasma of reactive species (hence the name of Reactive Ion Etching – RIE) which remove material from the surface. This process is often used to etch silicon and its compounds, such as silicon dioxide and silicon nitride. The anisotropy and speed of the process can be controlled balancing the process parameters: chamber pressure, etchant species and flow, and electrical field (bias). The plasma of reactive species can sometimes be coupled with inert plasma to enhance the physical milling effect, thus increasing process speed. The most used reagents for

RIE processes are sulphur hexafluoride (SF_6), which cause the isotropic etching of silicon, and carbon tetrafluoride (CF_4), which can be anisotropic to the point of obtaining vertical walls. The anisotropy and resolution performances of this process are limited to depth of up to ten microns and aspect ratios of up to 10:1.

To improve the conventional RIE performances, deep RIE (DRIE) processes are currently employed. An example of DRIE process is the so-called Bosch process (patented in 1994 by Bosch): the etchant species is SF_6, and plasma is inductively coupled to hit, and react upon, the horizontal surfaces of the substrate. After the etching step, CF_4 is flowed instead of SF_6 and the deposition of a thin passivation layer occurs, and then another etching step removes the passivating layer from the horizontal surface without affecting the passivated vertical structures. Alternating repetitions of etching and passivation steps are capable of etching structures with very high aspect ratio (up to 100:1) and vertical walls with no significant loss of resolution; the main drawback of this process is the formation of scallops, due to the isotropic SF_6 etching steps, along the walls of the structures (Figure 2.3).

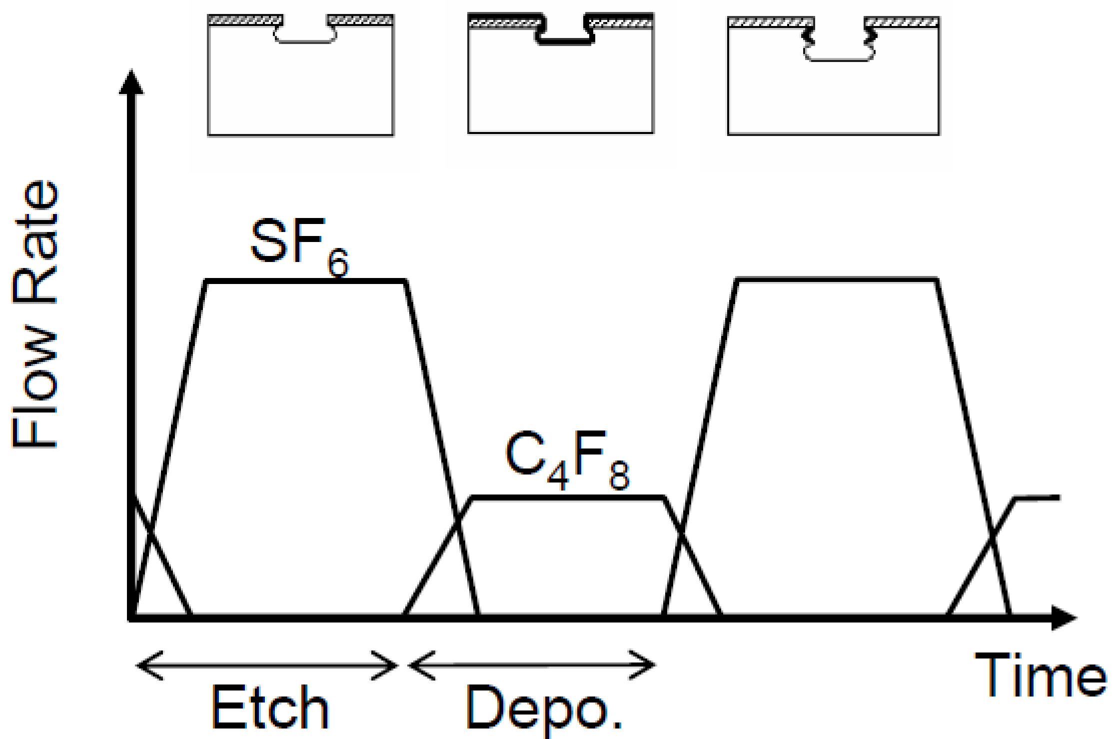

Figure 2.3 - Bosch process schematization: after each etching step, a portion of material is isotropically removed, forming the peculiar scallops (above), while the deposition steps coat the sides with a thin passivation layer (above, dark lines).

Wet and dry etching can be characterized in terms of etching speed, isotropy, and selectivity; the selection of the appropriate process to obtain the desired results is based on these three parameters, and the required resolution and aspect ratio of the structures must be also taken into

account. The example of silicon etching will be used below to illustrate the different effect of these parameters.
The etching of the same substrate can be either isotropic or anisotropic, depending on the solution. Anisotropic etching of silicon can be achieved either with dry or with wet etching, with different results. Anisotropic wet etching of silicon is obtained using a solution of potassium hydroxide (KOH), an etchant which removes material from a silicon substrate at different speeds depending from the crystallographic plane. KOH etching on a silicon {100} wafer proceeds faster along the <1 0 0> (horizontal) planes and much slower along the <1 1 1> planes, which are oriented at 54.7° from the <1 0 0> direction, creating tilted sidewalls; the horizontal etched area decreases in size along with the depth of the etching. On the other side, isotropic etching of silicon can be obtained using HNA solution, a mixture of Hydrofluoric, Nitric and Acetic acid with 4:7:11 ratio: this etchant can erode silicon independently from all crystallographic planes, leading to round-shaped profiles. Dry etching of silicon, typically using ICP-RIE, can be either isotropic or anisotropic: this parameter is controlled by the changing the ratio between the passivation and etching gas (CF4 and SF_6 respectively).
The etching speed is also determined by the process used. Wet etching of silicon can be as fast as 3 to 5 μm/minute, with high variability, due to reaction conditions such as temperature and substrate cleaning, and peaks of >10 μm/minute. The etch rate for dry etching processes is generally lower, ranging from 0.2 to >10 μm/minute, and can be controlled by varying the process parameters: power and gas flow must be adjusted correctly to avoid excessive passivation, which would eventually stop the process, or (for Bosch-like processes) by the speed of a single process cycle.
Selectivity is also an issue for etching processes: since microfabrication involves the transfer of a pattern on the substrate or part of it, the patterned zones (or their negative) must be protected from the etching effects. To protect the pattern features, resist or metal masks are used; the pattern can also be transferred to different layers instead of the silicon substrate (e.g. on silicon oxide or nitride layers) which must resist the sacrificial layer etching, a process mostly applied to the release of suspended structures. Most wet etching processes show good selectivity, since the chemistry of the etchant can be tuned to attack the substrate only; the most common example is KOH etching, which has an average selectivity of 200:1 for silicon over silicon dioxide, which is then used as a protective layer. The selectivity of dry etching is usually an order of magnitude lower for silicon over its compounds, so resist masks or metal films are used to protect the substrate from unwanted etching. The durability of the mask during etching processes must be carefully controlled, since damaging the mask can introduce errors – or even completely destroy – the pattern to be fabricated.

Wet and dry etching have different resolution performances. Wet etching is used when the smaller feature size is limited to tens of microns, since the control over undesired phenomena such as under- or overetching is poor. Dry etching processes are better suited for high resolution, so they are the most widespread in the nanofabrication field.
Both kinds of process are influenced by the aspect ratio of the structures: structures with high aspect ratio can hinder the diffusion of reactive species towards the surface of the substrate, thus slowing down the process, while (in particular for isotropic etching) the ongoing etching creates larger exposed substrate areas leading to slightly faster etching. Even though these two effects are less pronounced for dry etching processes, they are not immune from them; there are some tricks which can help in reducing them for dry etching, which usually decrease selectivity, etching rate, or resolution, but their effect must always be accounted for.

2.1.6 Suspended structure release – supercritical point drying

The final step of a fabrication process is the rinsing and drying of the device; when everything is planar, or at least adherent to the substrate, no problems arise during this step. However, when the release of micrometric or nanometric suspended structures is required, drying can lead to a relevant issue. The most common solvent, water, forms a meniscus when filling the gaps of the sample and undergo a density change during drying; this causes the increase of surface tension and the deformation of the meniscus, which can bend suspended structures until they stick to another surface – or even break. To avoid this problem, several techniques have been developed; one of them is the supercritical point drying. In this technique, the sample is immersed in a low surface tension solvent, like acetone or ethanol, and placed in a dedicated chamber while still wet, which is flooded with liquid CO_2: liquid CO_2 slowly replaces the solvent and, by raising the temperature and pressure over the critical point (hence the name of the technique), it evaporates without causing almost any stress to the suspended or fragile structures in the sample.

2.2 Surface functionalization

The steps described above for the fabrication of a device are enough to obtain a working MEMS in terms of electrical and/or mechanical features; specific behaviours for sensing applications, or the coupling between those features and other properties like chemical sensitivity or selectivity, require the functionalization of some or all surfaces of the devices. The most common methods for surface functionalization are described below.

2.2.1 Evaporation

Using a process like the one described earlier for thin film deposition in microfabrication processes, organic molecules can be evaporated from a source and be deposited in thin films over the surface of the devices. To ensure a uniform coating on 3D structures, a method called glancing angle deposition (GLAD) is used. In GLAD, the sample is not normal to the evaporation source but is kept inclined at different angles: the inclination determines the amount of shadowing effect due to vertical surfaces of the samples. The angle can be changed to fit different coverage requirements. In some configurations that require more uniform coatings, a stepper motor keeps the sample revolving over the source to expose all the differently oriented surfaces evenly during the process. While this process has been developed for the creation of sculptured thin films[4] (*i.e.* thin films with controlled porosity, orientation and nanostructure), it has been applied successfully in the deposition of thin films of polymeric materials over structures with complex shapes without the need of a specific chemical reaction to occur on the surfaces. The main limitation is due to the shadowing effect, which hinders the formation of a uniform layer from top to bottom of vertical structures with high aspect ratios; the choice of materials that can be used for functionalization via evaporation have the same limitations already described for physical vapour deposition processes.

2.2.2 Immersion and dip coating

An easier method for the functionalization of surfaces is immersion or dip coating. The basic principle is the same: the sample is placed in a solution of the desired functional molecules or their precursors and left to react inside the solution. While in the simple immersion coating the sample is left inside the solution waiting for the reaction to take place, in dip coating the sample is immersed and subsequently pulled out of the solution (Figure 2.4). This creates a thin layer of fluid on the walls of the sample whose thickness is determined by the pulling speed and the viscosity of the solution; the solvent contained in the layer evaporate is allowed to evaporate, leaving only the reacted molecules on the surface. A uniform coating can be obtained, or the thickness of the coating changed, repeating the immersion-pulling-evaporation sequence.

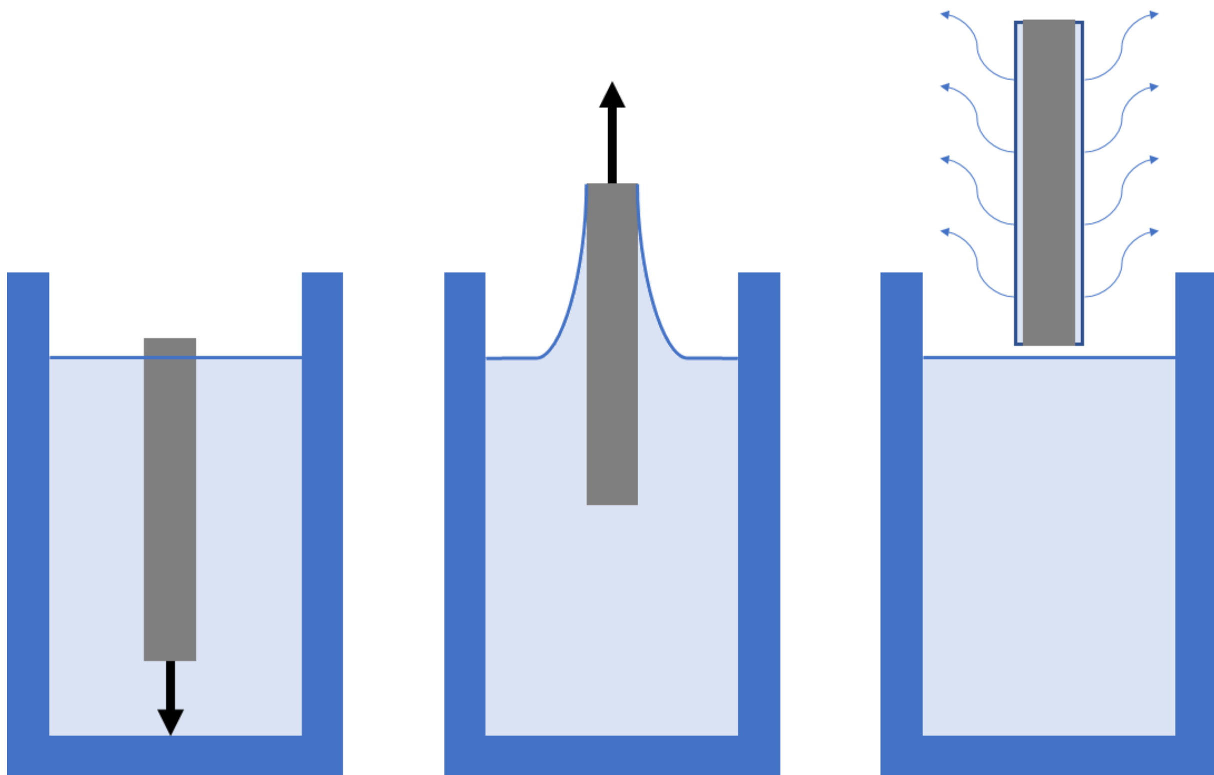

Figure 2.4 - Dip coating process schematization. The sample is immersed in the solution (a), pulled out at constant speed (b) and dried (c).

A special kind of functionalization where these two techniques are frequently applied is the formation of self-assembled monolayers (SAM). The formation of a SAM over the surface of a device requires special tuning of the chemistry, and different mechanisms are involved depending on the base group which reacts with the surface. For example, thiolated molecules (*i.e.* molecules terminated with a -SH group) react very well with gold and silver surfaces, they have a two-step kinetic which slows the process down and can create non-uniform coverage of the surfaces; silanes and siloxanes (molecules terminated with a $-SiH_3$ or -SiOOH group), on the other hand, interact with each other to form a reticulated structure, are more stable but need specifically activated structures to be bound.

Dip coating is particularly suited for this application because it can provide a fine control over solvent evaporation rate, avoiding or greatly reducing random multilayer stacking.

2.3 Characterization methods

The result of the fabrication and functionalization of a device must be verified prior to the real application. There are several techniques that can be employed for this purpose, depending on the properties to investigate: morphological, mechanical, or chemical. In the following paragraph, a description of the techniques used throughout the project will be given.

2.3.1 Morphological characterization of devices

The most common type of morphological characterization is imaging. This can be done in different ways, depending on the illumination source and detected particle.

For rapid control of the quality of the structures during the fabrication, conventional optical imaging with a microscope can be used. A broadband light source illuminates the sample through an objective, which also collects the reflected light and conveys the image to oculars or CCD cameras. Filters can be applied to the light source to avoid accidental exposure of the resist if the quality control is done before developing; the maximum resolution is limited by the diffraction of the light and can be estimated using the radius of the spot of light in the focal plane. This radius can be calculated using the Abbe equation:

$$r = \frac{\lambda}{2n\sin\theta} = \frac{\lambda}{2\,NA} \tag{2.2}$$

where λ is the wavelength of the light, n the refractive index of the medium between the objective lens and the sample, ϑ the half-angle formed by the convergent beam of light. The product $n \sin \vartheta$ is also called numerical aperture (*NA* in the second part of equation 2.2) and is an intrinsic parameter of the microscope objective.

For higher resolution imaging, the use of a scanning electron microscope (SEM) is more appropriate and straightforward. The sample is placed in a vacuum chamber and kept at very low pressure (below 10^{-6} torr) to avoid scattering from dust and air molecules; an electron beam is generated, collimated and focused through an ultra-high vacuum (below 10^{-10} torr) column and then it scans a small portion of the sample. Imaging is done acquiring the secondary electrons emitted from the atoms excited by the e-beam; their number and energy strongly depend on the surface topography, thus enabling a reconstruction of the morphology of the sample. Backscattered electrons can also be collected using different detectors and, while the morphological information can be less precise, they provide a simple material recognition: the intensity of the signal coming from backscattered electrons depends mostly on the atomic number of the material under analysis.

Chemical information can be obtained using energy-dispersive X-ray spectroscopy (EDXS) techniques: a detector is added inside the specimen chamber, which is sensible to the X-ray photons emitted by the sample when the e-beam of the SEM hits. An accelerating voltage inside the detector can convey the photons with different energies to the sensing element and, with appropriate data analysis, it is possible to evaluate the composition of the sample. The most recent software for EDXS analysis allows the chemical mapping of the sample.

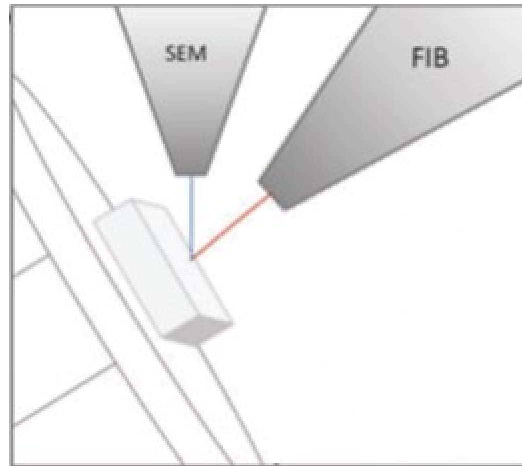

Figure 2.5 - SEM and FIB coupled analysis. The sample is tilted at the angle between the SEM and FIB columns in order to have perpendicular milling from the ion beam, while SEM imaging is software-corrected to compensate the tilting angle. Adapted from Earl et al[5].

An analogue to the SEM principle is the focused ion beam (FIB) analysis. A beam of metal ions (usually gallium, extracted from a liquid reservoir) is focused through an ultra-high vacuum column towards the sample; due to the high energy and mass of Ga^+ ions, this technique is destructive for the sample when used for imaging. The main application of FIB for morphological characterizations is the ability to deeply cut the sample in specific portions, in order to expose the internal layers and allow the inspection of the devices in section; it can also be used for atomic layer deposition of thin films of different materials in specific areas, or the direct patterning of surfaces via physical milling of the material. A FIB is often coupled with an SEM column as depicted in Figure 2.5, to allow non-destructive imaging of the sections created, to verify the quality of the patterning or have a live control of the FIB operation on the sample.
The interaction of SEM, FIB and EDXS analysis can give detailed, in-depth information about micro and nanofabricated devices.

2.3.2 Mechanical characterization of devices

Resonating devices, such as microcantilevers and micropillars, can be used as sensors in two different ways: in static mode and in dynamic mode. While each of these operation modes have its own advantages and disadvantages, only the latter will be described for its relevance for this thesis project.
To operate a resonator in dynamic mode, an external force must be applied to induce oscillations in the structure; the most efficient way to achieve this motion is to apply a sinusoidal driving force at the resonant frequency of the device. Operating at resonant frequency ensures that the drive-

induced motion is naturally amplified by the device, thus requiring a very small amount of energy to get wide oscillation amplitudes.

During the project step of a resonator, its resonant frequency must be at least estimated to predict its behaviour or to select the appropriate geometrical parameters for the fabrication. A simple estimation of the resonant frequency (*f*) for a cantilever can be obtained using the following equation[6]:

$$f = \frac{3.52}{2\pi} \cdot \sqrt{\frac{E}{\rho}} \cdot \frac{h}{l^2} \qquad 2.3$$

where E is the Young's modulus of the material, ρ its density, *h* the thickness of the cantilever and *l* its length. To account for the presence of a tip (approximated to a conical shape), when appropriate, Equation 2.3 can be replaced by[7]:

$$f = 0.276 \cdot \sqrt{\frac{E \cdot w \cdot h^3}{\rho \cdot \left(\pi \cdot h_{tip}^3 \cdot l^3 + 2.832 \cdot w \cdot h \cdot l^4\right)}} \qquad 2.4$$

In which the term h_{tip} represents the length of the tip and w the cantilever width. Using equations 2.3 and 2.4 it is possible to have a first esteem of the resonant frequency of a cantilever, which can be made more precise using finite-element modelling (FEM).

FEM is a computational technique which employs a geometrical model of the device and divides it into a grid of very small elements (a mesh); on each of the mesh elements the desired equations are applied on the boundary conditions between mesh elements and the sum of all the units gives the result for the whole structure. With this kind of software, it is possible to achieve high level of precision for the simulation of the behaviour of a wide range of structures and devices, from huge structures, to mechanical pieces, to MEMS, to nanostructures.

After the device fabrication, it is important to determine its real resonant frequency. Starting from the frequency esteem calculated using equation 2.3 or 2.4, and further improved by FEM, a range of possible frequencies can be identified. An external force is then applied to the resonator, whose motion can be detected using different methods.

A resonator can be actuated using different methods; the most widespread employs a piezoelectric element mechanically coupled with the device holder, or with the substrate on which the device is fabricated. This method is commonly used in scanning probe microscopes, such as atomic force microscopy (AFM) systems. Recently, the actuation of a resonating element through photothermal processes by illuminating a portion of a cantilever close to the clamped end with a pulsed near-

ultraviolet or blue laser[8]. The heat transfer phenomena resulting from the illumination close to the base of the resonator are responsible for the external driving force required to actuate it, thus demonstrating the need for very low driving forces when the resonator is actuated at its resonant frequency. This technology has been successfully applied in commercial AFM devices, e.g. by Asylum Research[9], to improve the stability of piezoelectric actuation in high-damping applications. The motion of a resonator can be detected, among other methods, using the optical lever technique. This is the most widely used method, commonly applied to AFM systems and sketched in Figure 2.6.

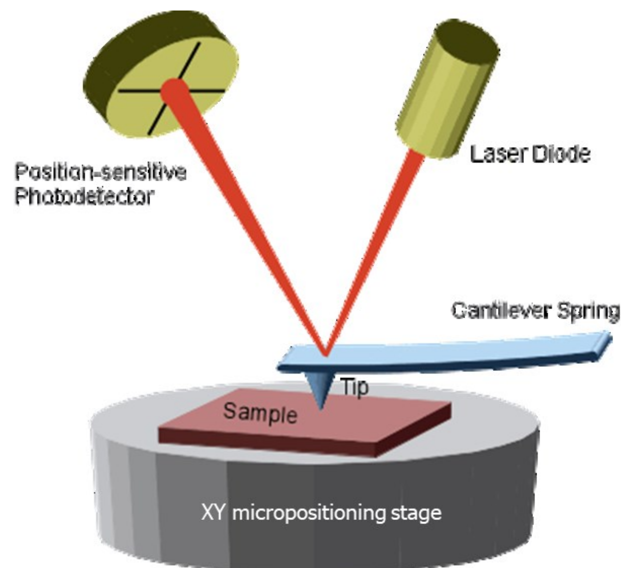

Figure 2.6 - Optical lever method scheme applied to an AFM system with cantilever, tip and sample scanner.

In the optical lever method, a collimated laser beam is directed upon the free end of the resonator (or, for double-clamped beams, to the point of maximum deflection, usually the middle of the beam) and its reflection is sent to a detector, that can be a 2- or 4-quadrant photodiode or a position-sensitive detector (PSD); the distance between the resonator and the detector is usually much higher than the oscillation amplitude, to amplify the motion of the device. After positioning the detector to have a reference signal (usually 0 V) when the resonator is not actuated, the signal variation during actuation is recorded. When the laser moves from the centre position, corresponding to the 0 V reference, each quadrant will be hit by a portion of the laser spot; the movement of the cantilever can be tracked measuring the differential voltage between the top and bottom section for vertical deflections and between left and right section for horizontal deflections (see Figure 2.7 for a schematic example related to a four-quadrant photodiode).

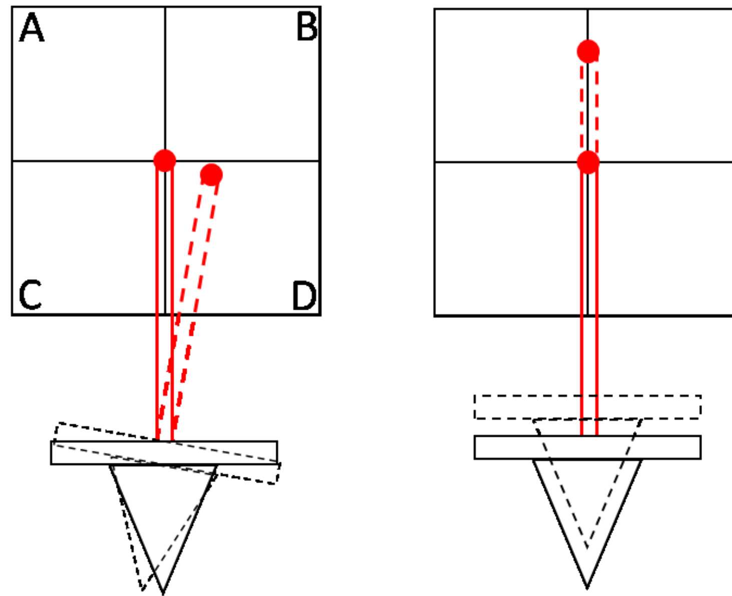

Figure 2.7 - Schematics of cantilever tracking with a 4-quadrant photodiode: each sector of the photodiode generates a voltage signal proportional to the distance from the centre of the sensor. The tilting of the cantilever (left) is detected measuring the differential voltage between the signal from sectors (B+D) and (A+C), while the vertical deflection (right) is detected measuring the differential voltage between the signal from sectors (A+B) and (C+D).

The resonance of the device is determined scanning the actuation frequency and analysing the detector response in magnitude and phase with a network analyser or a lock-in amplifier. The amplitude/phase response of a resonator in resonant conditions is identifiable from two features: a more or less sharp peak (or dip) in amplitude that can be fitted with a Lorentzian function, and a flexus point in phase, either with positive or negative slope (Figure 2.8).

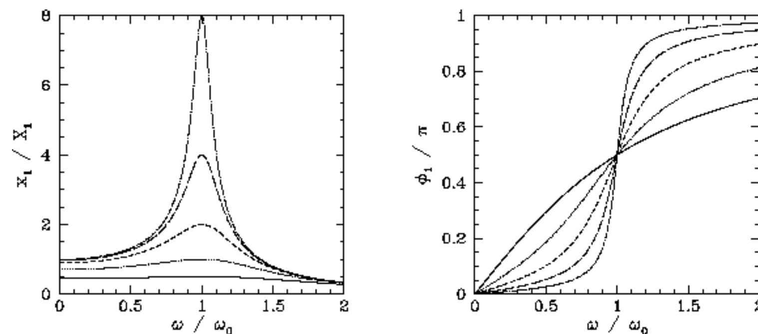

Figure 2.8 - Amplitude (left) and phase (right) resonance for varying amplitude of the external force in low damping conditions (adapted from Fitzpatrick[10]).

After the value of the resonant frequency has been identified, the actuation intensity can be varied in order to get the mechanical response of the device at different amplitudes. This can be done as shown in Figure 2.8, varying the amplitude of each frequency scan, or fixing the frequency at the resonance value and scanning the amplitude. This second method is useful when there is the need to understand the displacement of the resonator at different actuation forces.

2.4 Fabrication and characterization protocols

The working principle of the devices can be similarly described: an oscillator is fabricated facing a steady structure and both are coated with a thin film of gold; when the oscillations of the resonator drive the free end of the resonator in close proximity to the wall, with the proper excitation a hot spot can be created in the contact point. A sketch of the working mechanics is shown in Figure 2.9

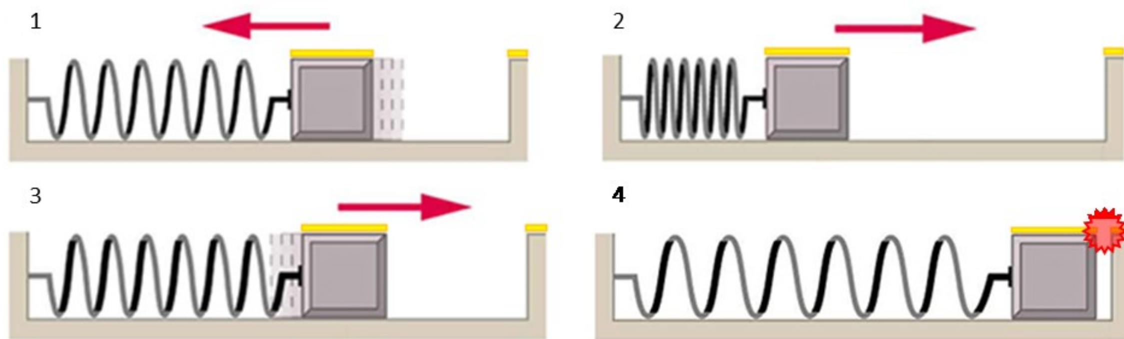

Figure 2.9 - Working principle of the optomechanical resonator: the oscillating structure is put in resonant conditions and pulled away from the steady wall (1); the elastic force pushes the free end of the resonator towards the wall again (2, 3) until the distance is small enough to achieve quasi-contact condition and create the hot spot under laser illumination (4).

Such a system can be characterized in its main features: the resonant frequency of the oscillator, the strength of the actuation required to achieve quasi-contact condition, the presence of the hot spot, and its precise location. These parameters require different characterization techniques and equipment, described in the following paragraphs.

The optomechanical resonators that are the object of this project have been fabricated using the techniques described in the previous paragraphs. Two different versions of the devices have been fabricated and functionalised throughout the project, with the second version designed to overcome the problems arisen with the first one.

The first version of the device makes use of a vertical resonator (pillar) in close proximity to a steady structure, forming a common configuration for impact oscillators. The separation distance between the resonator and the wall is 100 nm, far enough to avoid the spontaneous formation of hot spots in static mode. This version of the device will be referred to as “pillar device”.

The second version of the device features a suspended cantilever with a high width to height aspect ratio, to have the first natural resonant mode oscillation along the XY plane, in front of a steady structure. The resonating arm also features a triangular tip to have a well-defined contact point between the resonator and the steady wall to have a well-defined contact point. This second version will be referred to as “cantilever device”.

2.4.1 Fabrication of the devices

The two devices share the same approach, even though they start from different substrates, with only one additional step required for the fabrication of the second version.

The substrate chosen for the fabrication is a silicon [1 0 0] wafer (500 mm) for the pillar device, and a silicon-on-insulator (SOI) wafer with a handle layer of silicon [1 0 0] (500 μm), a silicon oxide (buried oxide - BOX) layer (2 μm) and a device layer of silicon [1 0 0] (15 μm) for the cantilever device.

A thin film of polymethylmethacrylate (PMMA AR-P 950K 671.05) is spin coated at 5000 rpm for 1 minute over one side of the wafer (one of the polished sides for the first version, the device layer for the second) and soft-baked at 180°C for 5 minutes. PMMA is a positive, electron-sensitive photoresist used in electron-beam lithography. The coated substrate is placed on a sample holder and introduced in the specimen chamber of a LEO 1540XB cross-beam scanning electron microscope equipped with a Raith pattern generator and beam blank controller. The pattern is directly written on the coated substrate using an e-beam acceleration voltage of 30 kV and the proper exposure parameters evaluated with dose matrix tests specific for each device version. After the exposure, the resist is developed immersing the wafer in a solution containing methyl-isobutyl ketone and isopropyl alcohol (MIBK:IPA) with 1:3 v/v ratio until fully developed and then immersed and rinsed in DI water. The exposition and development of the positive resist creates holes in the resist layer with the same shape of the structures.

The patterned photoresist is coated with a thin layer of chromium (30-50 nm) using DC sputter coating and the excess chromium is removed using a standard lift-off process in hot acetone until complete removal of the PMMA, leaving only the pattern of the structures in chromium over silicon.

The chromium layer acts as a mask for the Bosch-like etching process performed in an ICP-DRIE (STS-Surface Technology); the substrate is etched until the desired height (first version) or the BOX layer (second version) is reached. The Bosch-like process principles have been already described in § 2.1.5 above; each device has been fabricated using its own optimized combination of process parameters (gas flow, pressure, power) during the passivation and the etching phase. The difference in the IPC-RIE parameters is related to the different desired results; while the recipe used for the pillar device ensures the presence of the underetching on one side of the pillar to obtain the characteristic inverted tapering, the recipe for the cantilever device is aimed towards a more regular, vertical etching, even though it is impossible to eliminate the underetching effect completely.

After the fabrication, the pillar device is coated with a thin film of Cr/Au (2:40 nm thick) by thermal evaporation. Chromium acts as an adhesion layer to ensure proper attachment between the gold

layer and the devices. The evaporation direction was tilted 45° off the normal direction and moved along four orthogonal directions on the azimuthal plane in order to deposit the metal layer on the pillar and wall sides[11].

The cantilever device has a suspended resonating arm that must be released before the gold layer deposition; this is done immersing the sample in a diluted hydrofluoric acid solution ($HF:H_2O$ 1:10) which selectively and isotropically etches silicon oxide. After the release of the suspended structures, the devices are rinsed immersing them in DI water and gently dried under a low flux of nitrogen, to avoid damages to the resonating arms. A limited under-etching of the non-suspended parts of the structures is also observed but no influence on the stability of those parts of the structures has been recorded, mainly due to their width. The final fabrication step is the deposition of a thin Au film (50 nm). It has been demonstrated in literature that a chromium adhesion layer is detrimental for the plasmonic properties of nanostructures[12], so a different evaporation protocol is developed: gold is directly deposited on silicon by e-beam evaporation, to ensure a better adhesion without the need of the chromium layer for the increased purity of the material.

2.4.2 Functionalization of the devices

The fully-fabricated devices have gold surfaces which can exhibit plasmonic hot spots during actuation; to verify the hot spot formation and demonstrate the SERS effect of this plasmonic phenomenon, Raman-active molecules are deposited on both versions of the devices.

For the pillar devices, pentacene is chosen as the Raman reporter molecule. Pentacene is a polycyclic aromatic hydrocarbon consisting of five linearly-fused benzene rings which exhibit a well-recognizable Raman spectrum.

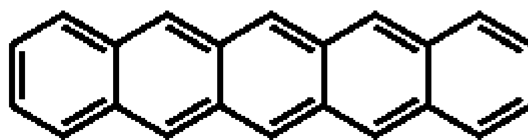

Figure 2.10 - Skeletal formula of the pentacene molecule.

It is solid at room temperature and therefore can be evaporated on the devices; we used this method to functionalize the devices with a protocol analogue to the one used for the evaporation of the Cr/Au layer (with 30° instead of 45° tilting angle, 2 nm per azimuthal position). Pentacene also has a strong absorption of light in the visible range, more pronounced for red wavelengths. The absorption spectrum structure is demonstrated to be, for the purpose of this project, thickness-independent[13].

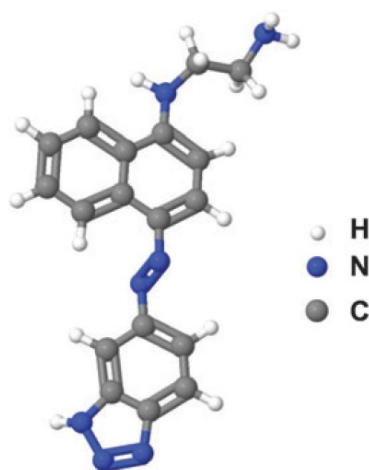

Figure 2.11 - Molecular structure of the BT-Azo dye.

The cantilever device is functionalized with a different molecule: benzotriazole-azo (BT-Azo) dye (Figure 2.11). This molecule has a strong Raman signal, is suitable for SERRS experiments and has a benzotriazole anchoring groups which facilitates the deposition over the surface of noble metals[14]. The cantilever devices are functionalized through overnight immersion in a 1 nM solution of BT-Azo in methanol, followed by gentle rinsing with fresh methanol to remove excess dye and drying in a low flow of nitrogen.

2.4.3 Characterization of the devices

Both the versions of the optomechanical devices were tested for resonant frequency and actuation voltage-dependent behaviour. The pillar device has been characterized both in vacuum and in air, while the cantilever device didn't undergo vacuum characterization.
The devices are used in dynamic mode throughout the experiments, so an actuation source must be used to excite the samples to their resonant frequency. For this purpose, the samples are mounted on piezoelectrical actuators; those are lead zirconate titanate crystals (EBL #2 RECT, EBL Products, Inc.) usually cut in 5x5 mm^2 square pieces, electrically connected to an arbitrary function generator (Agilent 33120A 15 MHz) which can provide actuation voltages of up to 10 V_{pp}.

2.4.3.1 Mechanical characterization of the pillar device

When measured in vacuum, the samples are placed in a chamber with an optical window and feed-through contacts for the actuation of the piezoelectric crystals. The vacuum in the chamber is obtained with a multi-roots dry pump (ALCATEL Adixen ACP 28, US), that is mechanically uncoupled from the chamber by a heavy attenuator. Higher vacuum is obtained with a turbo pump (VARIANT TV70D, Italy) with magnetic bearings mounted directly upon the vacuum chamber. Significantly low

pressure levels (below 10^{-6} mbar) are not required for the characterization of the devices, since it has been demonstrated (on cantilevers, but the same considerations can be extended to pillar-based systems) that, below 10^{-3} mbar of pressure, the effect of pressure on resonant frequency shift and Q-factor is negligible[15].

All the samples are mechanically characterized using the optical lever technique described in[16,17] and the measurement setup is schematized in Figure 2.6. The "actuator and sample" block (7) can be either the vacuum chamber or the piezoelectric actuator plus sample in air.

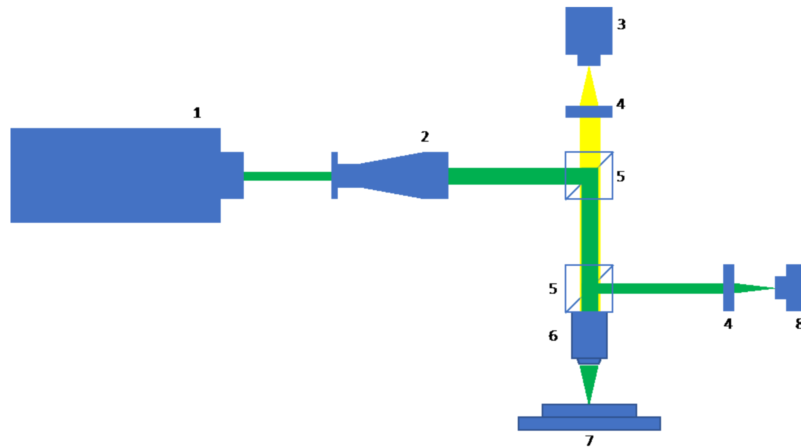

Figure 2.12 - Optical lever setup. 1: laser source, 2: 10x beam splitter, 3: white light illuminator, 4: lens, 5: beam splitter, 6: microscope objective, 7: actuator and sample, 8: photodiode

A lock-in amplifier (7280 DPS, Ametek Advanced Measurement Technology, Inc.) is used to elaborate the signal coming from the photodiode and, in the case of vacuum measurements, drive the piezoelectric actuator; the laser source is a 532 nm DPSS laser. When the laser is shone on the top of the non-actuated pillar the signal coming from the reflected beam to the photodiode is measured with an oscilloscope and used to align the photodiode to get a value as close to zero voltage as possible, in order to achieve the maximum sensitivity to pillar motion. The piezo is driven by a sinusoidal voltage through the internal oscillator of the lock-in amplifier, which is also used as the reference signal for the measurement; this is phase-shifted and multiplied by the measured signal coming from the photodiode to allow the rejection of all signals but those at the actuation frequencies. A phase-sensitive detector allows the separation of the input components depending on their frequency, and a low-pass filter removes all those which are not synchronized with the reference. The parameters for the lock-in signal processing are sensitivity, time constant, AC gain and selected harmonic component. The sensitivity and the AC gain are strictly related: the better the required sensitivity for the application is, the lower the allowed AC gain would be. Since the AC gain is simply the gain of the amplifier for the input signal, it would also amplify the noise associated with the input and therefore the lock-in amplifier (at least the digital, most recent ones) can limit

the gain to avoid the overloading of the input channel. The frequency-related behaviour of the lock-in amplifier is also evidenced in the presence of a low-pass filter which rejects the components with frequencies different from the reference; the time constant parameter mentioned before is the time constant of this filter, which can be specified in most recent instruments, while its quality (*i.e.* the steepness at which the filter reaches the maximum attenuation) is intrinsic. Finally, it is worth mentioning that a lock-in amplifier, and more efficiently so the digital ones, can choose to detect the signal coming at higher harmonics of the reference signal: this process, which requires only the selection of the desired harmonic, will cause the reference signal to be multiplied by the harmonic selected before the multiplication with the input, and allows the investigation of nonlinear phenomena such as plasmonics or electron spectroscopy[18].

The frequency of the actuation is scanned in sweeps of decreasing range and step size, thus allowing for the detection of the resonant frequency of the pillar within a small degree of uncertainty. The frequency sweeps are repeated at varying actuation voltages to analyse the behaviour of the resonators.

The same technique is used to characterize the pillar device outside the vacuum chamber (*i.e.* in air), with the only modification regarding the drive voltage source of the piezoelectric actuator. Due to the presence of air damping, the piezo requires higher voltages to actuate the pillars and therefore is driven by an arbitrary function generator.

2.4.3.2 Mechanical characterization of the cantilever device

The characterization of the cantilever device has been performed directly on the setup that would be used afterwards for the Raman measurements. The measurement setup is depicted in Figure 2.13. The optical technique used for the characterization is different from the optical lever described earlier. The laser (Laser Quantum Torus, 140 mW, 660 nm, 1 MHz bandwidth, vertical polarization) is focused on top of the device and then directed to a point near the edge of the steady wall; the actuated cantilever, when approaching and leaving resonance mode, increases the amplitude of its motion until the tip reaches the laser spot and the signal coming from the reflected laser light is increased.

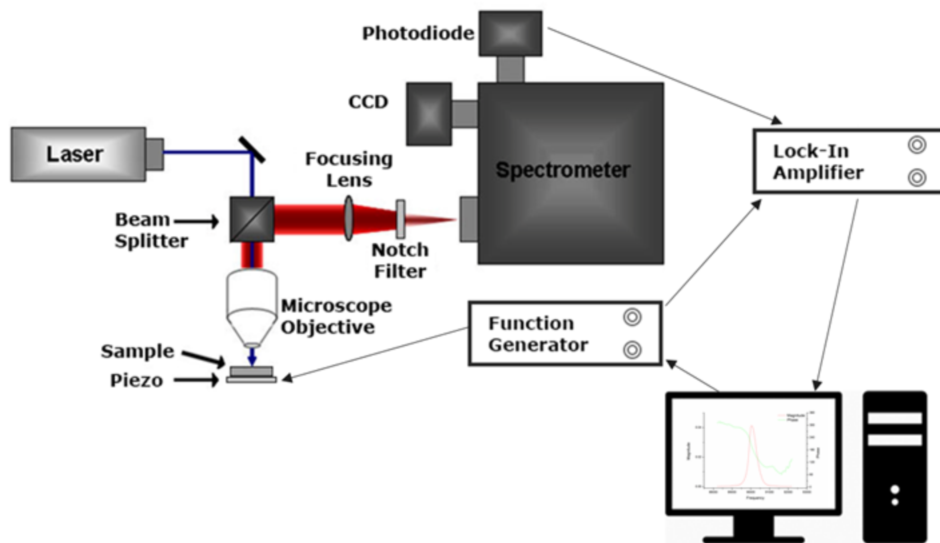

Figure 2.13 - Raman spectroscopy setup, also used for the mechanical characterization of the cantilever device. Without the notch filter, the spectrometer can act as a monochromator to acquire the Rayleigh scattered light.

The measurements are performed in air, so the actuator is driven by a function generator which can provide a higher drive voltage than the internal oscillator of the lock-in amplifier. The function generator is controlled via homemade LabVIEW software to sweep the frequency at the maximum actuation voltage; a TTL signal generated in phase with the sinusoidal drive voltage is used as reference for the lock-in amplifier elaboration already explained in § 2.4.3.1. The maximum of the signal in the frequency sweep curve corresponds to the maximum deflection amplitude, *i.e.* resonance condition. Once identified, the resonant frequency is set and the drive voltage is varied to understand the oscillator behaviour; the graph for the amplitude sweep should reach a maximum value or a plateau for the minimum voltage required to achieve contact conditions.

The lock-in amplifier can also be replaced with a gated photon counter, which is used in the tracking of the time-resolved behaviour of the cantilever tip during actuation. The signal from the avalanche photodiode (APD) is made of pulses, each corresponding to an event of a photon hitting the photodiode, that can be counted by the photon counter; the number of photons is proportional to the reflected light, so the number of counts is a measure of the portion of the tip illuminated by the laser. If the laser spot is fixed to the same position described earlier and the actuation parameters set at the resonant frequency and contact voltage, the gate delay can be swept along the period of the cantilever oscillation to collect the signal at different instants using a very short gate width, *i.e.* counting the photons only in very short time intervals along the whole period. The complete sweep of the gate delay from the beginning to the end of the oscillation period allows the tracing of the tip approach to the steady structure.

2.4.3.3 Rayleigh and Raman measurements

The functionality of the devices is demonstrated through the increase in the Raman scattering signal from the molecule chosen for the functionalization; the setup for the Raman scattering measurements is described in § 2.4.3.3, Figure 2.13, while the principle of the Raman spectroscopy has been already explained in § 1.1.

The Rayleigh and Raman scattering measurements are performed on an inverted optical microscope (Axiovert 200, Zeiss) coupled with a 750-mm long spectrometer (Shamrock SR-750, Andor Technology plc). First, a sample is mounted on the XY sample holder in order to obtain the laser scanning confocal images. 532 nm (Cobolt Samba, 50 mW, bandwidth 1 MHz) or 660 nm (Laser Quantum Torus, 140 mW, bandwidth 1 MHz) CW laser is used as the source of monochromatic light. The laser beam is reflected by a beam splitter, directed to the microscope and then focused on the sample by a 100x air objective (NA 0.8, EC Epiplan, Zeiss) resulting in a radius of the laser spot on the sample of around 0.4 µm. The approximated size of the beam spot is calculated using Equation 2.2.

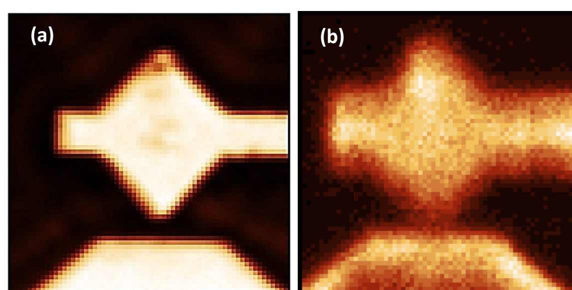

Figure 2.14 - Mapping of the cantilever device in the region of interest obtained using reflected (Rayleigh scattered) (a) and Raman scattered (b) light.

The Rayleigh or Raman scattered light is collected by the same objective and directed into a spectrometer through the proper edge filter (664 nm RazorEdge® or 532 nm RazorEdge® ultrasteep long-pass edge filter, for Raman mode only), dispersed by a diffractive grating of 600 lines/mm, and finally analysed using either a TE-cooled EMCCD (Newton DU971-UVB, Andor Technology plc) to acquire the spectra or a silicon avalanche photodiode (SPCM-AQRH-15, Perkin Elmer) connected to a lock-in amplifier. The position of the diffractive grating can be controlled by the Andor SOLIS software and changed accordingly to the Rayleigh or Raman mode. The XY sample holder allows to move the sample with nanometric precision, focusing on the locations of interest. The laser power on the sample is controlled by a variable metallic neutral density filter (NDC-50C-4M, Thorlabs) and kept at 0.01 mW or 0.1 mW for Rayleigh or Raman mode respectively. The signal from the APD is elaborated by the lock-in amplifier (when appropriate), as described earlier in § 2.4.3.1, and transferred to the controller of the atomic force microscope (Nanowizard II, JPK), which controls

the XY piezo stage (TAO module, JPK) and allows to scan a sample in the range of 100x100 µm for the recording of laser scanning confocal images with reflected (a) or Raman scattered (b) light.

References

(1) Franssila, S. *Introduction to Microfabrication*, 1st ed.; John Wiley & Sons, Ltd: Chichester, UK, 2004; Vol. 1.

(2) Samsung. Samsung Starts Industry's First Mass Production of System-on-Chip with 10-Nanometer FinFET Technology https://news.samsung.com/global/samsung-starts-industrys-first-mass-production-of-system-on-chip-with-10-nanometer-finfet-technology.

(3) Vieu, C.; Carcenac, F.; Pepin, A.; Chen, Y.; Mejias, M.; Lebib, A.; Manin-Ferlazzo, L.; Couraud, L.; Launois, H. Electron Beam Lithography - Resolution Limits and Applications. *Appl. Surf. Sci.* **2000**, *164*, 111–117.

(4) Robbie, K.; Brett, M. J. Sculptured Thin Films and Glancing Angle Deposition: Growth Mechanics and Applications. *J. Vac. Sci. Technol. A Vacuum, Surfaces, Film.* **1997**, *15* (3), 1460–1465.

(5) Earl, J. S.; Leary, R. K.; Perrin, J. S.; Brydson, R.; Harrington, J. P.; Markowitz, K.; Milne, S. J. Characterization of Dentine Structure in Three Dimensions Using FIB-SEM. *J. Microsc.* **2010**, *240* (1), 1–5.

(6) Lobontiu, N. *Dynamics of Microelectromechanical Systems*; Microsystems; Springer US: Boston, MA, 2007; Vol. 17.

(7) Roark, R. J.; Young, W. C.; Plunkett, R.; Budynas, R. G. *Roark's Formulas for Stress and Strain*, 7th ed.; 2002; Vol. 43.

(8) Ilic, B.; Krylov, S.; Aubin, K.; Reichenbach, R.; Craighead, H. G. Optical Excitation of Nanoelectromechanical Oscillators. *Appl. Phys. Lett.* **2005**, *86* (19), 1–3.

(9) Labuda, A.; Cleveland, J.; Geisse, N.; Kocun, M.; Ohler, B.; Proksch, R.; Viani, M.; Walters, D. Photothermal Excitation for Improved Cantilever Drive Performance in Tapping Mode Atomic Force Microscopy. *Microsc. Anal.* **2014**, *28* (3), 23–27.

(10) Fitzpatrick, R. Resonance in one-dimentional oscillators http://farside.ph.utexas.edu/teaching/336k/Newtonhtml/node21.html (accessed Sep 16, 2017).

(11) Naumenko, D.; Toffoli, V.; Greco, S.; Dal Zilio, S.; Bek, A.; Lazzarino, M. A Micromechanical Switchable Hot Spot for SERS Applications. *Appl. Phys. Lett.* **2016**, *109* (13), 131108.

(12) Siegfried, T.; Ekinci, Y.; Martin, O. J. F.; Sigg, H. Engineering Metal Adhesion Layers That Do Not Deteriorate Plasmon Resonances. *ACS Nano* **2013**, *7* (3), 2751–2757.

(13) Naumenko, D.; Toffoli, V.; Greco, S.; Dal Zilio, S.; Bek, A.; Lazzarino, M. A Micromechanical Switchable Hot Spot for SERS Applications (Supplementary Information). *Appl. Phys. Lett.*

2016, *109* (13), 3–5.

(14) Naumenko, D.; Stolzer, L.; Quick, A. S.; Abt, D.; Wegener, M.; Barner-Kowollik, C.; Zilio, S. D.; Marmiroli, B.; Amenitsch, H.; Fruk, L.; Lazzarino, M.; Dal Zilio, S.; Marmiroli, B.; Amenitsch, H.; Fruk, L.; Lazzarino, M.; Zilio, S. D.; Marmiroli, B.; Amenitsch, H.; Fruk, L.; Lazzarino, M. Design of Broadband SERS Substrates by the Laser-Induced Aggregation of Gold Nanoparticles (SI). *J. Mater. Chem. C* **2016**, *4* (25), 6152–6159.

(15) Yasumura, K. Y.; Stowe, T. D.; Chow, E. M.; Pfafman, T.; Kenny, T. W.; Stipe, B. C.; Rugar, D. Quality Factors in Micron- and Submicron-Thick Cantilevers. *J. Microelectromechanical Syst.* **2000**, *9* (1), 117–125.

(16) Melli, M.; Pozzato, A.; Lazzarino, M. Inverted Tapered Pillars for Mass Sensing. *Microelectron. Eng.* **2010**, *87* (5–8), 730–733.

(17) Melli, M.; Scoles, G.; Lazzarino, M.; Al, M. E. T. Fast Detection of Biomolecules in Diffusion-Limited Regime Using Micromechanical Pillars. *ACS Nano* **2011**, *5* (10), 7928–7935.

(18) Stanford Research Systems. Model SR830 User Manual. 2011.

3 A micromechanical switchable hot spot for SERS applications

In this chapter, the results of the different stages of the device realization are explained for the pillar device, from the fabrication to the Raman enhancement effect validation. The problems arisen, and the actions taken to solve them are also presented.

3.1 Fabrication of the device

The fabrication of the pillar devices has been carried out using methods and instrumentations already described in § 2.4.1; the Bosch-like process used for the ICP-RIE dry etching has been carefully tuned to obtain the inverted tapered structure of the resonator, a conformation that ensures larger oscillation amplitudes. The main issue regarding the fabrication of the pillar devices arises during the lift-off process, due to the very short separation gap between the pillar and the steady structure. Imperfect removal of the PMMA resist layer during lift-off of the metal mask can cause unwanted coverage of the gap (Figure 3.1), resulting in the incomplete detaching of the pillar.

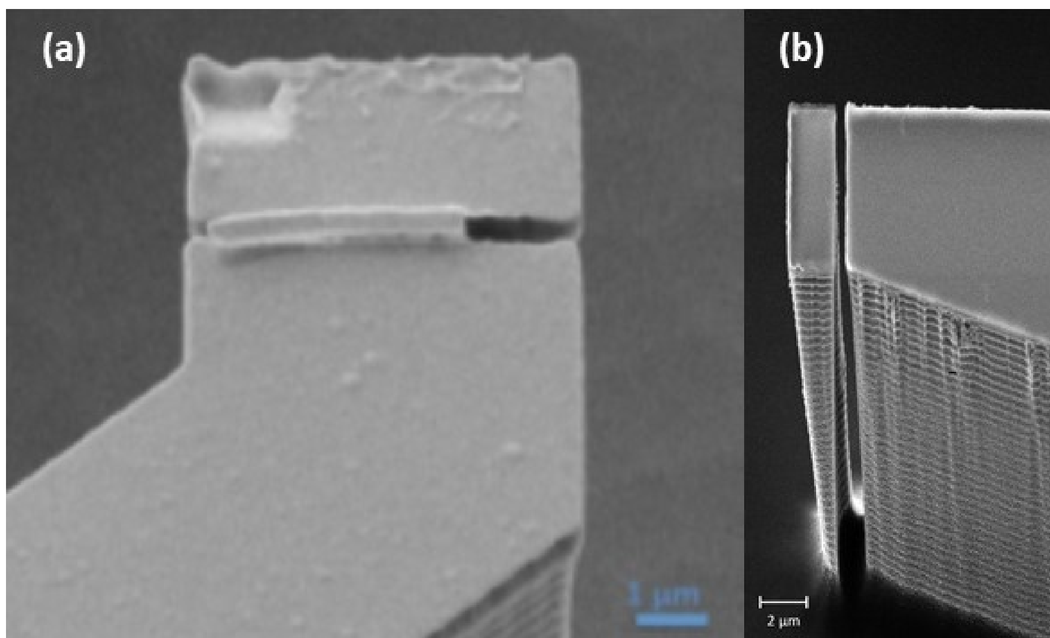

Figure 3.1 – (a) Artefact during fabrication of the pillar device: the gap between the pillar (top) and the steady structure (bottom) is not completely opened during lift-off, resulting in an unwanted bridging between the two structures. Scale bar is 1 μm. (b) Side iew of a complete pillar device; the inverted tapering on the back wall of the pillar is evident. Scale bar is 2 μm.

The Bosch process for the ICP-RIE etching of the pillars has an influence over the mechanical parameters of the pillars. The ICP etching process developed in our laboratory allowed us to fabricate the pillar with an inverted tapered structure (Figure 3.1 (b)), whose resonant frequency is dependent from the thickness of the top and of the base. Sometimes, however, the tapering can be unevenly distributed on the whole sample, due to thickness inhomogeneity of the substrate or fabrication defects, and some of the pillars can be destroyed by an excessive etching of the base. As already explained in § 2.3.2, the resonant frequency of a standard cantilever structure can be calculated, for the first flexural eigenmode, using Equation 2.3; when evaluating cantilevers with a tapered structure, however, the influence of the shape must be considered to have a better esteem of this parameter. With the peculiar shape of the pillars, most of the mechanical stress during motion is concentrated at the base, thus allowing for a simplification of the analytical modelling of the tapered pillars: the effective thickness can be approximated with the thickness at the base, introducing an overestimation but getting closer to the real resonant frequency trend. The etching process used to fabricate this kind of structures, following our results already reported in literature[1], introduced in the structure a constant underetching angle of about 3°. The final dimensions of a half-tapered pillar are 2x5 µm on the top, 0.95x2.9 µm at the base, 15 µm height, and a gap width of 100 nm.

After the fabrication of the complete device, a thin film of chromium and gold with thickness of 2 nm and 40 nm respectively has been deposited following the protocols described in § 2.4.1; the obtained metallic layer covers the top of the devices and the first part of the side wall, to ensure a more uniform attachment of functional molecules around the edges. Using the same tilted evaporation technique used for the metallic layers, a thin film of pentacene has been evaporated on the device. The final pentacene thickness during the 4-positions scan is 2 nm per azimuthal angle, resulting in a final pentacene thickness on top of the devices of 1.5 nm.

3.2 Mechanical characterization

3.2.1 Preliminary calculations and finite element analysis

The behaviour of the resonator has been estimated before characterizing the device to select the best operating conditions and instruments for the experiments; specifically, the resonant frequency has been estimated with the use of both analytical equations and finite-element modelling. In this device, the etching-induced tapering is localized only on the sides of the pillar not facing the wall, while the side facing the wall is perpendicular to the substrate, making it a half-tapered structure;

to account for this half-tapering, the formula used for the estimation of the resonant frequency must be modified accordingly. The result of the modification of Equation 2.3 is the following:

$$f = \frac{3.52}{2\pi} \cdot \sqrt{\frac{E}{\rho}} \cdot \frac{(t_0 - l \tan \alpha)}{l^2} \tag{3.1}$$

Where the numerator of the second fraction is the thickness at the base of the pillar, in which t_0 is the thickness at the top of the pillar, l is the height of the pillar and α the under-etching angle. The corrected esteem of Equation 3.1 can be compared with the behaviour of an analogue FEM system:

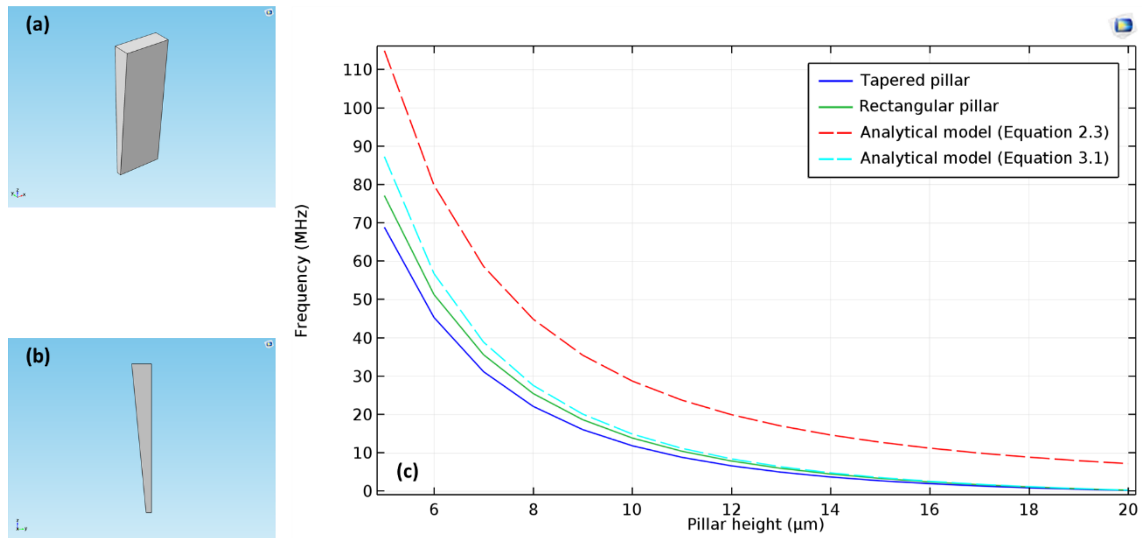

Figure 3.2 - Analytical and finite-element modelling of the resonant frequency for a micropillar resonator. The half-tapered geometry used in the FEM simulation is shown in (a) and (b – side view), while the rectangular is not shown. (c) Resonant frequency as a function of the pillar height for the half-tapered pillar (blue), rectangular pillar (green), and the two analytical models: Equation 2.3 (red, dashed) and Equation 3.1 (cyan, dashed).

The results have shown the aforementioned overestimation of the effective resonant frequency, which is fairly predictable if we consider that Equation 3.1 is simply the modification of Equation 2.3 considering the base of the tapered pillar. Comparing the results of the analytical models and the FEM simulations, the contribution from the mass of the pillar which is neglected when approximating the half-tapered structure to a rectangular one, which leads to an overestimation of the resonant frequency of the system.

3.2.2 Mechanical characterization in vacuum

As already described in § 2.4.3.1, the pillar device has been mechanically characterized first in vacuum, and only later in air. The vacuum characterization gives important information about the frequency response and amplitude-dependent behaviour of the pillar.

During the search for the resonance conditions, the actuation frequency is swept sequentially in decreasing spans centred around the calculated resonant frequency. After the determination of the resonant frequency, the frequency is swept at different actuation voltages to understand the behaviour under varying intensities of the driving force.

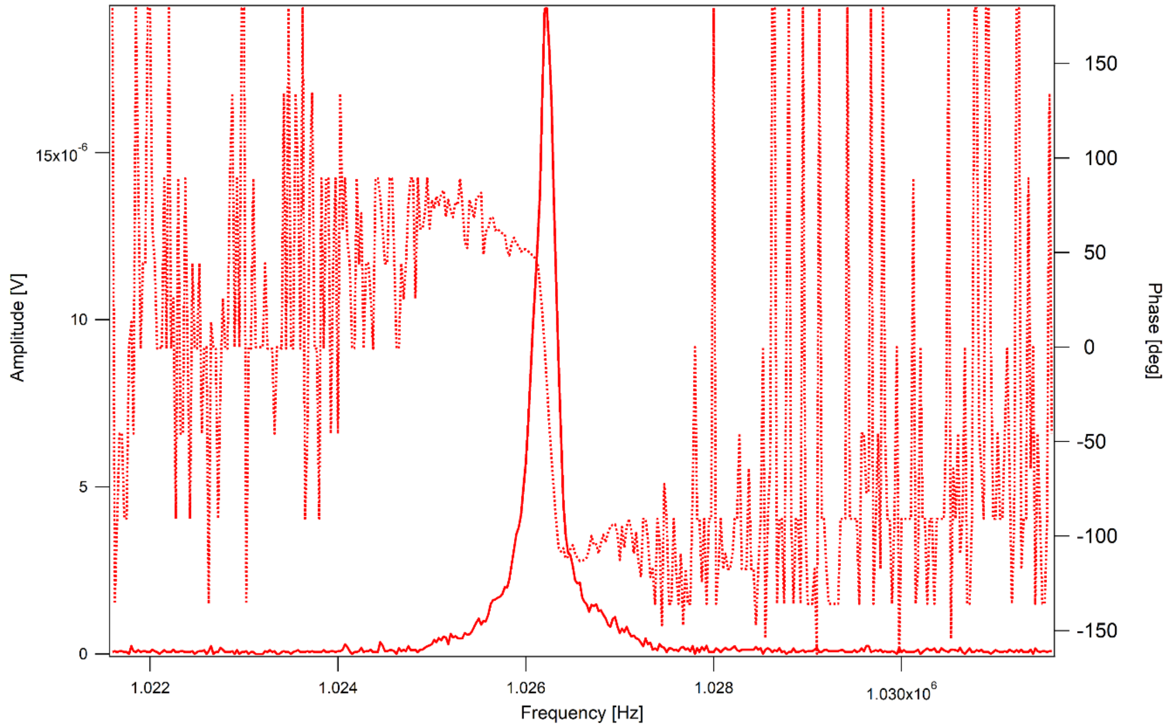

Figure 3.3 - Frequency response (positive scan) of a pillar device. The amplitude shows a peak corresponding to the resonant frequency, while the phase has a linear behaviour in the same region, with the flex point corresponding to the exact value of the resonant frequency.

The frequency sweeps during the characterization have been performed from lower to higher frequency (positive scans); for low actuation voltages, the measured pillars have shown a distinctive resonance behaviour. The resonant frequency is slightly different for each pillar due to tolerance in the substrate uniformity and in the fabrication procedures, thus requiring a separate characterization for each device. The quality factor Q for these devices, defined as the ratio between the resonant frequency and the Full Width Half Maximum (FWHM), in vacuum has been calculated to be on average 3800.

With increasing actuation voltage, the graph changes its shape: the oscillation amplitude increases with voltage, but it reaches a saturation value, due to the fact that the pillar oscillation is limited by the presence of the adjacent steady structure.

On the other hand, the width of the resonance increases with the actuation voltage, maintaining high oscillation amplitude also off resonance, to suddenly drop to zero at higher frequency. This resemble the Duffing oscillator behaviour[2,3] which for mechanical oscillator is due to a hardening effect at high oscillation amplitudes. Here the hardening is instead induced by the impact of the

pillar against the steady wall, impact that result harder at higher voltage amplitude. Figure 3.4 (a). To verify this hypothesis, we scanned the actuation voltage downward, from higher to lower values. In this case the hardening effect is not observed, as expected. Above a certain voltage the amplitude remains practically constant, and the resonance peak shows the same shape.

The observed frequency response can be described in an impact oscillator-like framework[4]. During contact time, the system behaves chaotically, and the pillar motion can be described by a superposition of mode in which sub-harmonic frequencies are introduced. The mechanical contact causes a shift of resonant frequency to higher and, with the increase of the actuation voltage, the plateau increases its frequency extension. The system in this condition is bistable and, when the resonant condition cannot be sustained further, frequency response comes back to its original value and the response of device drastically drops down. Scans with negative frequency shows a two-peak response in the amplitude response (Figure 3.4 (b)). When contact occurs, pillar amplitude response drops down immediately, due to the shift of the resonant frequency; this causes a decrease on oscillation amplitude down to no-contact condition. Consequently, the pillar immediately arises out of its chaotic oscillation state and this results in a narrow amplitude negative peak at the resonant frequency.

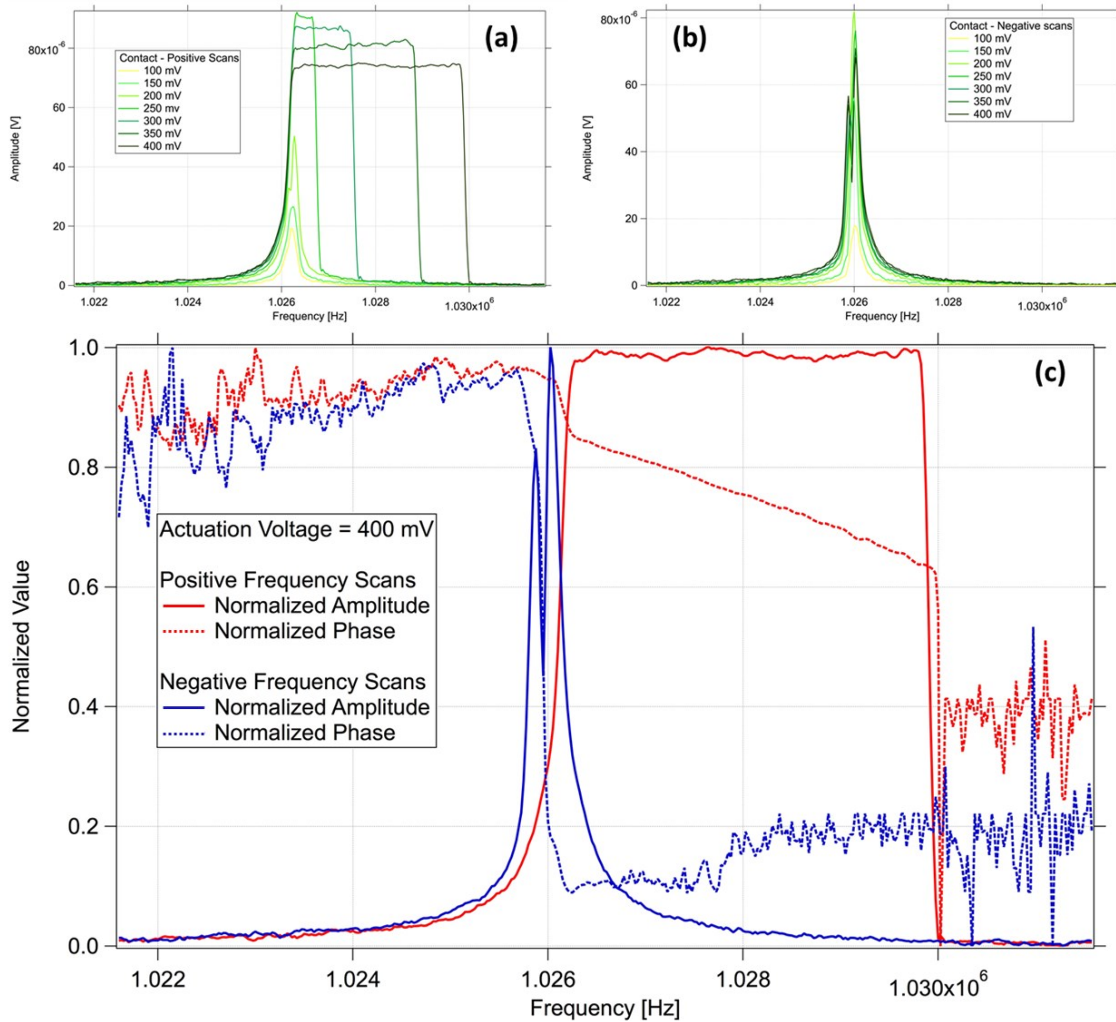

Figure 3.4 - Actuation of the pillar device with varying actuation voltage: increasing (a) and decreasing (b) frequency sweeps. The effect of the impact is visible in both graphs, either as an amplitude-limited response during contact in (a) or a double-peak behaviour of the resonator in (b). Positive and negative scan results are normalized and compared in (c) along with the phase behaviour of the pillar device during contact characterization.

The impact oscillator behaviour of the pillar device implies an even more pronounced stiffening effect for higher actuation voltages; although the motion in an impact oscillator is chaotic, we can infer from the graph that, by increasing the actuation strength, the fraction of the oscillation period in which the pillar is in contact with the rigid wall increases due to the spatial constraints of the device design. It is worth observing also the detected phase in the impact oscillator-like behaviour of the device: both during positive and negative frequency scans, the phase changes linearly during contact. This is compatible with the resonant frequency shift caused by the hardening effect of the impact oscillator, where the phase change during resonance is not ideally instantaneous any more. The induced instability causes a rapid change in the phase response of the pillar and then, due to the spatial limitations of the resonance, it decreases at a linearly slow rate instead of an asymptotically fast one.

3.2.3 Mechanical characterization in air

The same characterization has been performed in air, confirming the results already obtained with the in-vacuum characterization. To oscillate in air, the pillar requires a much higher actuation voltage, due to the increased energy dissipation produced by the increased friction and the film squeezing effect: the air trapped in the narrow gap between the pillar and the wall acts as an obstacle to the oscillation at low voltages. As a first consequence the quality factor of the resonance is reduced, typically the reduction in the quality factor can be up to two orders of magnitude[5]. A second effect due to the increased dissipation is a significant red shift of the resonance frequency.

3.2.4 Metallic layer characterization

The uniformity of the metallic film above the devices has been analysed mapping the top surface of pillars and associated steady structures; the maps have been acquired using the setup and method already presented in § 2.4.3.3. This method allows the collection of the light from different points, which is then filtered using a spectrograph set at the laser wavelength, and its intensity measured with an avalanche photodiode.

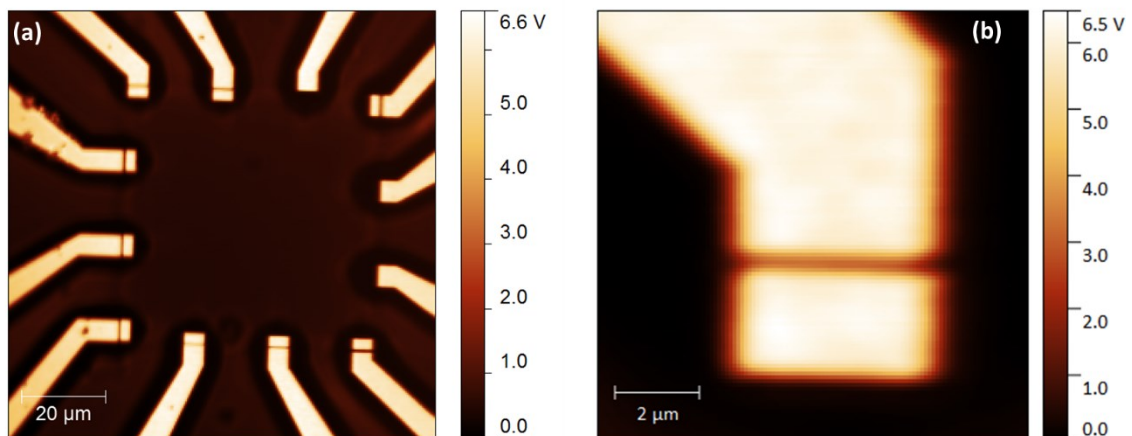

Figure 3.5 - (a) 80x80 μm reflectivity map of a complete device. The two missing pillars on the right side are lost in the etching step of the fabrication. (b) 10x10 μm map of a single pillar (top row in (a), left side) with the steady structure. The inhomogeneity of the gold layer are barely visible, demonstrating the smoothness of the metal surface.

The reflectivity maps show that the gold coverage of silicon is complete, and show uniform reflectivity over the whole surface, considering the averaging effect of the optical mapping and the diffraction limit of resolution; the same effects cause the blurring of the across the gap between the pillar and the wall. In the perspective of Raman scattering experiments, a uniform reflectivity

can help avoiding substrate-induced inhomogeneity in the distribution of the Raman signal. Profile analysis of the maps in three different positions have confirmed this estimate (Figure 3.6).

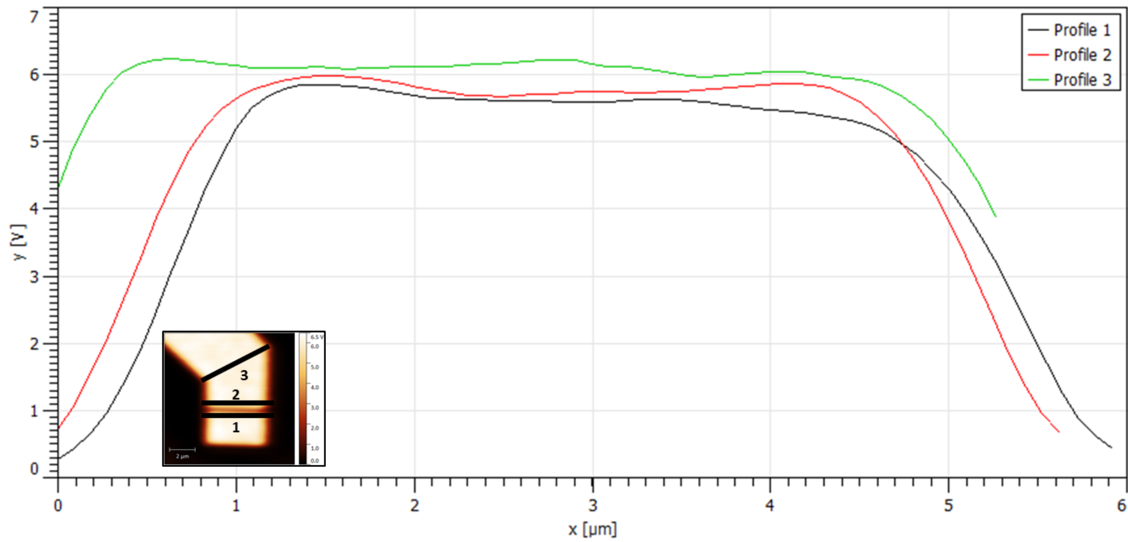

Figure 3.6 - Quantitative analysis of the gold layer reflectivity in three positions: (1) along the gap on the pillar, (2) along the gap on the steady structure, (3) at the bending of the steady structure. The two profiles across the gap start from points out of the structure, while the third profile rests completely on the gold film.

The obtained uniformity of the gold layer along the gap-facing edges is important because a non-uniform film in the region where the hot spots will be created could cause an uneven distribution of the enhancement along the contact area, thus reducing the overall increase in the electromagnetic field.

3.3 SERS effect detection

After the assessment of the gold layer uniformity, the presence of pentacene has been verified on different points along the top surface of the device. The Raman spectrum has been collected from the top of the steady structure, from the top of the pillar far from the gap and from different points along the gap, which is small enough to allow the detection of the Raman signal from both edges of the device.

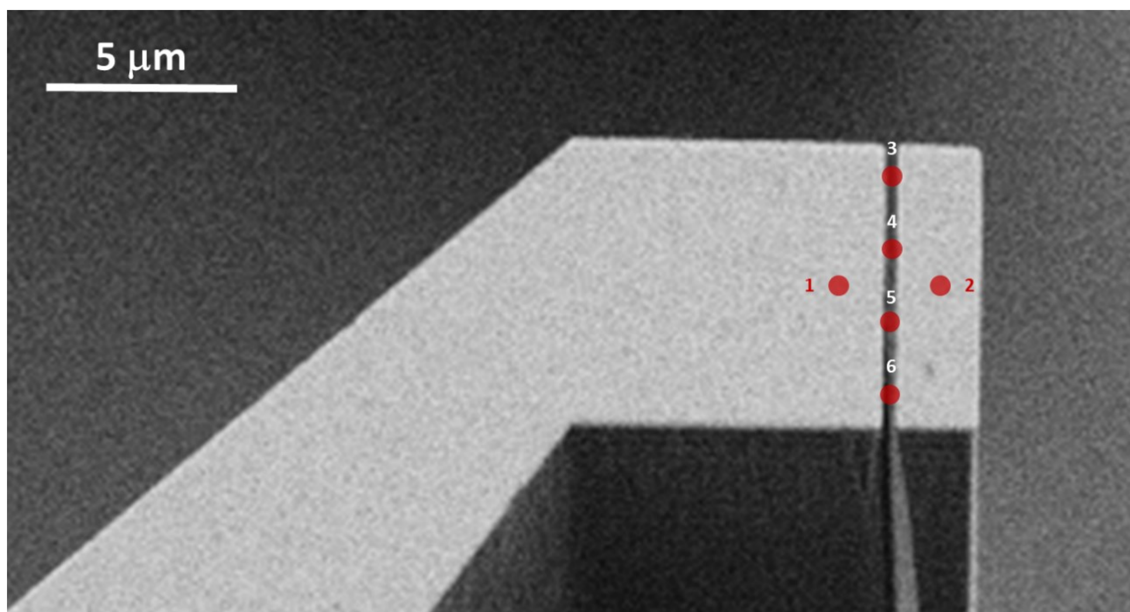

Figure 3.7 - Raman spectrum collection points. 1: steady structure; 2: pillar (far from the gap); 3: gap (edge 1); 4: gap (middle 1); 5: gap (middle 2); 6: gap (edge 2).

The choice of pentacene for this kind of experiments has been done for two main reasons:

- To exploit the resonance effect, since thin films of pentacene have a strong absorption peak towards the red end of the visible spectrum;
- To have a morphology-independent deposition on the surface, due to the applicability of functionalization via grazing evaporation (see § 2.1.2) to pentacene;
- To have a good control of the pentacene thickness.

The appropriate excitation wavelength has been chosen with a simple experiment: pentacene has been evaporated on two glass slides with different thickness and the absorbance has been measured in a broad wavelength range. The results obtained confirm the resonant condition and demonstrate that the absorption spectrum of pentacene is, for the purpose of these experiments, thickness-independent.

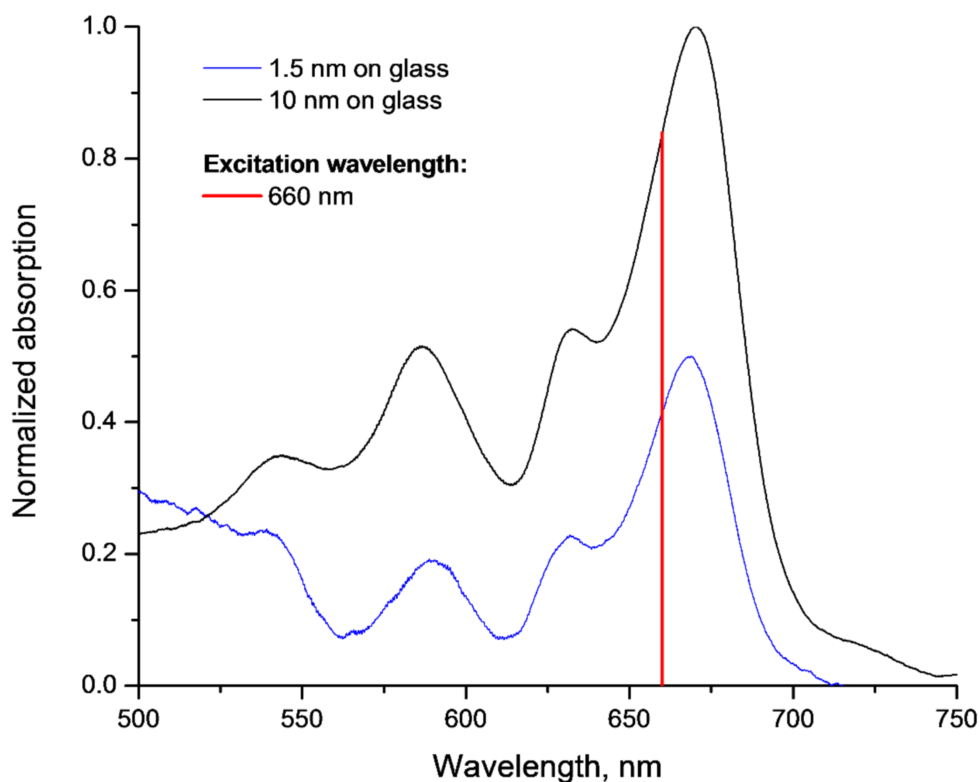

Figure 3.8 - Absorption spectra of pentacene on glass evaporated at two thicknesses: 1.5 nm (blue curve) and 10 nm (black curve).

The measured Raman spectrum matches well with the spectrum of pentacene found in literature[6] (Figure 3.9 (a)) and its intensity is comparable when acquired in different positions far from the gap; the main spectral features of the aromatic rings around 1160 and 1180 cm^{-1} are well represented along with the peak at 1370 cm^{-1}, and the small contribution at 1530 cm^{-1} can be attributed to the polycyclic structure of the pentacene molecule. The spectra from the positions along the gap are compared with those acquired far from the gap and the intensity is reduced as expected, since the gap is wide enough to subtract a large portion of the pentacene molecules from the laser spot. The device has been actuated at the resonant frequency and the spectra on the top of the pillar, as in position 2 from Figure 3.7, have been recorded during dynamic mode (*i.e.* when the pillar is actuated) and compared with the previous measurements in the same regions, with no noticeable differences (Figure 3.9 (b, c)). This spectrum will be used in further measurements as reference for the pentacene.

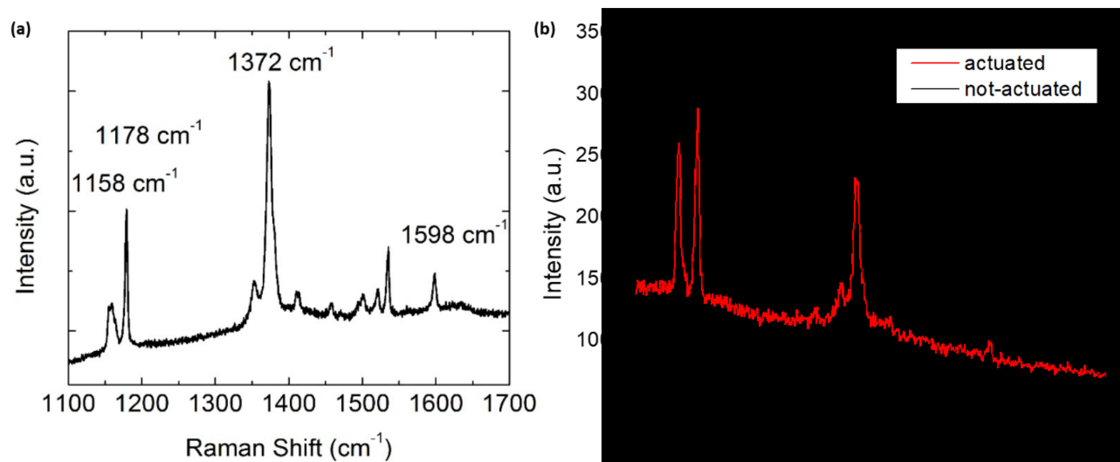

Figure 3.9 - (a) Raman spectrum of a 30 nm-thick layer of pentacene on quartz recorded with 532 nm excitation wavelength. Reproduced from literature[7]. (b) Raman spectrum of pentacene measured on the flat surface of an actuated (red) and not-actuated (black) pillar. The peaks with the highest intensity are labeled for each graph, and the three highest peaks show the same spectral position. The difference in the relative intensity between literature and measured spectrum is due to the different excitation wavelength: (a) is non resonant, (b) is resonant.

After the characterization of the pentacene layer, the measurements to assess the presence of the hot spot have been performed. Raman spectra have been collected in the four positions along the gap depicted in Figure 3.7 during static and dynamic mode. As already mentioned earlier, the laser used in the experiments is vertically polarized, and the polarization direction on the sample, after the optical path, has been detected using a rotating linear polarizer (λ/2). The pillars for these measurements have been chosen with the gap oriented perpendicularly to the laser polarization, in order to maximize the hot spot formation probability, and actuated at the maximum voltage allowed by the available instrumentation (10 V_{pp}).

The results of the hot spot formation assessment are presented in Figure 3.10:

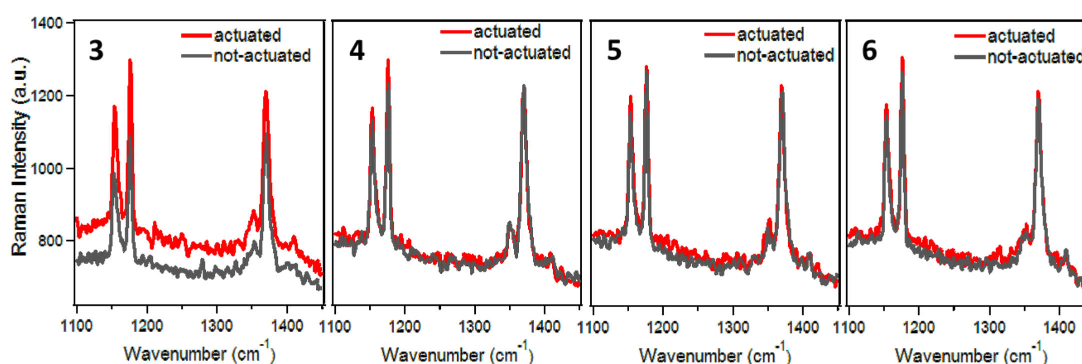

Figure 3.10 - Raman spectra for actuated (red) and not-actuated (black) pillars with the gap oriented perpendicularly to the polarization direction. The collection points 3,4,5,6 are the same depicted in Figure 3.7.

At the position "3" a significant enhancement can be observed. The origin of this increased signal can be safely deemed independent from the increased number of molecules under the laser spot during pillar actuation, since this effect should be observable everywhere: the pillar motion has

been observed through a CCD camera during the mechanical characterization in air and the oscillation of the pillar top surface has been found to be coherent with the first resonance oscillation mode, as predicted by the simulations in § 3.2.1.

3.3.1 *Effects of the laser polarization*

Since the hot spot formation is a plasmonic phenomenon, the dependence from the polarization direction of the incident light must be considered to prove the plasmonic nature of the enhancement. Therefore, on each sample, other pillars with the appropriate Q factor have been chosen, with the gap parallel to the light polarization. While the enhancement has been measured on the pillars with the previous configuration, no effect should be observed in these ones.

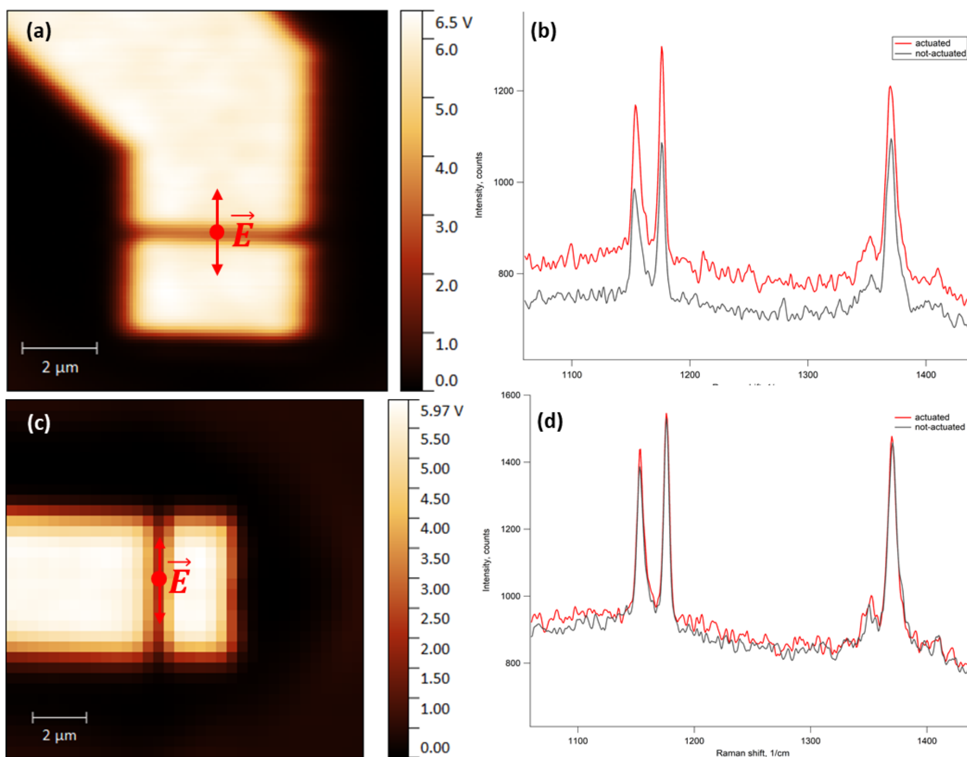

Figure 3.11 - (a) Reflectivity map of the pillar with the gap perpendicular to the polarization. (b) Actuated (red curve) and not-actuated (black curve) Raman spectrum of pentacene in the enhanced collection point (Figure 3.10 (3)) with perpendicular polarization. (c) Reflectivity map of the pillar with the gap parallel to the polarization. (d) Averaged actuated (red curve) and not-actuated (black curve) Raman spectrum of pentacene in all the collection points with parallel polarization. The collection points are those along the gap, as depicted in Figure 3.7, the polarization direction is shown in (a,c).

The pillars in Figure 3.11 (a,c) were chosen for the good quality of the resonance, each of them being oriented correctly to allow perpendicular and parallel polarization measurements. The Raman signal collected along the gap of the pillar parallel to the polarization direction hasn't been enhanced (only the averaged spectrum in Figure 3.11 (d) showed because all the spectra are the

same within the experimental error limit), thus demonstrating the plasmonic nature of the enhancement.

3.3.2 *Modulability of the enhancement*

The rationale behind the device, as already mentioned earlier, is the ability to switch on and off the enhancement effect for the Raman signal; however, due to the ability to change the voltage and frequency of the actuation, it may be possible to modulate the signal enhancement changing one parameter or the other.

The absolute value of the Raman peaks of pentacene increases with increasing actuation voltage, as expected from the increased contact time underlined in § 3.2.2: the longer the contact is maintained, the higher the duration of the plasmonic phenomena which can cause the signal enhancement, since they are distance-dependent.

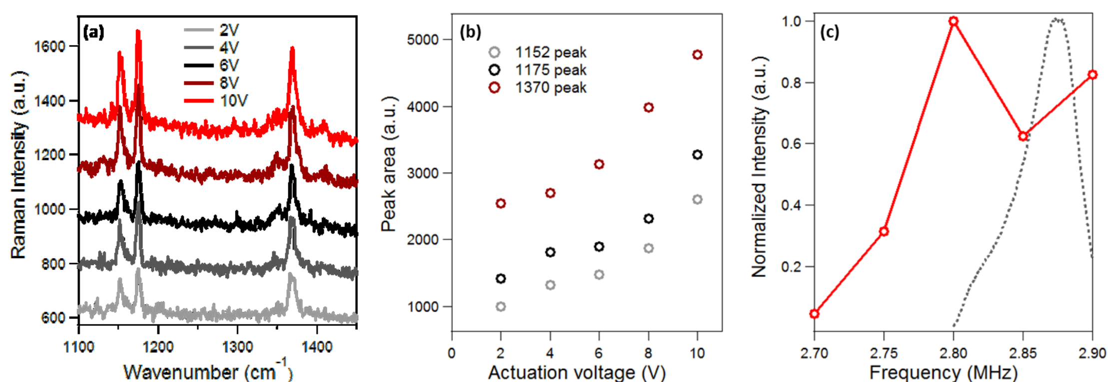

Figure 3.12 - (a) Raman spectra collected at point 3 for different actuation voltages (vertically shifted for better visualization). (b) Integration of the area under the three main Raman peaks of pentacene for increasing actuation voltage. (c) Red line: frequency response of the sum of the areas underneath the three main Raman peaks, normalized to [0:1]; black dotted line: frequency response of the pillar, measured in air with low actuation voltage before the deposition of pentacene, normalized to [0:1].

The increase in the area underneath each of the three main Raman peaks of pentacene plotted against the actuation voltage shows a linear dependence from the actuation voltage (Figure 3.12 (b)).

Changing the actuation frequency means detuning the pillar from its resonance; the resulting effect should be similar to the change in the actuation voltage, since the oscillation amplitude rapidly decreases when moving from the resonant frequency to higher or lower values. In Figure 3.12 (c) this phenomenon is evident, thus demonstrating the opportunity to modulate the enhancement changing either the actuation frequency or the voltage. The shift towards lower frequency of the resonance peak from the mechanical characterization (black dotted line) to the Raman intensity measurements (red line) is due to the additional mass of pentacene, evaporated after the mechanical characterization of the devices. The mass of the evaporated pentacene cannot be

estimated from these measurements because the mass sensitivity of the pillars has not been evaluated and the resolution of the curve for the Raman measurements is not enough to have a precise value of the resonant frequency.

3.3.3 *Signal enhancement evaluation*

The enhanced factor for the Raman signal at point 3 of Figure 3.7 has been calculated: the ratio between the Raman signal area under the three peaks (1152, 1175, and 1370 cm^{-1}) at 10V and the not-actuated device, is 2.592, 2.305, and 1.873, respectively. We started from these values to evaluate the effective enhancement in the gap region following the same approach already used in literature[8,9]

First, the contribution of the pillar and steady structure surface along the gap is constant during static measurements, while it is variable in dynamic mode. The number of molecules contributing to the plasmonic enhancement, however, can be assumed to be only those along the gap, and it is the same for perpendicular or parallel polarization, so only the signal from the former is considered for the enhancement evaluation. Second, it can be reasonably assumed that the enhancement is generated by the hot spots along the gap, and the hot spots are formed only when the pillar and the steady wall are closer than 2 nm to each other; this condition only lasts for a time interval comparable with the contact time, which can be estimated in 5% of the oscillation period.

The enhanced signal from an actuated device can be decomposed into three components:

$$S_A = S_{NA} + S_{GC} + S_{HS} \cong S_{NA} + S_{HS} \quad (3.2)$$

where S_A is the signal from the actuated device, S_{NA} the signal from the not-actuated device, S_{GC} the signal increase due to the gap covering during half oscillation and decrease during the second half of the oscillation and therefore average to zero for a whole oscillation period, and S_{HS} the enhanced signal generated in the hot spot locations. The previous spatial and temporal considerations must be introduced for the last two terms, while S_{NA} is constant for the whole oscillation period. Additionally, the enhancement from S_{HS} is integrated only in the hot spot formation area and lasts 5% of the oscillation period, as mentioned earlier.

With these considerations, the time-independent contribution from S_{HS} can be isolated:

$$0.05 S_{HS} = S_A - S_{NA} = 2.592 S_{NA} - S_{NA} = 1.592 S_{NA} \quad (3.3)$$

Finally, the total enhanced signal due to the hot spot formation only can be estimated to be $S_{HS} = 31.84S_{NA}$; the integration area can be approximated to a rectangle as wide as the laser spot diameter (412.5 nm, calculated from Equation 2.3) and as high as the distance at which the hot spot can be generated, resulting in a 2x825 nm^2 region, while the laser spot is a circle of radius 412.5 nm, again as calculated from Equation 2.3. Considering S_R the ratio of the integration surfaces for S_{NA} and S_{HS}, and τ_R the ratio between the period of the oscillation and the duration of the hot spot in terms of fraction of the oscillation period, the final estimation of the enhancement in a hot spot can be calculated with the formula:

$$EF_{HS} = 1.592\frac{S_R}{\tau_R} \quad 3.4$$

Resulting in an enhancement factor of 10315. This value represents a lower limit for the hot spot enhancement, since the resolution limit doesn't allow a proper signal collection from the hot spot area only and the temporal resolution of the method used in these experiments is not enough to discriminate between the contribution of the hot spot, of the pillar oscillation, and of the baseline signal. However, the estimated enhancement is compatible with the values found in literature for similar devices[10], thus confirming the validity of the approach. Moreover, here we have assumed that hot spots are formed continuously along the whole gap. In fact, the roughness of the two edges is larger than the gap of the hotspot and also during the contact time in some portion of the device the pillar edge will be more than 2nm far away the steady wall edge, thus resulting in no hotspot formation. However, this evaluation was not feasible, in particular it was not possible to evaluate the specific roughness at the laser spot location unless we had installed the Raman system within an SEM, which was not the case. We should therefore limit our estimation of the enhancement to a factor over 10000, being aware that this does not represent the exact enhancement but rather a lower limit.

3.4 Critical points and proposed solutions

The first, evident problem of the pillar devices is the uneven distribution of the enhancement along the gap between the pillar and the steady wall; in all the devices, the enhanced signal was created only in one of the collection points, always close to one of the edges. This event may be explained by a slight tilt of the pillar during oscillation: since the base of the pillar is overetched to obtain the tapering, the process can lose uniformity with increasing pillar height and create slightly asymmetrical pillar bases. These defects are too small to have a macroscopic influence on the pillar

motion, which appears uniform along the whole gap when viewed with a CCD or SEM, but a deviation of 20 nm from edge to edge can result in the formation of a hot spot only where the edge is closer than 2 nm while the other is still further away (Figure 3.13 (a)). Moreover, the hot spot is formed in concentrated regions of the laser spot due to the roughness of the gold surface (Figure 3.13 (b)) which creates isolated, nanometric contact points, much smaller than the collection points, so the surface ratio between the not-enhanced and enhanced Raman signal is unfavourable.

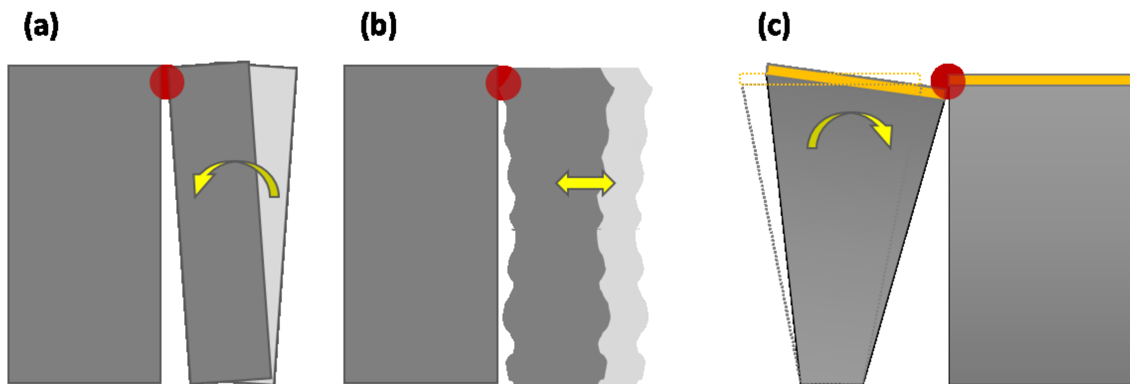

Figure 3.13 – Sketch of the critical points of the device: (a) tilting of the pillar top during actuation, causing the contact to be localized unevenly along the gap; (b) effect of the gold roughness on the hot spot area, resulting in very small enhanced regions; (c) effect of pillar, reducing the coupling efficiency between the plasmonic structures. Red circle: Raman signal collection point (not on scale). All the effects have been exaggerated for visualization purposes.

When the hot spot is formed, the reduced enhancement can be also attributed to an imperfect planarity of the pillar motion; even though the gap is much smaller than the pillar top width, the pillar can experience a small bending during oscillation (Figure 3.13 (c)). A misalignment of only a few nanometres can decouple the plasmonic nanostructures and reduce the hot spot intensity.

The redesign of the whole device must be undertaken in order to address all these issues and improve the performances of the device. The easiest problem to tackle is the pillar bending: the resonator can be designed to have the first oscillation mode parallel to the surface, to have a better coupling between the gold layers; this new design can include a better definition of the contact point through the insertion of a tip, which can avoid the uncertainty in the contact point localization underlined in Figure 3.13 (a).

References

(1) Melli, M.; Pozzato, A.; Lazzarino, M. Inverted Tapered Pillars for Mass Sensing. *Microelectron. Eng.* **2010**, *87* (5–8), 730–733.

(2) Postma, H. W. C.; Kozinsky, I.; Husain, A.; Roukes, M. L. Dynamic Range of Nanotube- and Nanowire-Based Electromechanical Systems. *Appl. Phys. Lett.* **2005**, *86* (22), 1–3.

(3) Zaitsev, S.; Shtempluck, O.; Buks, E. Nonlinear Damping in a Micromechanical Oscillator. **2012**, 859–883.

(4) Dyskin, A. V; Pasternak, E.; Pelinovsky, E. Periodic Motions and Resonances of Impact Oscillators. *J. Sound Vib.* **2012**, *331* (12), 2856–2873.

(5) Yasumura, K. Y.; Stowe, T. D.; Chow, E. M.; Pfafman, T.; Kenny, T. W.; Stipe, B. C.; Rugar, D. Quality Factors in Micron- and Submicron-Thick Cantilevers. *J. Microelectromechanical Syst.* **2000**, *9* (1), 117–125.

(6) Cheng, H. L.; Mai, Y. S.; Chou, W. Y.; Chang, L. R.; Liang, X. W. Thickness-Dependent Structural Evolutions and Growth Models in Relation to Carrier Transport Properties in Polycrystalline Pentacene Thin Films. *Adv. Funct. Mater.* **2007**, *17* (17), 3639–3649.

(7) Bettis Homan, S.; Sangwan, V. K.; Balla, I.; Bergeron, H.; Weiss, E. A.; Hersam, M. C. Ultrafast Exciton Dissociation and Long-Lived Charge Separation in a Photovoltaic Pentacene–MoS 2 van Der Waals Heterojunction (SI). *Nano Lett.* **2017**, *17* (1), 164–169.

(8) Bek, A.; De Angelis, F.; Das, G.; Di Fabrizio, E.; Lazzarino, M. Tip Enhanced Raman Scattering with Adiabatic Plasmon Focusing Tips. *Micron* **2011**, *42* (4), 313–317.

(9) Naumenko, D.; Toffoli, V.; Greco, S.; Dal Zilio, S.; Bek, A.; Lazzarino, M. A Micromechanical Switchable Hot Spot for SERS Applications. *Appl. Phys. Lett.* **2016**, *109* (13), 131108.

(10) Wei, H.; Xu, H. Hot Spots in Different Metal Nanostructures for Plasmon-Enhanced Raman Spectroscopy. *Nanoscale* **2013**, *5* (22), 10794.

4 Optomechanical devices for frequency-modulated plasmonic hot spot

Following the results obtained with the pillar device, in this chapter the fabrication, characterization and validation of the cantilever design are explained. The preliminary design steps and the fabrication outcome, the strategy followed to address the critical points of the pillar device and the investigation of the hot spot formation are presented.

4.1 Finite-element modelling

The first step to properly design the structures has been the finite-element modelling of their behaviour. The simulations have been carried out using different packages included in the commercial software COMSOL Multiphysics©.
COMSOL Multiphysics is a finite-element modelling software with an embedded parametric CAD interface to build the model of the system under analysis with different complexity: 1D, 2D or 3D structures (geometries) can be designed and modelled. The material properties of the whole geometry can be defined for each domain or object and the desired physics interface can be selected for each geometry. The geometrical entities are then divided into smaller volumetric units in which all the physical parameters are assumed constant following a specific scheme (mesh). The equations of the selected physical model are applied to the boundary conditions of each unit of the mesh to obtain the results for the complete geometry. The strength of this software, user-friendliness aside, is the ability to couple different physics on a single geometry: this allows for the simulation of complex phenomena, such as thermomechanical stress, piezoelectric behaviour, *et cetera*. This powerful feature has not been implemented in the models created for this project. Even though the plasmomechanical system could be simulated altogether, the mechanical and the plasmonic behaviour can be considered as decoupled; the system can be simulated independently for the mechanical and plasmonic properties, greatly reducing the required computational power.

4.1.1 Mechanical modelling

The cantilever device has been modelled to predict its mechanical behaviour (namely the stress distribution and the resonant frequency) for different geometrical configurations.

The 3D model of the cantilever device has been created reproducing the CAD drawings that will be used for the EBL patterns in the fabrication. The scallops caused by the Bosch process have been omitted due to the limited influence on the desired outcome of the simulation, so the resulting model is composed of smooth polyhedrons (Figure 4.1). No further details have been added to the model because it was meant only to evaluate the influence of the geometrical parameters on the resonant frequency of the device, in order to select the best design for the purpose of the experiments.

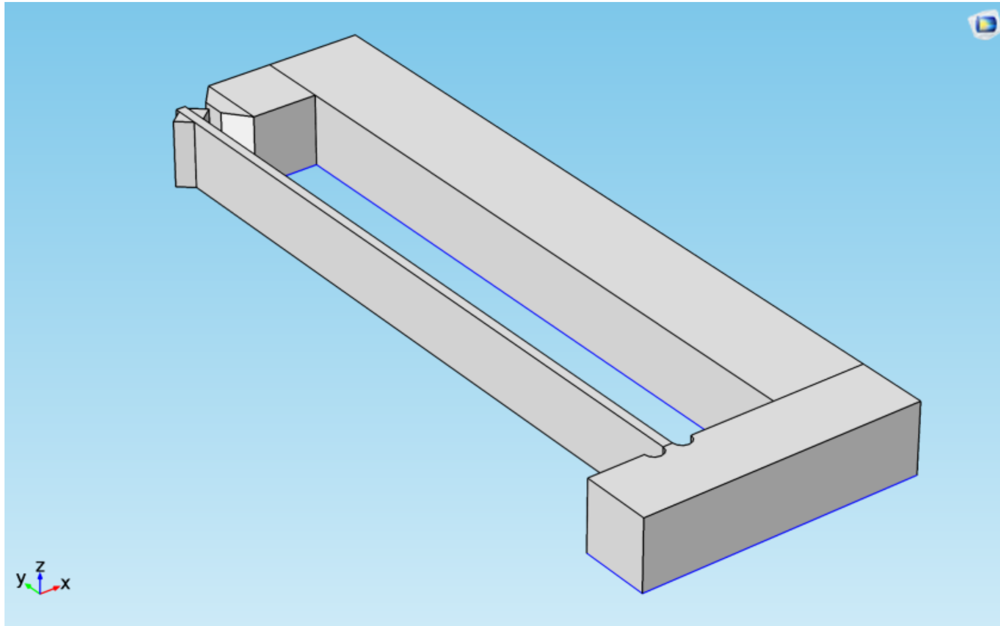

Figure 4.1 - Geometry of the cantilever device. The resonating arm is visible on the left side, equipped with the tips at the free end, while the L-shaped side of the model is the steady structure.

The displacement amplitude would have required a more complex, time-dependent simulation considering also the surrounding medium and the piezoelectric actuation; however, since the displacement is intrinsically limited by the geometry of the structure, such a complex simulation is not required, and the displacement amplitude can be evaluated experimentally. The gold layer has not been considered in the model since its effect on the resonant frequency is minimal: the lowering of the resonant frequency induced by the increased mass on the resonator is, in first approximation, balanced by the stiffening of the cantilever which pushes the resonant frequency to higher values. The data for different geometrical parameters are plotted in comparison with the solution of Equation 2.3 and 2.4 (see § 2.3.2) for the same parameter variation range. The trend of the simulated resonant frequency is in good agreement with the analytical solution, considering the approximations used in both models, when considering the dependence from the length of the cantilever. The behaviour is matching almost perfectly with Equation 2.3 and showing only a trend similarity with Equation 2.4 when the varying parameter is the cantilever width; this can be due to

the oversimplification of the tip shape, which is neither conical nor single in the device, in Equation 2.4: the symmetrical configuration used for the device allows for the minimization of the unbalancing due to the mass of the tip. The comparison between the geometry-dependent behaviour of the simulation and the trend of Equation 2.3 is shown in Figure 4.2.

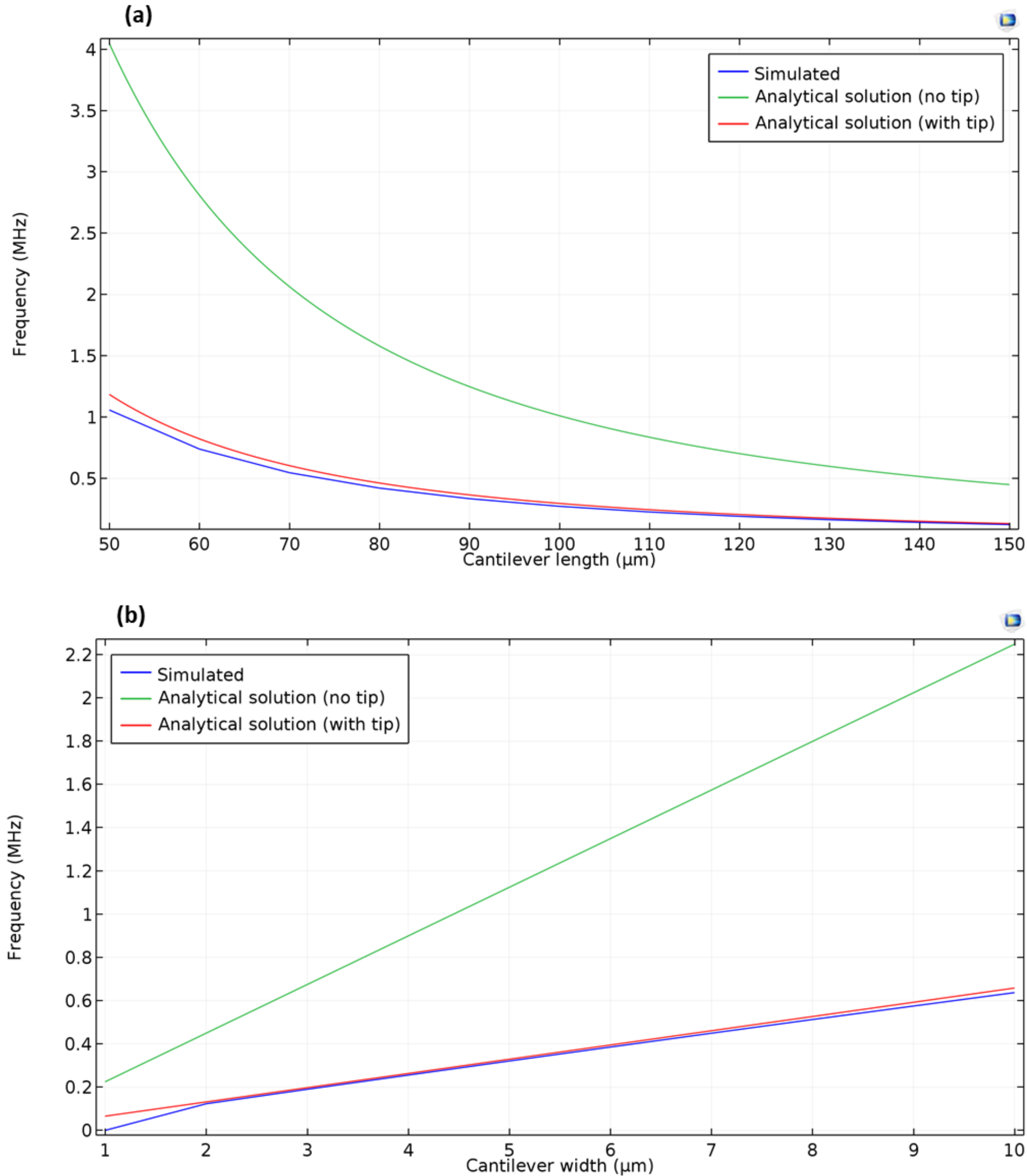

Figure 4.2 - Comparison between analytical and simulated trend of the resonant frequency for varying geometrical parameters. (a) Length dependence and (b) width dependence of the resonant frequency. The simulated data are obtained using the model shown in Figure 4.1, changed accordingly to the geometry of the cantilever. The analytical solutions are calculated from Equation 2.3 and 2.4 (see § 2.3.2)

The geometrical parameters of the cantilever are independent on any fabrication constraints, thanks to the micron-wide separation gap between the cantilever tip and the steady structure. The main consideration when designing this structure has been the resonant frequency, because a lower resonant frequency is useful for higher harmonics analysis of the modulated signal (explained

in detail later in § 4.4.2). The compromise of choice has been a resonant frequency in the range of 100 kHz, well within the dynamic range of our instrumentation for higher harmonics analysis, resulting in a geometry of 150x15x2 µm with a triangular tip shape of 1x2x15 µm.

4.1.2 Plasmonic modelling

Using the same software adopted for the design optimization of the cantilever device, an estimation of the plasmonic properties of the tip-wall interaction has been performed. The simulations can provide information about the distance at which the formation of a hot spot, if possible, is obtained and an estimation of the area where the field is enhanced by the plasmonic behaviour; for this purpose, a two-dimensional plasmonic model of the region of interest (ROI) comprising the tip and the wall has been set up.

The geometry has been designed with a rounded tip apex that is also present in the fabricated version of the device. The tip radius has been approximated with a semicircle of radius 300 nm and the laser beam spot has been modelled as a background illumination source, focused at the centre of the ROI, with a radius of 412.5 nm calculated from Equation 2.2 using the laser wavelength of 660 nm and the numerical aperture of the objective of 0.8. The geometry and the result of the simulation can be seen in Figure 4.3.

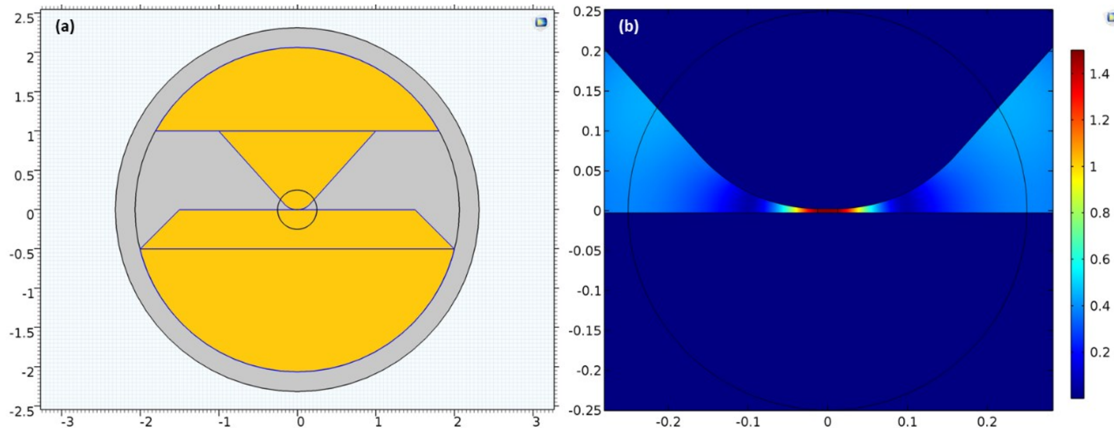

Figure 4.3 - (a) 2D geometry of the region of interest used in the electromagnetic simulation; grid dimensions in microns.(b) Simulation result for wavelength of 660 nm, gap width of 1 nm and perpendicular polarization. The color bar is the absolute value of the field enhancement calculated as the ratio between the scattered electric field and the background electric field.

Considering a background electric field of 1 V/m and a gap width of 1 nm, the norm of the electric field in the gap is increased only when the polarization of the incident light is along the separation gap, similar to what can be observed in the presence of a plasmonic hot spot. A punctual enhancement factor can be calculated dividing the final electric field in the centre of the gap by the initial electric field in the same point; the enhancement factor calculated with this method is not

indicative of the real enhancement achievable with this structure, since the value coming from one point alone cannot account for the effect on a whole surface and doesn't consider the effect of the interaction of the electric field with the molecules that can be excited by the field in the gap.

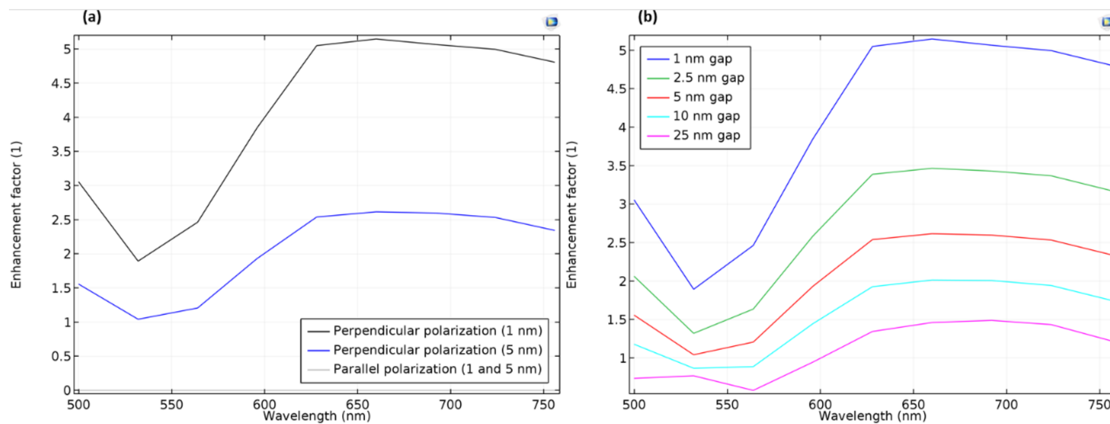

Figure 4.4 - (a) Polarization dependence of the enhancement in the middle of the gap; enhancement factor for 1 and 5 nm gap with perpendicular (black and blue lines) and parallel (grey lines) polarization plotted against wavelength. (b) Distance dependence of the enhancement in the middle of the gap for 1 (blue line), 2.5 (green line), 5 (red line), 10 (cyan line), and 25 (magenta line) tip-wall distance. The enhancement factor is almost zero for parallel polarization on all the wavelengths considered in the simulation (a) and is reduced with increasing gap size (b).

The simulated results are in accordance with the simulation of a similar model, composed of a dimer of two identical gold nanoparticles of radius compatible with the curvature radius of the tip; the transition between the dimer of nanoparticles and the tip-wall model, one nanoparticle in close proximity to a wall, has also been simulated, confirming again the results obtained before. The simulations for the dimer of nanoparticles and the wall-nanoparticle system have been performed using the same parameters used for the simulation of the tip-wall interaction to make the three results fully comparable.

Another confirmation of the plasmonic nature of the enhancement is the evaluation of the gap-dependent behaviour. For different distances between the tip and the steady wall, an exponential decay is expected from theory and literature[1]. The simulation results show this dependence, as demonstrated by the plot in Figure 4.5; the same trend is replicated in the result of the three plasmonic simulations, which confirms the quality of the transition from the simplest model (gold nanoparticles dimer) to the intermediate (gold nanoparticle and wall) to the final geometry (rounded tip and wall). A decrease of the enhancement factor can be observed in the transition between the dimer and the tip-wall simulation; this can be attributed to the shape of the scattering objects, which influences the plasmonic behaviour of the whole system.

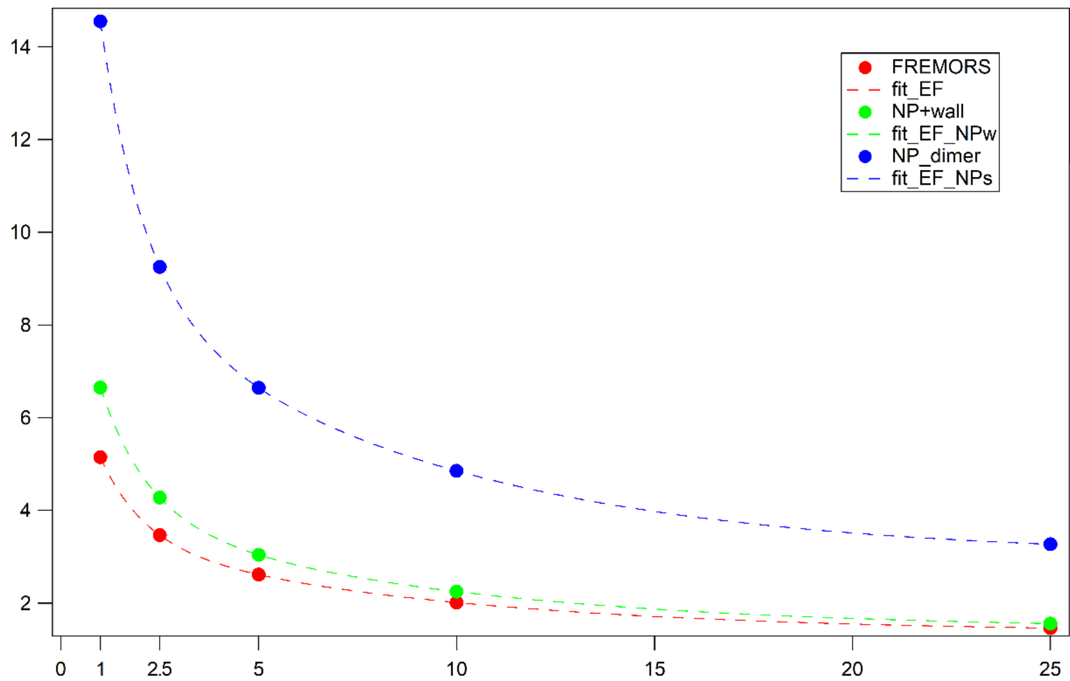

Figure 4.5 – Distance dependence of the enhancement factor in the central point of the gap between the tip and the steady wall (red curve), the nanoparticle and the wall (green curve), the two nanoparticles (blue curve). The full circles are calculated values, the dashed line is an exponential trend (drawn for ease of visualization).

The enhancement has been also estimated along a 160 nm long segment parallel to the *x* axis, crossing the (0,0) of the geometry in its middle point. The evaluation of the distribution of the field enhancement can be useful for the calculation of the SERS enhancement factor of the real device.

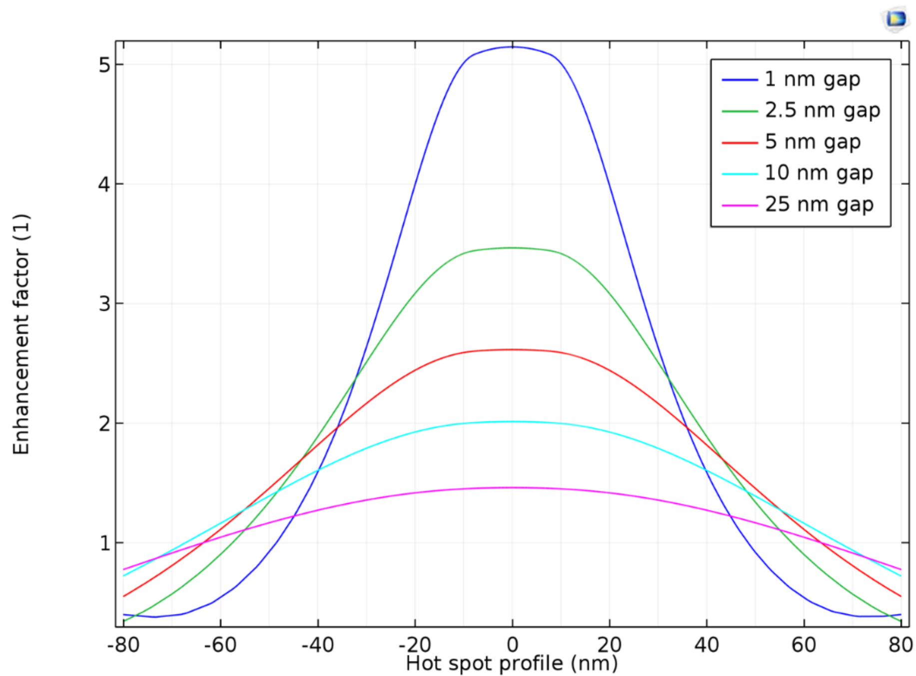

Figure 4.6 - Evaluation of the hot spot profile along a segment parallel to the wall for varying gap width. The excitation wavelength is 660 nm.

The resulting profile shows the maximum enhancement in a 20 nm-wide section, rapidly decreasing until no enhancement remains in the long range, and a FWHM of 60 nm (Figure 4.6). In this region where the enhancement is maximum, and the hot spot formation is more probable, the nanometric roughness of the real gold layer (not considered in this simulation) can create multiple hot spots, all of them behaving similarly to a dimer of gold nanoparticles: the total enhancement of such a system is in principle much greater than the value obtained from the simulation. Moreover, the material properties used in the model are bulk properties and, even though the software can consider the geometry a surface, the results could be improved if the gold layer could be simulated as a thin film.

4.2 Fabrication of the devices

The fabrication of the cantilever device has been carried out using conventional fabrication techniques (see § 2.1 for the explanation of the technique and § 2.4.1 for more details about the processes actually used). The vertical walls are slightly underetched to ensure the contact between the cantilever tip and the steady wall on the top surface only; this has been obtained with a careful tuning of the ICP-RIE etching parameters. The tip apex is not sharp on purpose: the repeated hits of a sharp tip on the wall could damage the gold layer and affect the plasmonic behaviour of the device. While fabricating the cantilever device, the detaching of the suspended cantilever from the SOI substrate is necessary to obtain a resonating arm. The selective wet etching of silicon oxide in a solution of water and hydrofluoric acid (HF:H_2O 1:10) is required to obtain suspended cantilevers; the very high ratio between the width of the cantilever tip and that of the C-shaped support ensures detaching of the resonating arm without damaging the steady structure.

To have a first measure of the silicon oxide etching stage, pillars are added to the EBL pattern in the area between the cantilever and the C-shape of the steady structure. The falling of these structures, anchored on the BOX layer of the SOI wafer, is a first indicator of the ongoing stage of the etching process (Figure 4.7 (a)). Moreover, the presence of the pillars allows a more uniform etching and can help reduce the undercut below the steady structure.

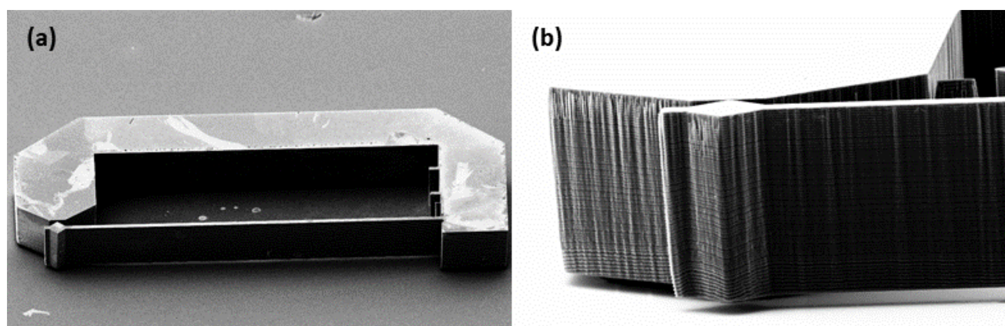

Figure 4.7 – SEM images of a completely fabricated device: (a) tilted view of the whole structure; (b) side view of the tip, where the complete detaching of the resonating arm can be appreciated.

The detachment of all the cantilevers (an example is shown in Figure 4.7 (b)) has been obtained, thus demonstrating a correct optimization of the fabrication process.

After the successful release of the cantilevers, the optimization of the gold layer deposition has been performed: a homogeneous layer is crucial to ensure good plasmonic properties of the surface and a uniform functionalization. The e-beam evaporation technique, explained in § 2.1.1, has been used to deposit a thin uniform gold film of 80 nm; the e-beam evaporation technique produces a film of purer material which exhibits better adhesion to the silicon substrate without the need for an adhesion layer, which can dampen the plasmonic properties of the gold layer. The metal film can be functionalised with BT-Azo via immersion coating (see § 2.2.1 and § 2.4.2).

4.2.1 Cleaning and disposability considerations

Since the smallest geometrical features of the structure are in the range of 1 µm, the serial production of the devices for commercial use is feasible even on large wafer scale using optical lithography techniques; the perspective output in terms of number of devices per wafer ranges from thousands to tens of thousands based on wafer dimension and the large-scale production would decrease the cost per unit to levels comparable with similar disposable devices, e.g. commercial AFM chips. Therefore, the devices are designed to be disposable and do not require test about efficacy of, and resistance to, cleaning procedures.

The use of a disposable device in the field of Raman and SERS substrates is advisable, since cross-contamination between different measurements must be considered. The cleaning processes required to regenerate a device for an efficient and contamination-free usage range from harsh chemical protocols, like piranha or RCA solutions, to long sessions of dry cleaning in oxygen plasma; even after these processes, not every contaminant is guaranteed to be eliminated, since some kind of molecules can create complexes with the gold film which are even more difficult to remove. Moreover, strong cleaning protocols can damage the gold film, strongly reducing or even

completely quenching the plasmonic properties of the devices. Every chip containing several devices has been tested for resistance to cleaning protocols after the characterization of the devices; while oxygen plasma cleaning is not enough to remove contaminants and analytes from the gold surface, piranha cleaning stripped the gold from the structures, cantilevers and the steady walls alike, making the devices useless. Nevertheless, we noted that the robustness of the devices is much higher than the durability of the test analytes, deeming further characterization in this regard unnecessary.

4.3 Preliminary characterization

4.3.1 Rayleigh scattering mapping

After the fabrication, gold layer evaporation and functionalization of the devices with the BT-Azo dye, the samples have been mounted on a piezoelectric actuator glued to a glass slide used as physical support. This system has been placed on the XY stage of the optical characterization setup described in § 2.4.3.2, which provides the laser illumination, the collection optics and the signal detectors, whose response is elaborated by the lock-in electronics. More in detail, the laser is focused on the gold surface of a device and the sample is then moved using the TAO module of the AFM, which controls the XY sample stage. The Rayleigh scattered light (*i.e.* the light elastically scattered from the surface) is collected, filtered using a spectrograph set at the laser wavelength, and its intensity measured with an avalanche photodiode. The signal from the photodiode is directly sent to the AFM controller, combined with the position of the XY stage controlled by the TAO module and used as the intensity signal for the creation of an XY image, which appears like an AFM image in which the Rayleigh scattering intensity replaces the topographic information obtained with conventional AFM imaging. A sample image is shown in Figure 4.8 (a), where each pixel corresponds to a position of the XY piezo stage and the intensity to the signal coming from the photodiode.

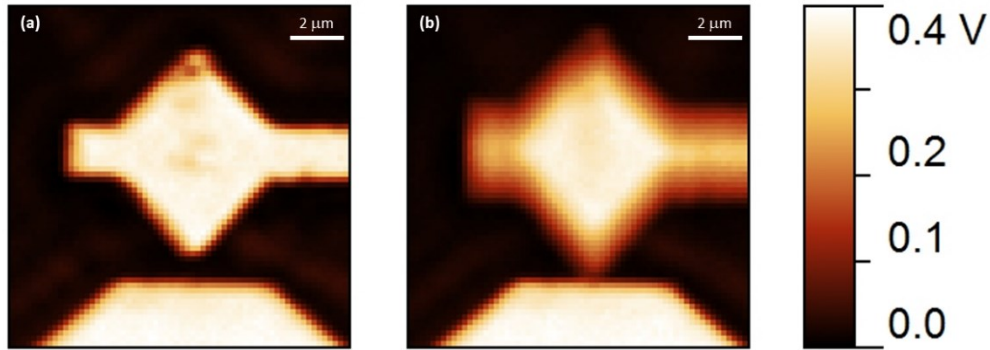

Figure 4.8 - Reflectivity mapping of the cantilever tip end and the steady wall in static (a) and dynamic (b) mode. The blurred area surrounding the cantilever tip is created by the controller, which integrates the signal over a time interval much longer than the oscillation period.

The mapping of the surface has been used to evaluate the uniformity of the gold layer surface, since the wavelength of the laser used is very far from the absorption peak for the BT-Azo, which falls in the wavelength range of blue light (around 455 nm) and decreases to almost zero for wavelengths over 600 nm[2] A uniform gold layer is required, especially in the regions close to the edges of the device, to have homogeneous plasmonic properties, in order to avoid artefacts during the search for the hot spot in the contact point. Moreover, the quality of the gold layer determines the uniformity of the BT-Azo dye film after the functionalization.

During and after the mechanical characterization, the mapping is repeated during actuation to visualize the exact contact region between the tip and the steady wall. The result of this second step can be seen in Figure 4.8 (b) and similar maps will be used in other steps of the experiment. A detailed description of the results of this characterization will be given in the next paragraph.

4.3.2 Mechanical characterization

The cantilever has been characterized only in air to have a direct response from the device in its final operation environment. The considerations about the impact oscillator behaviour have been deemed of secondary importance for this new design, so only a basic characterization of the mechanical motion is required. The technique and the experimental setup have been described in detail in § 2.4.3.2: the working principle of this setup is the change in the amount of reflected light detected by a photodiode when the tip is moving in and out of the laser spot. A sketch of the method has been shown in Figure 4.9.

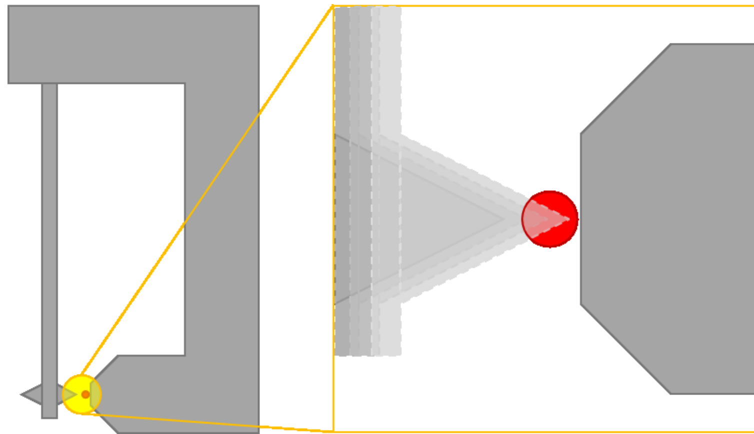

Figure 4.9 - Working principle of the setup for the mechanical characterization of the cantilever device. The laser is focalized on the top of the steady structure and then moved in the gap (left). During actuation, when the cantilever is in resonant condition the tip moves in and out of the laser spot (right), causing an increase in the reflected light and thus a higher signal detected by the photodiode.

The resonant frequency of each device has been evaluated after the complete fabrication and functionalization, as described in the previous paragraph, to test the devices under the final working conditions. The measured resonance frequencies, all slightly different from device to device due to fabrication tolerances, were lower than those simulated with COMSOL Multiphysics; this can be easily explained with the additional mass of the gold and BT-Azo layers, the damping of air and the intrinsic uncertainties of the fabrication. For each measured cantilever device, the appropriate actuation voltage at the resonance frequency is analysed through a voltage scan to evaluate the minimum voltage corresponding to an oscillating amplitude large enough to bring the cantilever in contact with the steady wall. The typical frequency and voltage response is shown in Figure 4.10:

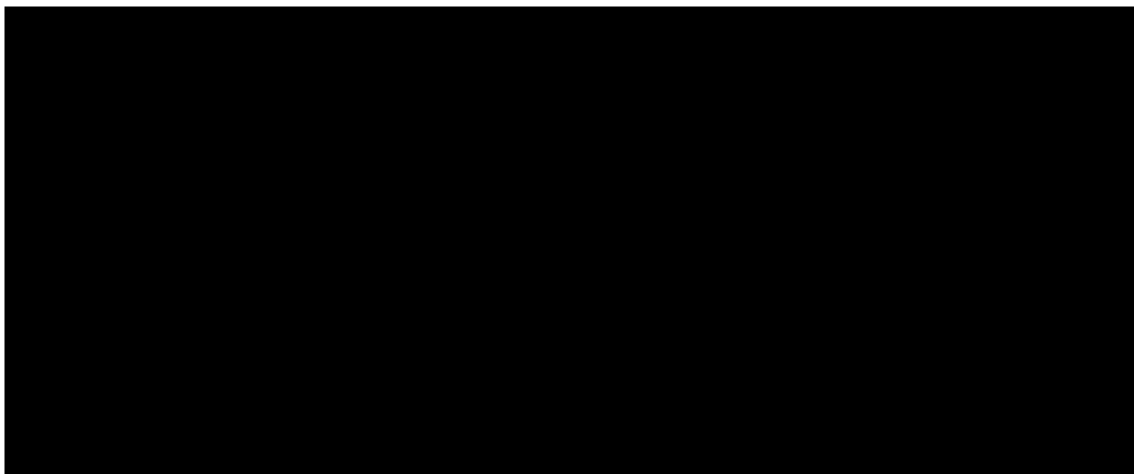

Figure 4.10 - (a) Frequency response of a cantilever device as measured with the method described above; the signal is the Rayleigh scattered light (i.e. the reflected light) measured in amplitude and phase with a lock-in amplifier. The phase (dashed line) values are measured in degrees on the right axis. (b) Actuation voltage dependence of the same cantilever actuated at the resonant frequency. The dashed lines indicate the typical parameters of choice for the experiments.

The graph of the frequency response has shown the trend of a mechanical resonance[3]: the amplitude response is sharp and its shape can be fitted with a Lorentzian curve, the phase has a flex point corresponding to the resonant frequency value. For the frequency response measurements, the maximum voltage possible has been applied to the piezoelectric actuator (10 V_{pp}). The frequency response of the cantilever has been obtained with a minimum frequency step of 100 Hz to get an accurate result in a reasonable time; the resolution could be further increased but it is not required for the following experiments, since 100 Hz precision means (at most) an error range of ±0.15% of the actual value. The amplitude of the cantilever oscillation has been evaluated using the same technique described earlier for the frequency response, with a simple modification: the frequency has been set to the resonant frequency value, while the applied voltage has been scanned, using the same collection point described in Figure 4.9. The voltage response curve has a sigmoidal shape, with an initial flat region in which the movement is too small for the tip to reach the laser spot, a linear region in which the illuminated area of the tip grows proportionally with the voltage, and a final plateau in which the amplitude of the movement (hence the illuminated area) cannot grow further due to the limit imposed by the presence of the wall, meaning that the contact condition has been achieved. The same considerations about the resolution can be applied to the voltage scans: each curve has been obtained with a resolution of 0.1 V, typically in the range 1-10 V. The voltage chosen for the experiments is the value that corresponds to the beginning of the contact plateau, to be reasonably sure that the tip of the cantilever would be close enough to the steady wall for the best experimental conditions. An excessive actuation voltage, beside undesired heating of the piezoelectric actuator, could damage the gold layer in the contact point due to the increased strength of the impact of the tip on the wall.

Due to the spatial constraint that must be considered for the hot spot formation, a clearer understanding of the tip path and the time interval during which the tip is close enough to create the hot spot must be undertaken. For this purpose, the lock-in amplifier was replaced with a gated photon counter, as described in § 2.3.5. After focusing on the edge between the steady wall and the gap at the expected contact point, the resonating arm has been actuated and the Rayleigh scattered light acquired with the avalanche photodiode; the pulses from the photodiode can be counted over very short time intervals from the gated photon counter scanning the counting delay, thus recreating the time-dependent behaviour of the resonator during motion.

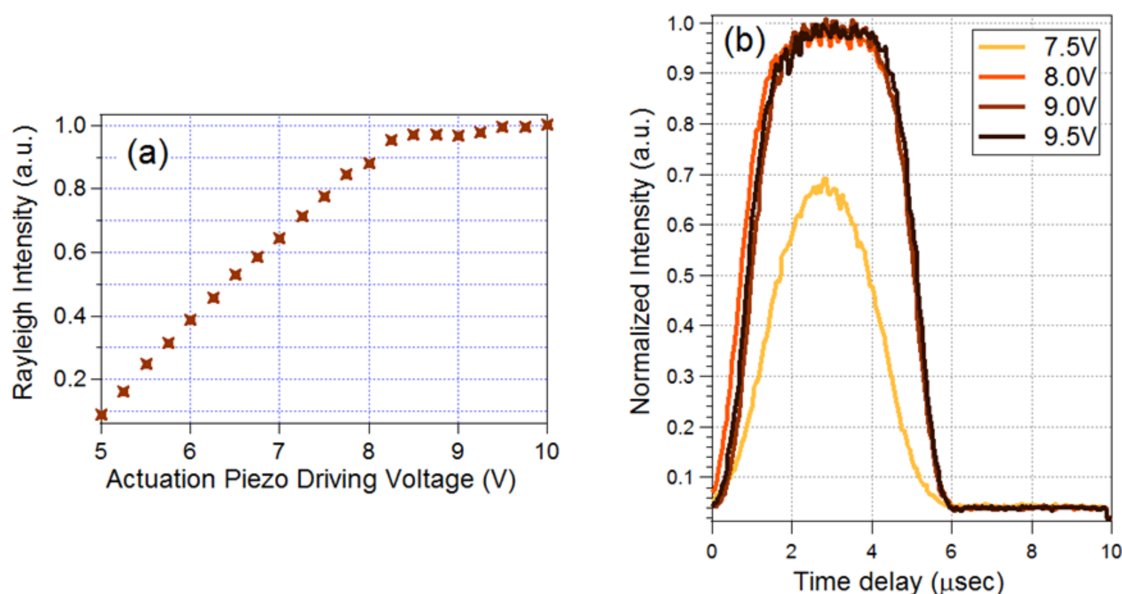

*Figure 4.11 -**(a)** Determination of the actuation voltage required to achieve contact between the tip and the wall; **(b)** Rayleigh scattering intensity during a single oscillation cycle of the cantilever. Data have been normalized to [0,1] for easier visualization.*

The data in Figure 4.11 (b) have been obtained for different actuation voltages to analyse the different behaviour of the cantilever for small and large displacements. For actuation voltage below the contact regime, the Rayleigh intensity follows a sinusoidal profile given by the convolution of the cantilever position and the laser spot size. For actuation voltage above the contact regime the intensity shows a saturation, which corresponds to the fraction of the oscillation cycle in which the hot spot is formed. Using this method on all the devices measured, the cantilever has been determined to be in quasi-contact conditions, required for the hot spot formation, for about 1.5 μs over an average oscillation period of 10 μs.

4.3.3 BT-Azo dye film characterization

The device has been functionalized with benzotriazole-azo dye (BT-Azo). BT-Azo is a molecule, whose structure is shown in § 2.4.2, specifically designed for experiments with SERRS (surface-enhanced resonant Raman scattering) studies. This dye has been selected for several reasons: it has a strong and well identifiable Raman signal; it can be physisorbed to a noble metal surface through immersion coating and subsequent rinsing to remove excess dye; after the functionalization, it is stable at room temperature and does not degrade when exposed to air. The main features of the Raman spectrum of BT-Azo can be found in the range of 1000-1700 cm^{-1}, with the highest peak found at the Raman shift of 1292 cm^{-1} (a combinational mode generated by the interaction of the aromatic rings with the azo group) when using an excitation wavelength of 660

nm; as already demonstrated, this excitation wavelength is able to excite the dye in pre-resonant conditions[2,4]. The charged benzotriazole group facilitates the electrostatic interaction with the gold surface and this property has been exploited to obtain a thin film of a Raman-active molecule whose signal can be exploited to investigate the presence of a plasmonic enhancement of the electromagnetic field in the tip-wall contact region. After the dip coating of a chip containing the devices to be analysed, appropriate rinsing must be executed using the same solvent in which the dye is dissolved, methanol, in order to remove excess molecules accumulated over the device itself; the reaction time must be long enough to ensure proper bonding of the molecules, otherwise most of them could be removed during methanol rinsing, therefore the sample have been immersed in the dye solution overnight. After the functionalization of the surface, the presence of the BT-Azo has been ascertained performing Raman spectroscopy on the top of the steady structure, since the functionalization should be uniform over the whole device. The results are shown in Figure 4.6, where the measurement location and the Raman spectrum obtained have been shown.

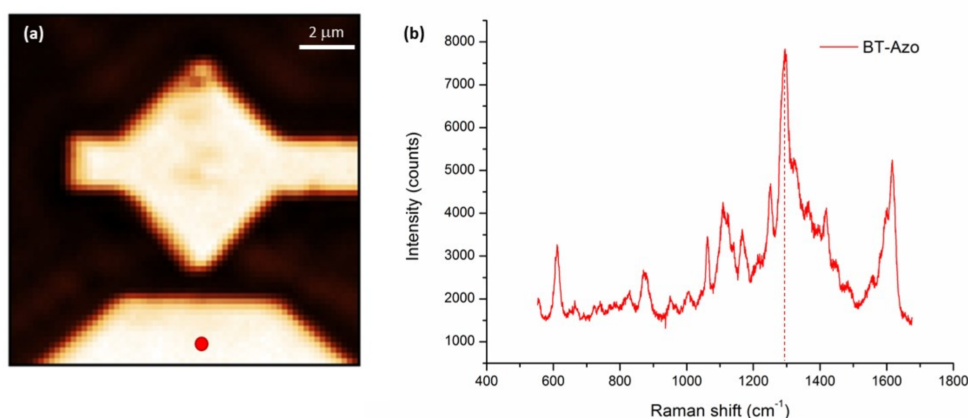

Figure 4.12 - (a) Rayleigh mapping of the region of interest where the Raman scattering signal has been collected (the red circle indicates the location). (b) Raman spectrum of the BT-Azo collected from the functionalized device.

The spectrum of the BT-Azo is well in agreement with those found in literature[5]. The characterization of the BT-Azo film uniformity has been carried out using the same kind of mapping already described earlier (see § 4.3.1), with the spectrograph set to the Raman shift corresponding to the highest peak of the spectrum in Figure 4.12 (b) (1282.75 cm^{-1}, dashed line).

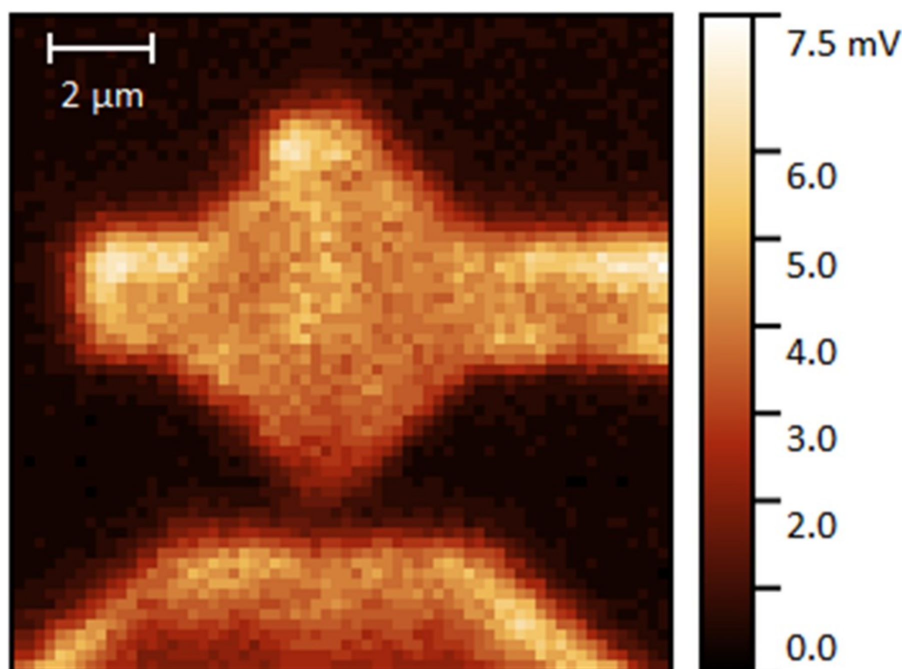

Figure 4.13 - Raman mapping of the region of interest. The intensity of the signal is much lower due to the very low probability of the Raman scattering phenomenon. The BT-Azo is present on the whole device, with good uniformity.

Switching from Rayleigh to Raman scattered light required a double acquisition time and therefore a lower number of points has been selected; a more resolved image would require longer acquisition times, which can lead to unwanted heating of the surface that would damage the dye film. The uniformity of the BT-Azo film has shown to be lower than the gold layer underneath; reasons for this small inhomogeneity can be either the imperfect functionalization of the gold layer, due to imperfect cleaning of the device before the immersion in the BT-Azo solution, or to nanometric-size defects of the surface, which can create zones of lower affinity with the BT-Azo molecules.

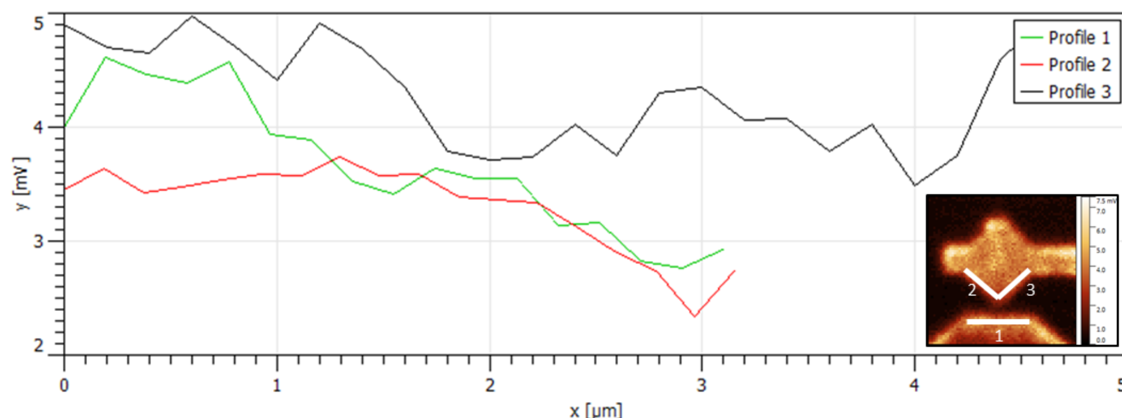

Figure 4.14 - Signal distribution along three lines in the region of interest. The graph of Profile 1 is the distribution of the BT-Azo along the edge of the steady structure, while the graphs of Profile 2 and 3 represent the distribution of BT-Azo along the edges of the triangular tip. Inset: figure 4.8 with lines marking the locations of the profiles in the graph.

Even with these defects, the 1292 cm^{-1} Raman signal detected in the most relevant parts of the region of interest (*i.e.* the end of the tip and the edge of the steady wall) is homogeneous in the range of ±25% (see Figure 4.14) taking as reference the average value along each line. The uniformity on the wall edge is higher, in the range of ±10%.

4.4 Dynamic mode mapping

The cantilever device has been mapped also in dynamic mode, the first step being the mapping of the device with the same methods described in the previous paragraph during device actuation. The Rayleigh and Raman maps are shown in Figure 4.15 below.

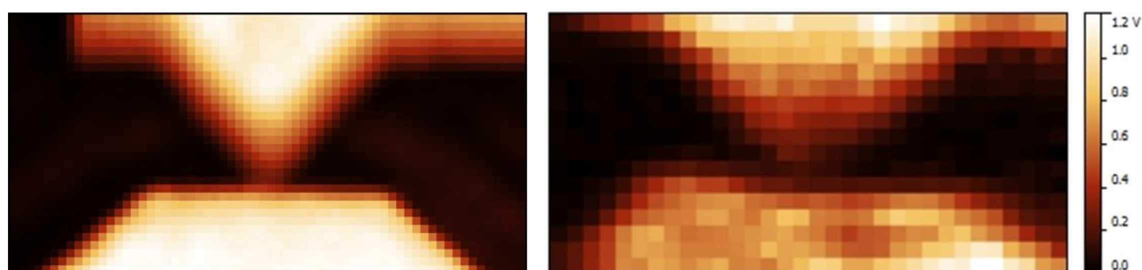

Figure 4.15 - Mapping of the actuated device using Rayleigh (left) and Raman (right) scattered light.

The mapping of the actuated device has shown a blurred area in the gap between the tip and the steady wall, that is the path followed by the tip during motion. The blurring is due to the difference between the resonant frequency of the cantilever and the sampling ratio of the AFM controller; even during Rayleigh mapping, which is twice faster than Raman mapping, the pixel sampling speed is 1280 Hz, while the typical resonant frequency of the devices is around 90 kHz, over seventy times higher. This long integration of the signal causes the averaging over more than seventy periods of the signal coming from the mechanical motion of the tip under the laser spot, which is proportional to the time spent by the tip under the spot: the wider the motion of the cantilever, the longer the device is under the spot, and the higher the integrated signal.

4.4.1 Parallel and perpendicular polarization

As already explained in the first chapter (§ 1.d), the formation of a plasmonic hot spot is a phenomenon that is strongly dependent from the polarization of the electromagnetic field incident on the sample: when the light is polarized along the gap between the two nanoparticles or nanostructures a hot spot is formed, otherwise no concentration of the electromagnetic field is obtained. The mapping of the actuated device with Raman scattered light has been performed accounting for this parameter. The laser light polarization in the focal point after the optical path

has been determined using a linear polarizer ($\lambda/2$) and the sample rotated accordingly, to obtain a polarization direction either perpendicular or parallel to the wall.

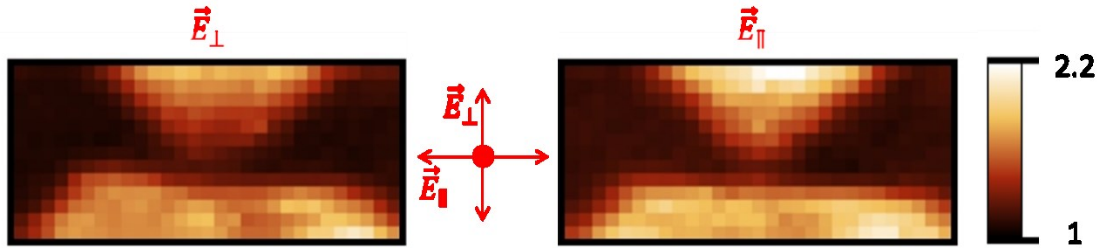

Figure 4.16 - Raman scattering maps of the actuated device with different light polarization: perpendicular (left) and parallel (right) to the steady wall. The direction of polarization of the electric field in the laser spot is illustrated by the arrows between the maps. Colour bar in volts.

Unfortunately, by integrating the signal over many cantilever oscillations the Raman signal coming from the small region of the hot spot is covered by the less intense signal but originated continuously for the much larger area of the cantilever surface. To extract the signal from the hot spot we need to address a more complex frequency dependent analysis.

4.4.2 Lock-in signal deconvolution

It has been evident, since the first mappings with Raman scattered light, that the hot spot wouldn't be possible to be visualized in this way. The number of pixels of the Raman maps is enough to get close to the resolution limit of the laser optics, since the map obtained as in Figure 4.16 have a horizontal dimension of 10 µm divided into 32 square pixels; the size of those pixels is then 312.5 nm, which is already lower than the ideal spot size of the laser (412.5 nm, calculated with Equation 2.2). The Raman signal is also much lower than the Rayleigh signal, due to the very low probability of this scattering phenomenon (1 in 10^9 incoming photons is Raman scattered, see § 1.1.2), therefore the signal-to-noise ratio is very low; the contrast between the enhanced Raman signal coming from the hot spot and the surrounding Raman signal coming from the tip and the steady wall during cantilever motion cannot be achieved with simple mapping, even exploiting a favourable polarization of the light. Moreover, the duration of the hot spot is comparable with the time during which the tip is within a few nanometres from the steady wall, and the conventional mapping system integrates the signal over a much longer time. To overcome these problems, a deconvolution of the signal has been performed. The signal coming from the mapping of the actuated device has been fed to a lock-in amplifier, which is capable to extract the signal which is in phase with a reference; the reference signal, in these experiments, is the SYNC signal generated from the function generator used to actuate the piezo. The choice of demodulating the signal to

single out the hot spot contribution is based on the assumption that the hot spot is modulated at the same frequency at which the cantilever resonates.

The scattered signal collected from the actuated device and filtered by the lock-in amplifier comes only from the parts of the device which move at the actuation frequency, excluding the contribution from the other zones of the ROI. The result of the maps generated through the lock-in demodulation is shown in Figure 4.17:

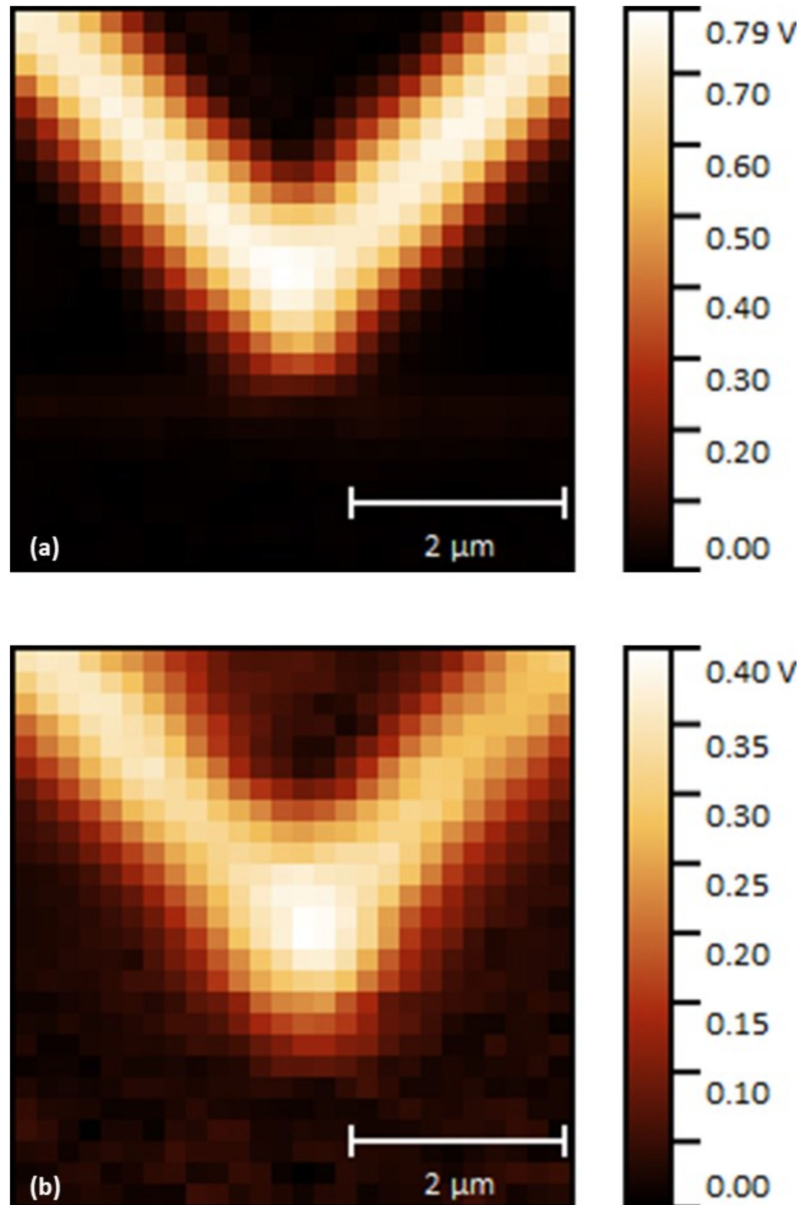

Figure 4.17 - Rayleigh (a) and Raman (b) mapping of the actuated cantilever deconvoluted at the first (fundamental) harmonic of the resonant frequency.

The lock-in processing of the signal allows the selection of the contribution coming from a single frequency multiplying the input signal by a reference waveform: this creates a continuous signal proportional to the components with the same frequency of the reference and additional signals

of different frequencies proportional to the components of the input which are not modulated at the reference frequency. A low-pass filter applied after the multiplication rejects every modulated signal leaving the continuous signal only, thus selecting only the signal coming from the light which is scattered while modulated at the resonant frequency of the device. This is useful to assess the feasibility of the mapping with this signal processing, assessment done using Rayleigh scattered light: the only signal above the noise threshold comes from the parts of the device oscillating at resonance. After obtaining the map in Figure 4.17 (a), the spectrograph has been set to select Raman scattered light only and Raman mapping has been performed; unfortunately, the hot spot signal is still hidden beneath the contribution from the mechanical motion of the cantilever.

The demodulation of the Raman signal at the fundamental harmonic has given no clue about the presence and position of the plasmonic hot spot; as already presented in § 1.4.1, a better contrast is achieved for deconvolution of increasing harmonics. Therefore, the maps have been deconvoluted at up to the fourth harmonics. To understand the behaviour of the oscillating cantilever using higher harmonics deconvolution, this technique has been applied to the Rayleigh scattered light signal; obtaining this map is faster since the acquisition and integration times are lower, so they can be a good benchmark where to test the method.

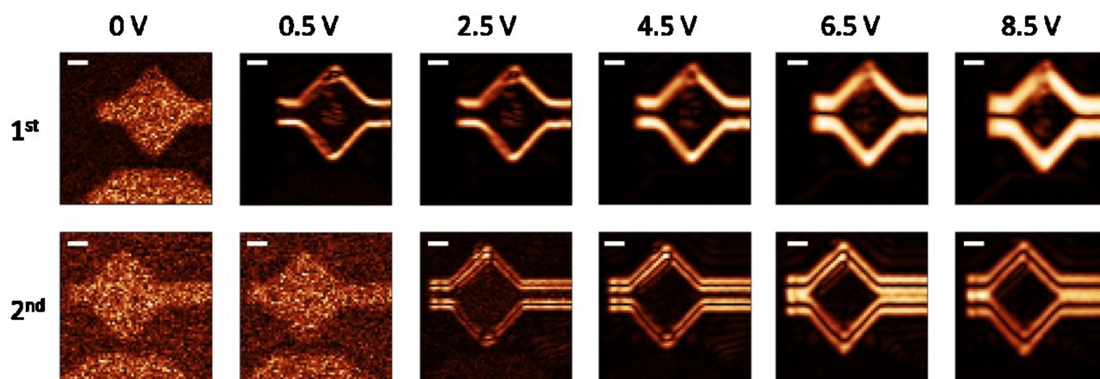

Figure 4.18 - Demodulation of the Rayleigh scattered signal at first (top row) and second (bottom row) harmonics for the actuated device at different voltages (indicated above each column). The very low signal-to-noise ratio of the 0 V maps is due to the very low intensity of any frequency, while the 0.5 V map for the second harmonic is low due to the weakness of the signal introduced by the higher harmonic modulation. Scalebars are 2 μm.

The deconvoluted maps for first and second harmonic show the contribution from the moving parts of the device only; the main difference between the two is the formation of the V-shaped pattern along the trace of the moving cantilever edge. The pattern has periodic features along the resonating arm, proportional to the harmonic selected for the deconvolution: one trace for the first, two for the second, and so on. This is caused by the lock-in signal processing itself, which multiplies the incoming signal by the reference or its harmonics. To verify this hypothesis, mapping at different actuation voltages have been acquired. The mapping of the cantilever for small and large motion

matches well the predicted pattern formation. A graphical explanation of this phenomenon is given below, provided for five specific points but can be extended to all the other positions in the map.

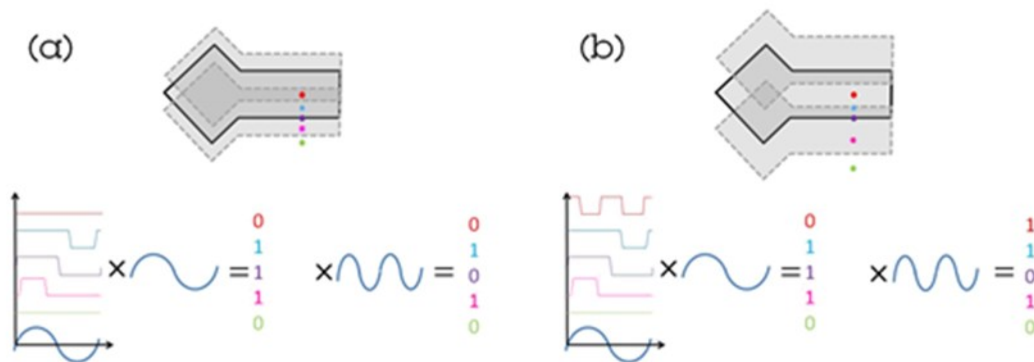

Figure 4.19 - Ridge formation during signal deconvolution for (a) small and (b) large cantilever oscillation. The graph traces on the left for (a) and (b) show the recorded path in the collection points depicted above; the zeros and ones on the right after the equal sign indicate the high (1) or low (0) signal recorded by the lock-in amplifier when the traces in the graph are multiplied by the first or second harmonic of the reference signal.

The reason for different pattern formation in the middle of the cantilever for small or large motion condition is straightforward. For small amplitude oscillations, the signal from the centre of the cantilever is not modulated since during an oscillation period the reflectivity under the laser beam is constant (not modulated): therefore, the centre of the image appears black in the first harmonic image. When the oscillation amplitude approaches the thickness of the cantilever, it may exit from the laser spot, providing lower Rayleigh scattering: the signal becomes modulated at the cantilever oscillation frequency and a non-zero signal appears also in the centre of the image in the second harmonic map. The positions along the cantilever in which this happens increase with the actuation voltage (*i.e.* with the oscillation amplitude) as show in Figure 4.18. The behaviour of the points near to or along the edge is the same in both conditions. The mapping of the actuated device using the deconvolution has been performed also at higher harmonics, as in Figure 4.20. The different patterns around the resonating arm are formed when the signal coming from locations which spend under the laser spot a fraction of the oscillation period which is different from half the period is multiplied by a multiple of the resonant frequency: the integration time is always longer than the oscillation period and its harmonics, causing an averaging effect which reduces to zero the periodic alternation of positive and negative outcomes of the multiplication. If the fraction of period is $\frac{1}{2n}$ (*i.e.* the denominator is even) the integrated signal will be positive when multiplied at every even harmonic deconvolution; if the fraction of period is $\frac{1}{2n+1}$ (*i.e.* the denominator is odd) the integrated signal will be positive at every odd harmonic deconvolution. The higher the harmonic selected, the smaller the fraction of period that will be visualized, thus increasing the number of black-and-white alternating lines on the map.

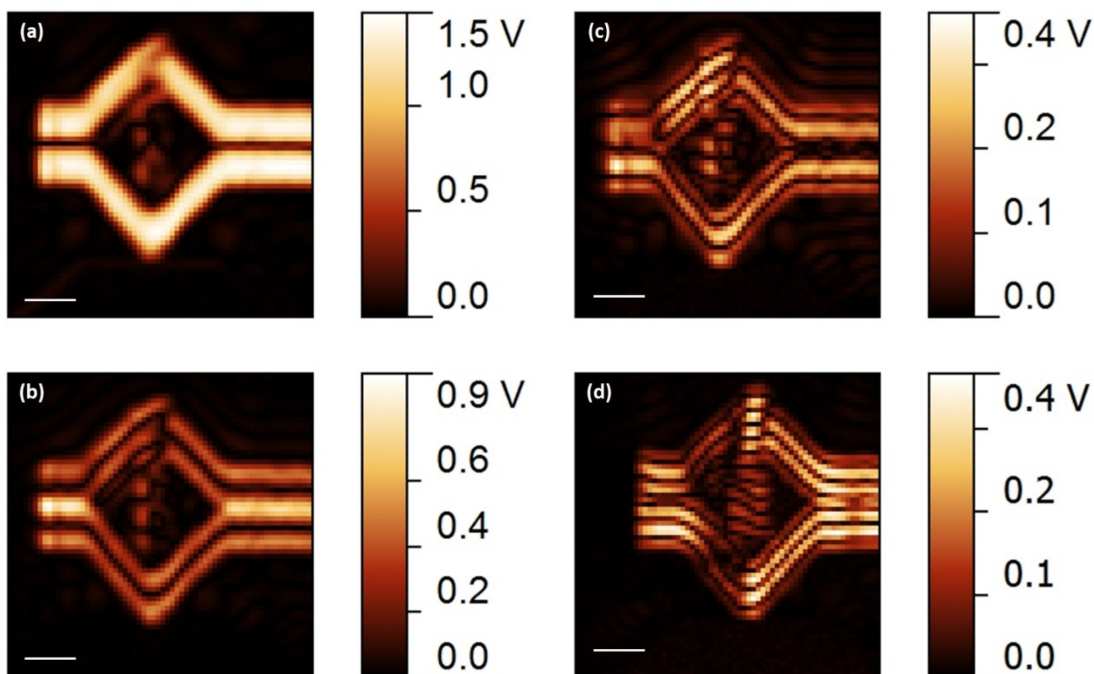

Figure 4.20 - Rayleigh maps at higher harmonics: first (a), second (b), third (c), and fourth (d). The ridges observed after the deconvolution are artefacts created by the lock-in signal processing. Scalebars are 2 μm.

Once the mapping has been completed for the Rayleigh scattered light, Raman mapping has been performed for first, second, third, and fourth harmonics for both perpendicular and parallel light polarization; the same considerations made for the pattern formation of the Rayleigh mappings can be extended to the Raman signal coming from the BT-Azo molecules. Another step is required to validate this hypothesis: the dependence of the hot spot formation from the polarization of the light must be checked.

4.4.3 Hot spot localization

The Raman maps for first, second and third harmonic of the reference signal have been collected with perpendicular and parallel polarization (Figure 4.21). The Raman signal is much lower in absolute intensity than the Rayleigh signal and the signal gets lower for higher harmonics deconvolution, no matter how nonlinear the evaluated phenomenon is. For these reasons, the mapping for the fourth harmonic deconvolution doesn’t show any signal above the noise level.

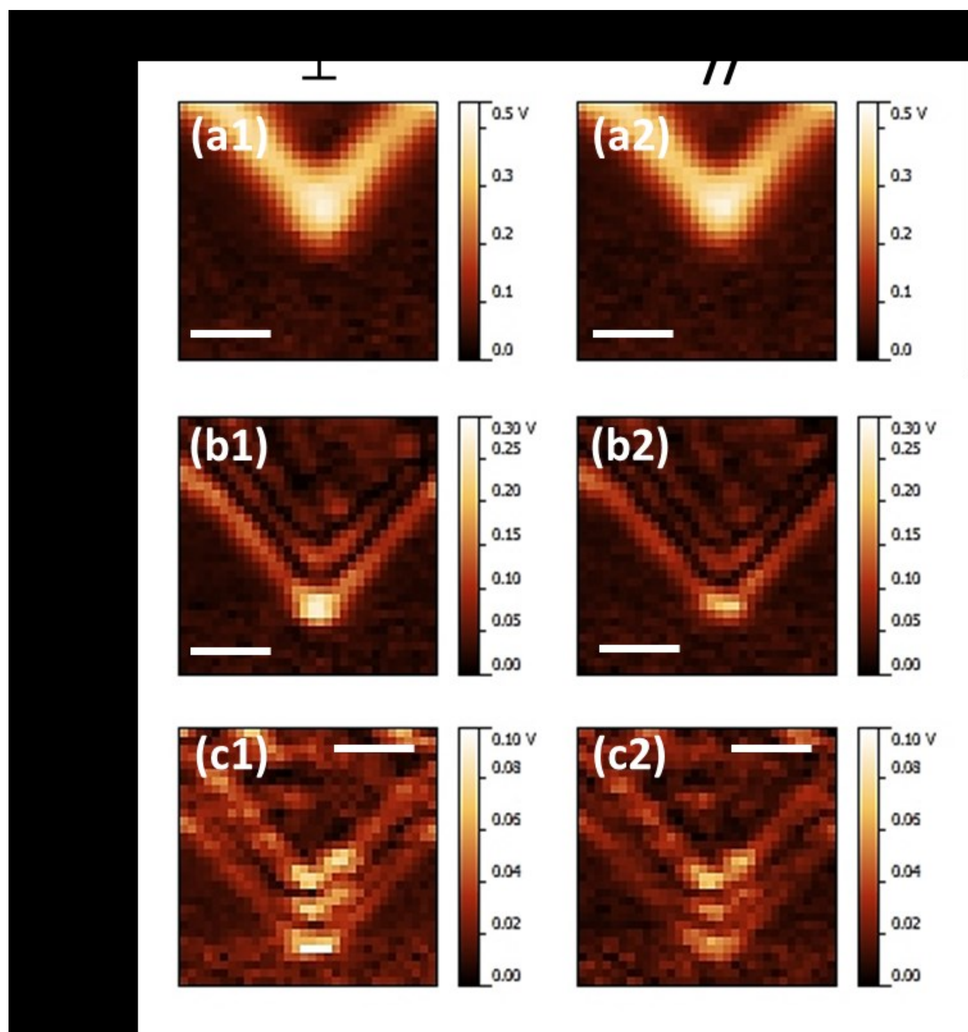

Figure 4.21 - Raman signal maps deconvoluted at higher harmonics for two orthogonal polarizations. (a1-b1-c1) perpendicular polarization maps deconvoluted at first, second, and third harmonics; (a2-b2-c2) parallel polarization maps deconvoluted at first, second, and third harmonics. Scalebars are 2 μm.

In the contact point, a higher signal can be seen for both polarizations, even if the intensity is different; the random orientation of the BT-Azo molecules on the gold surface and the intrinsic roughness of the gold layer itself can create nanometric-sized gaps which can be oriented in all directions, and partially excited by favourable light polarization components. The SERS signal from randomly placed hot spots should be in principle observable in both the perpendicular and parallel polarization mapping, and less intense than the proper hot spot formed by the tip of the cantilever and the steady wall. Arithmetic post-processing of the deconvoluted maps can give more information about the presence of the hot spot: since in principle the signal from the parallel polarization maps should be present also in the perpendicular polarization maps, which should also bring in the contribution from the hot spot, the former can be considered a background signal from which the hot spot location information can be extracted. The parallel polarization maps have been

subtracted from the perpendicular polarization ones and the ration between the two calculated; the result is visible in Figure 4.22.

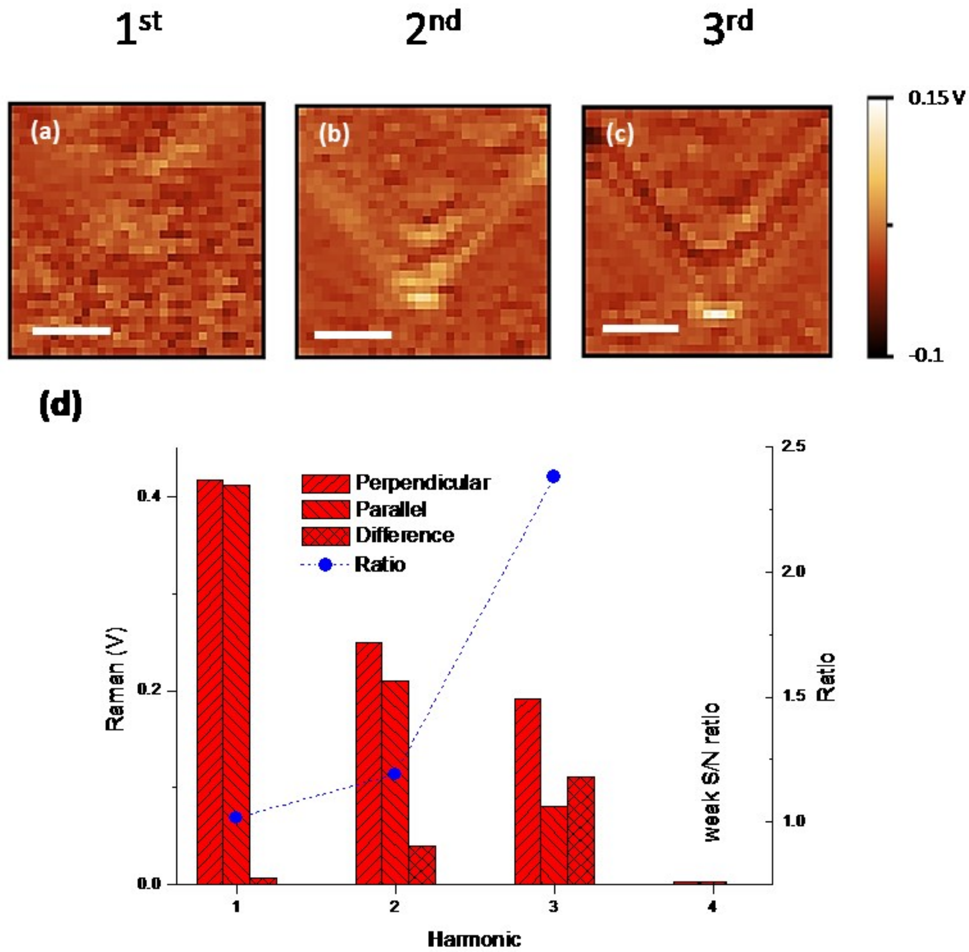

Figure 4.22 - Difference maps obtained from the subtraction of the parallel from the perpendicular mappings for first (a), second (b), and third (c) harmonics. (d) Value of the deconvoluted signal for the two orthogonal polarizations measured in the highest point (contact point); difference and ratio between the signal at the two polarizations for each harmonic deconvolution. Scale bars are 2 μm.

The graph in Figure 4.22 (d) summarizes well the results of this elaboration. The signal from the contact point increases with increasing harmonic, as already noted for separate polarization mappings, and the difference and ratio between the perpendicular and parallel polarization is higher for higher harmonics. This phenomenon can be attributed to the exponential decay of the hot spot with the distance and, while the motion of the cantilever is modulated at a single frequency, an exponential phenomenon has components at higher harmonics. The hot spot formation has been demonstrated to be exponentially dependent from the distance between the nanostructures, and the demodulation of the oscillating scattered signal at higher harmonics has the advantage of removing the scattering contribution from the sources outside the tip-wall contact point: this results in a "tip sharpening" effect, where the effective interaction that creates the

enhancement is equivalent to the hot spot generated by a tip of much smaller radius. The background signal is therefore decreased or suppressed, coming from regions much further away from the hot spot, thus increasing the contrast in the hot spot area, as already observed in literature for similar experiments[1]. The nonlinear and polarization-dependent behaviour observed and confirmed by the map subtraction confirms the presence of the plasmonic hot spot.

4.5 Signal enhancement evaluation

To estimate the enhancement factor due to the plasmonic hot spot formation, two main factors must be considered:

- The molecules exposed to the hot spot are only those in the contact point, and the number of molecules which contributes to the enhanced signal is equivalent for both perpendicular and parallel polarization mappings;
- The hot spot enhancement is confined in a region of space which can be approximated to a rectangle with dimensions corresponding to the distance at which the hot spot is formed and to the FWHM of the hot spot profile obtained from the simulations in § 4.1.2;
- The time during which the hot spot is active is only a fraction of the oscillation period.

When these two factors are considered, an estimation of the plasmonic enhancement can be made. The spatial and polarization-dependent considerations about the hot spot intensity can be summarized in an equation for a time-independent estimation of the enhancement factor:

$$E = \frac{\pi R^2}{wd}\left[\frac{I_{\perp}}{I_{\parallel}} - 1\right] \quad 4.1$$

Where E is the enhancement factor, R the radius of the laser spot (R = 412.5 nm, calculated from Equation 2.2), d is the average distance between the tip and the wall at which the hot spot can be created, w the FWHM of the enhancement in the simulated hot spot profile, $I_{\perp}$ and $I_{\parallel}$ the intensity of the Raman signal for perpendicular and parallel polarization, respectively. The result of this estimation for third harmonic maps gives the highest value of E because the ratio between the perpendicular and parallel signal intensity is higher (2.38); considering an average hot spot formation distance d of 2 nm and a hot spot enhancement profile w of 60 nm, the resulting value for E is 6148.

The timing considerations must be introduced to calculate the enhancement factor obtained only when the tip is close enough to the wall to actually create the hot spot. For this purpose, and for calculation uniformity, the time interval considered will be when the tip is within 2 nm from the steady wall. As already demonstrated in 4.3.2, the tip is in quasi-contact conditions for 1.5 μs over

the total oscillation period. Thus, if the enhancement factor is generated during that 1.5 μs and averaged over a longer interval, to calculate a time-related enhancement factor a simple modification can be done to Equation 4.1:

$$E_t = \frac{\pi R^2}{wd}\left[\frac{I_{\perp}}{I_{\parallel}} - 1\right]\frac{t_p}{t_c} \quad 4.2$$

In this final form of the equation for the enhancement factor, t_c is the time duration of the hot spot formation (1.5 μs) and t_p is the oscillation period of the devices; t_p is calculated as the inverse of the average oscillation frequency which is considered 90 kHz, so an average value of t_p is 11 μs. Introducing this modification, the enhancement factor for the same conditions already applied before is E_t = 45540, a much higher value, comparable with the results already found in literature for similar devices[6].

References

(1) Knoll, B.; Keilmann, F. Enhanced Dielectric Contrast in Scattering-Type Scanning near-Field Optical Microscopy. *Opt. Commun.* **2000**, *182* (4–6), 321–328.

(2) Naumenko, D.; Stolzer, L.; Quick, A. S.; Abt, D.; Wegener, M.; Barner-Kowollik, C.; Dal Zilio, S.; Marmiroli, B.; Amenitsch, H.; Fruk, L.; Lazzarino, M. Design of Broadband SERS Substrates by the Laser-Induced Aggregation of Gold Nanoparticles. *J. Mater. Chem. C* **2016**, *4* (25), 6152–6159.

(3) Lobontiu, N. *Dynamics of Microelectromechanical Systems*, 9th ed.; Senturia, S. D., Ed.; Microsystems; Springer US: Boston, MA, 2007; Vol. 17.

(4) McNay, G.; Eustace, D.; Smith, W. E.; Faulds, K.; Graham, D. Surface-Enhanced Raman Scattering (SERS) and Surface-Enhanced Resonance Raman Scattering (SERRS): A Review of Applications. *Appl. Spectrosc.* **2011**, *65* (8), 825–837.

(5) Graham, D.; Brown, R.; Ewen Smith, W. SERRS Detection of PNA and DNA Labelled with a Specifically Designed Benzotriazole Azo Dye. *Chem. Commun.* **2001**, No. 11, 1002–1003.

(6) Wei, H.; Xu, H. Hot Spots in Different Metal Nanostructures for Plasmon-Enhanced Raman Spectroscopy. *Nanoscale* **2013**, *5* (207890), 10794–10805.

5 Design, fabrication and characterization of nanofabricated wire scanner

In the context of micro- and nanofabrication, another project has been developed in parallel with the main research topic already presented. In this chapter, the whole process to obtain a working prototype of a sensor for the characterization of a high energetic radiation beam is presented: the fabrication and operation of a novel device manufactured using nanofabrication techniques providing several potential benefits including the potential for sub-micron resolution, lower dose rate, and compatibility with the routine operation of the acceleration facilities, in *in-operando* fashion. The basic idea is to fabricate thin bridges across a robust frame using nanofabrication techniques, to make the structures thinner and narrower than a traditional metal wire, thus achieving higher resolution. The reduced width and thickness, together with the use of materials with low atomic number, confer to our devices a dramatic reduction of their effects on the electron beam current, making it possible to run measurements during operation. This device has been tested on the BEAR beamline of Elettra Synchrotron, in collaboration with the team of the CNR-BEAR beamline, where the response to soft X-rays was evaluated, and on the FERMI free electron laser, in collaboration with the team in charge of the FEL-1 line, where the response to high energy electrons (1.2 GeV) has been measured. A crosswire configuration for 2D beam characterization has been fabricated too, and the prototype will be tested after further optimizations.

5.1 Project background

Since the development of particle accelerators, such as synchrotrons, colliders facilities, or free-electron lasers (FEL), the need to monitor the transverse dimensions of the beam has been of primary importance; a reduced beam size in a FEL guarantees low emittance (*i.e.* higher electron density in a bunch)[1], while in a collider or a synchrotron it is required to meet the desired high brightness of the beam[2]. The main instrumentation used in this context falls typically into two categories: imaging screens and wirescanners.

Scintillating screens are detectors based on the property of some materials to exhibit scintillation: when an ionizing radiation is absorbed by the screen, the scintillating material emits a photon with energy lower than that of the original radiation. The coupling of a scintillator screen with a photodetector, usually a CCD or a photomultiplier, allows the visualization of the profile of the

incident radiation beam in two dimensions, with resolution in the micron range[3]; the scintillator+photodetector system is the imaging screen. Unfortunately, even though mitigation schemes have been developed[4,5], the performances of this kind of device when subject to short and dense bunches of correlated electrons are reduced due to coherent optical transition radiation (COTR)[6], which can lower the resolution to about 10 μm[7]. The phenomenon of optical transition radiation is the emission of electromagnetic radiation in the visible range when a charged particle hits a dielectric or conducting thin surface; this effect can be used to investigate the charge distribution of an electron beam with imaging screens; when the electrons hit the screen at random time points, radiation emission is incoherent and the OTR imaging replicate the beam current distribution. However, if the electrons in the beam are temporally correlated, the beam contains well-defined spatial and temporal Fourier components, which are visualized as speckles on the beam image[8], thus reducing the performances of the imaging screens.

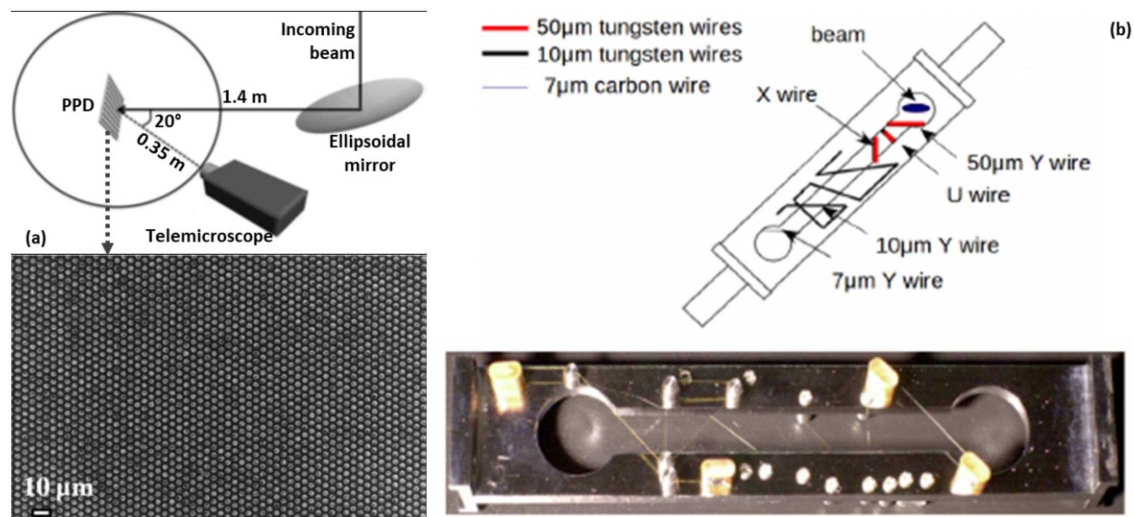

Figure 5.1 - (a) Example of focal spot monitoring with a scintillator, based on a pixelated phosphor detector. Schematics of the measurement setup (top): the beam is focused by an ellipsoidal mirror as in the regular experimental configuration of the beamline and directed towards the PPD; the luminescence of the pixels is then recorded by a telemicroscope placed in a fixed position. SEM image of the PPD (bottom) showing the regular arrangement of the phosphor-filled holes. Adapted from literature[9]. (b) Drawing and structure of a wire scanner. The wire scanners are installed with an angle of 45° to the beam line to enable the simultaneous scan in 3 axes. The X and Y wires are used for horizontal and vertical scan. The U wire, which is 45° to X and Y wire is used to measure the correlation between horizontal and vertical measurements. In addition, two 10 μ m tungsten wires with +10° and -10° tilted from X direction are used to measure the tilt angle of the beam profile. Reproduced from literature[10].

These devices can also be used for the characterization of the focal spot of a beamline in a FEL or a synchrotron; however, especially for FEL applications, damage of the luminescent material from the high intensity radiation are a serious limiting factor to the application of this technique. The recent years have seen the development of more sophisticated imaging screens, like pixelated phosphor detectors (PPD)[9]: a very recent implementation uses micrometric holes in a honeycomb

arrangement fabricated on a silicon substrate using microfabrication techniques, filled with phosphor powder and covered with Indium-Tin Oxide (ITO) to protect the phosphors and avoid leakages from the holes.
On the other hand, wirescanner sensors provide only one-dimensional information from multishot measurements, but the achievable resolution is higher. The principle behind the wirescanner sensors is the quantification of the ionizing radiation dose generated when the wires are hit by the electron beam. The combination of material and wire diameter of the wirescanners must be a compromise between high signal, high resolution, and high robustness. The latter property is required mostly to withstand the mechanical vibrations induced by the motorized stages required for the correct positioning of the sensor in the beam path, and thicker wires made of heavier, denser elements correspond to higher signal; however, this is also linked to higher emission of ionizing radiations, which may be responsible for an augmented risk of damage for electronic and magnetic equipment of the facility in the vicinity of the sensor. The need for thick and heavy wires for robustness and high signal is usually counterbalanced by the resolution requirements: it can be demonstrated[11] that the resolution of a wire sensor with diameter *d* can be at best equal to *d/4*. To reach a good compromise for practical applications, the diameter of the wire is seldom thinner than 5 µm. The same kind of detector can be used to measure the profile of the focal spot of a light beam at the end station of a beamline; the analysis chamber where the spot is focused usually doesn't contain ionizing radiations detectors, which are usually placed very distant from the sensor (in the range of tens of metres), so another method to evaluate the beam dimension must be used. Measuring the neutralization current from a conducting wire scanned across focal spot, the beam profile can be reconstructed.

5.2 Nanofabrication process of the devices

The nanobridges for the wirescanner have been fabricated using a silicon wafer coated on both sides with low stress silicon nitride (Si_3N_4) using low pressure chemical vapour deposition (LP-CVD); the thickness of the silicon is 500 µm, while the silicon nitride layers are both 2 µm thick.
The fabrication of the nanobridges requires a two-side process to obtain suspended bridges over an open window; the final dimension of the window is 3x9 mm, while the four bridges are 3 mm long and 30, 21, 14, 7, and 4 µm wide. The thicker bridges are used in the alignment of the device because they are easier to see and for the characterization of low intensity beams, while the thinner ones are used in high resolution measurements. To ensure a better alignment, the first step has been the dicing of the wafer into rectangular chips of dimension 15x9 mm, the same dimensions of the final frame. The wafer pieces have been covered with a 50 nm-thin layer of chromium using DC

sputtering coating on both sides and then spin coated with a positive tone photoresist (Megaposit SPR 220 1.2) at the speed of 3000 rpm for one minute on one side and soft baked at 115 °C for 90 s. The resulting resist layer showed good uniformity and a thickness of about 1.3 µm; the pattern of the backside is impressed upon the photoresist through exposure with UV light (wavelength of 350 nm) using a mask aligner, post-baked with the same parameters used for the soft baking, and then developed using the appropriate developer (Megaposit MF24A). The exposed sample is rinsed in DI water and dried with a clean stream of dry nitrogen.

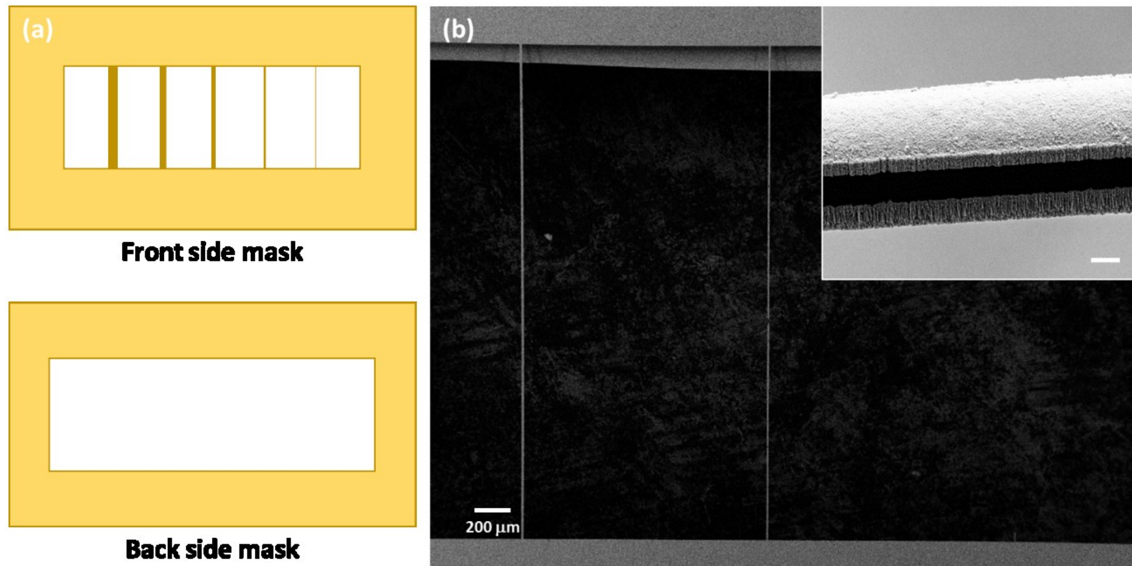

Figure 5.2 – (a) Drawing of the front and back side mask used in the fabrication of the bridges (not on scale). (b) SEM image of a parallel bridge wire scanner (scalebar: 200 µm); inset: tilted view of a bridge showing the two-side metallization (scalebar: 2 µm).

After the photolithography, the exposed chromium is wet-etched in a solution of acetic acid and sodium cerium(IV)nitrate in water (7:40:120 w/w ratios) to deprotect the silicon nitride underneath; the silicon nitride is dry-etched by reactive ion etching (RIE) with a mixture of CF_4 and oxygen, 25 and 5 sccm respectively, and a bias of 100 V, for 45 minutes. The result of this process is an open window over the silicon substrate, which is wet-etched for a depth of 450 µm in a solution of KOH 30% w/w. Since the rate of the anisotropic etching of silicon in KOH is temperature-dependent, the solution in which the samples are immersed is kept around 60 °C to ensure a reasonably constant etch rate of 25 µm/hour. The etching advancement is checked periodically every four hours using optical microscopy.

When the desired etching depth is reached, the lithographic process already described is applied on the front surface using the front side mask; silicon nitride has been dry-etched in an ICP-RIE reactor instead of RIE to further reduce the isotropy and keep the smaller bridges intact. The residual silicon is removed using HNA, a solution of hydrofluoric, nitric and acetic acid in 4:7:11 ratio. The use of HNA instead of KOH for the residual etching has been chosen due to the absence

of hydrogen bubbles formation, typical of silicon etching with KOH, that can break the thin bridges; moreover, HNA etching is isotropic, therefore a careful control of the etching time is required to remove the silicon under the bridges without excessive underetching the anchoring frame. Finally, after the removal of the silicon below the bridges, all the chromium mask is wet-etched away, leaving only silicon nitride on top of the silicon substrate. The removal of the residues of etching solutions is performed rinsing the device in ultrapure milliQ water, keeping it vertical to avoid breakage of the bridges due to the surface tension of water. A careful drying of the devices is crucial to avoid breaking the suspended structures: after rinsing in water the devices are transferred to a solution of water:ethanol 1:1, finally immersed in pure ethanol and then removed and left to dry spontaneously, always maintaining the vertical orientation of the device.

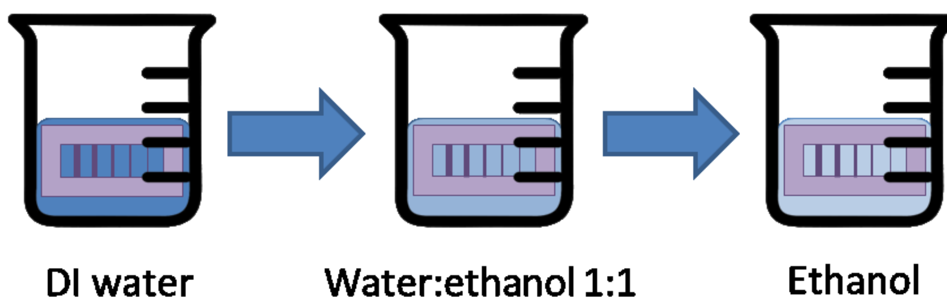

Figure 5.3 - Sketch of the three-step rinsing process before drying the samples. DI water step: required to thoroughly clean the samples; water:ethanol step: required to remove contaminated water and begin solvent replacement on the surface; ethanol step: complete replacement of the solvent over the sample surface. The vertical positioning of the device during all these steps is required to avoid breaking the bridges during the transfer from one solution to another.

This sequence of rinsing solutions has been chosen to decrease the surface tension effect on the bridges step-by-step. Water has a higher surface tension than ethanol and a lower evaporation rate, therefore the forces applied to the bridges during water evaporation are so strong that can break the structures, especially the thinner ones; on the other hand, water is the best solvent for the removal of residues of the etching solutions, so it must be used for the first rinsing. The intermediate step of immersion in 1:1 water:ethanol solution helps in the replacement of the water from the silicon nitride, and this process is completed during the last immersion in pure ethanol. The complete drying of the samples after this last step can be achieved without breaking the bridges, due to the lower surface tension and boiling point of ethanol. During the whole process, the device must be kept with the bridges aligned vertically, since the surface tension in the first steps can damage them during the crossing of the water-air interface.

To increase the ionization cross section of the as-fabricated bridges, which are made only of S_3N_4, we added a metal layer on both sides: different metals with different thicknesses (200 nm chromium, 200 or 500 nm silver, or 50 nm platinum, depending on the application) have been

evaporated on both sides of the bridges in ultra-high vacuum. The layer of metal has been deposited on both sides of the bridges to reduce the stress induced by the additional material. The final result is shown in Figure 5.4 (b), where it is possible to appreciate the high aspect ratio of the suspended bridges and the double-sided metal coating.

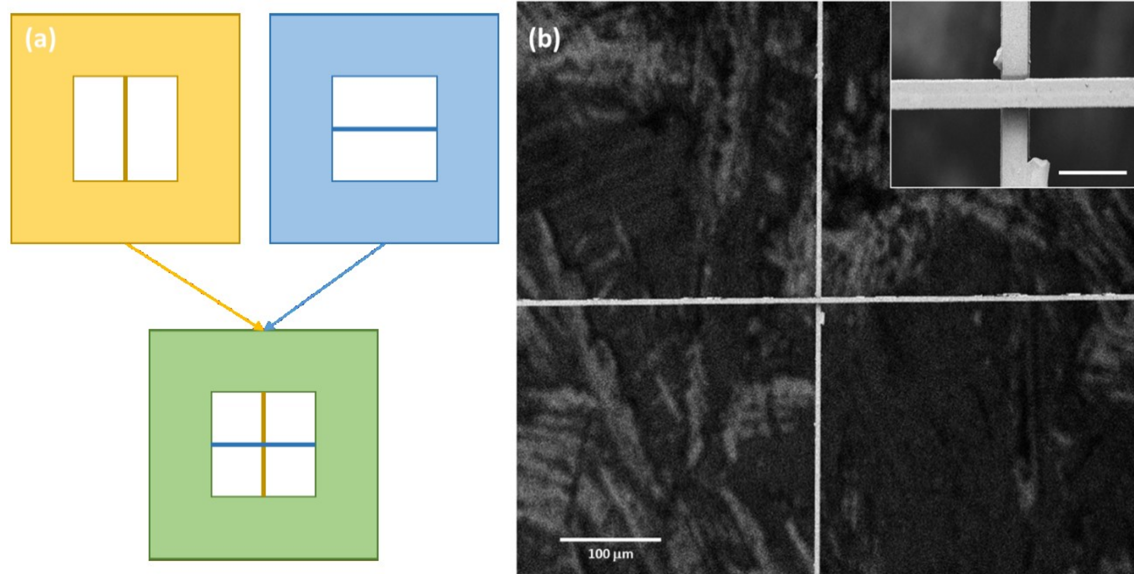

Figure 5.4 - (a) Drawing of the two-frames fabrication of the crossbridge scanner: the two identical frames with the single bridge are rotated until the two bridges are perpendicular and then placed upon each other. (b) SEM image of a crosswire scanner (scalebar: 100 µm); inset: detail of the centre of the cross (scalebar: 10 µm).

A first prototype of the device in crosswire configuration has also been fabricated (Figure 5.4 (b)); the same process used for the realization of the suspended bridges has been used to fabricate two identical, separate frames with one bridge 5 µm wide across the centre of a square window each. After the metal evaporation, the two square windows have been stacked with the bridges perpendicular to each other to obtain the final crosswire configuration. The choice of overlapping two bridges instead of directly fabricating a cross is due to functional reasons. The different focal plane of the bridges, that could be further increased with the insertion of a spacer between the two chips, allows the focusing of the beam on the two bridges separately; moreover, if they are fabricated on physically different chips it could be easier to contact the chips independently in order to measure the signal coming from each bridge separately, thus allowing the characterization of the vertical and horizontal dimension of the focal spot with a single exposure. The development of this new kind of 2D sensor is still in progress and therefore no functional test has been done yet.

5.3 Intra-undulator chamber measurements at FERMI Free-Electron Laser

The prototype of the nanofabricated wire scanner with multiple suspended bridges has been tested inside the undulator chamber of the FEL1

5.3.1 *Simulations of ionizing radiation emission*

An important parameter for the evaluation of the device ability to be used under normal operation conditions is the evaluation of the amount of ionizing radiation generated by the device; to estimate this parameter, a simulation with the Monte Carlo particle tracking code Fluka[12,13] has been performed to compare the radiation field created by the different wire shapes in a FEL beam profile measurement. The simulation contains exclusively electromagnetic interactions and tracks electrons and positrons down to a kinetic energy of 20 keV, and photons down to 5 keV. The simulated electron beam has a Gaussian profile of radius 50 µm and no divergence. It hits the wire centrally at $z = 0$. For the sake of simplicity, the rest of the simulation space is empty (vacuum). The target configurations of choice are: tungsten wire, 10 µm diameter, aluminium wire, 5 µm diameter, silicon nitride bridge, 10 µm width and 2 µm thickness, silver/silicon nitride/silver nitride bridge, 10 µm width and 0.5/2/0.5 µm thickness.

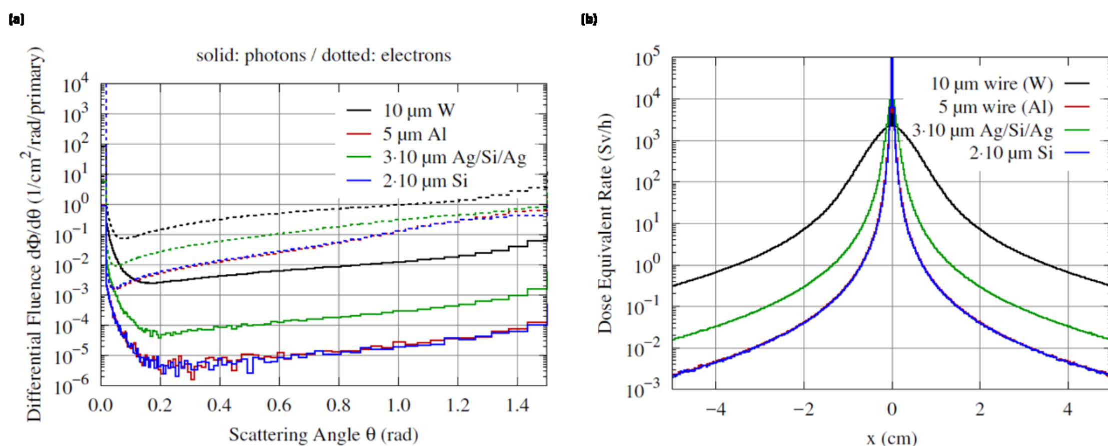

Figure 5.5 – (a) Differential fluence calculated as a function of the scattering angle for photons (solid lines) and electrons (dotted lines) hitting the chosen targets. (b) Calculated cross-sectional distribution of the dose rate on a perpendicular plane 10 m away from the target for the chosen configurations.

The simulations have been useful to gain information about the performances of the devices under different conditions. The differential fluence of ionizing radiation for the chosen devices has been simulated for photons and electrons as a function of the scattering angle; the results are shown in Figure 5.5 (a), underlining a higher fluence for electrons than photons of a few orders of magnitude.

The cross-sectional distribution of the equivalent dose delivered in a plane perpendicular to the beam direction, placed at a distance of 10 m from the device, has also been evaluated; the predicted dose for the 5 µm aluminium wire and the 2 µm silicon nitride bridge are almost the same, while the Ag/silicon nitride/Ag bridge has a predicted dose 7.5 times higher and the 10 µm tungsten wire 175 times higher.

5.3.2 Experimental setup

The experiments at the FERMI FEL have been performed in the fourth intra undulator chamber of the FEL1 undulator chain, in correspondence with the imaging screen already in place in that section to compare the performances of the new device with an already existing one.

The main reason for this choice is the availability of a motorized actuator fitted with independent optical encoder for wire scanning and the availability of ionizing radiation detectors. Moreover, both the high energy and the low beta optics in this machine position produce electron beam of the order of 100 µm that are ideal for the measurements; finally, the chosen location was also suitable for an initial evaluation of compatibility of such a device with the operation of the accelerator for what concerns the damage to the undulators. During the experiment, the FERMI beam charge was 700 pC, and the energy 1.285 GeV, with a repetition rate of 10 Hz. Figure 5.6 shows a schematic layout of the FERMI FEL1[14] area involved in the experiment. The ionizing radiation detectors installed in the FEL region are of two types: Cherenkov fibers and ionization chambers, which are part of the machine protection system (MPS) of FERMI[15] and have been used as measurement devices. The Cherenkov fibers run along the entire undulator vacuum chamber. The light produced by high energy particles hitting the fiber is transferred out of the tunnel to an optical to electrical conversion unit based on MPPC detector. The electrical signal is then acquired by means of a VME ADC board with 12 bits resolution and 250 Msample/s sampling rate.

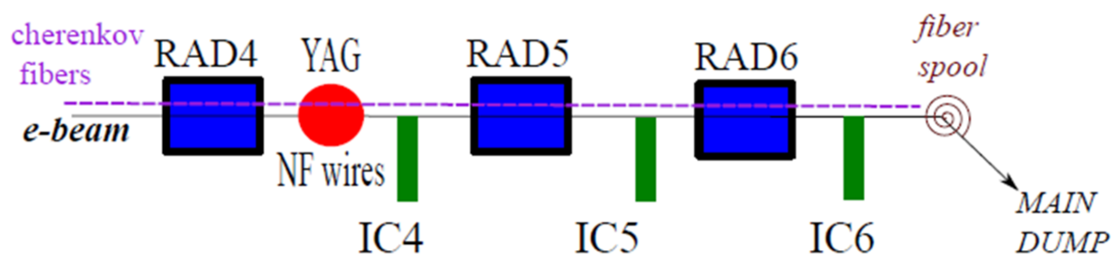

Figure 5.6 - Schematic drawing of the experimental layout along the FEL1 undulators (blue rectangles). The ionization chambers (green rectangles) follow the corresponding undulators and the Cherenkov fibers (purple dashed line) are placed along the whole path of the beam considered in the experiment, terminated by an additional fiber spool. The experimental chamber, where the scintillator (YAG) and the wire scanner (NF wires) are placed is depicted as a red circle between the RAD4 undulator and the IC4 ionization chamber.

The ionization chambers are installed in the vicinity of each imaging screen chamber. The ionization chambers are filled with air at atmospheric pressure and connected to the controller which supplies the high voltage (1 kV) and acquires the signal via an embedded picoamperometer. As an addition for the experiment, a spool of Cherenkov fibres has been placed at about 12 meters downstream of the device under test.

5.3.3 Experimental results

The signal generated in the ionization chambers by the ionizing radiations induced by the nanofabricated wires is rather small and, in some conditions, could be comparable to the background noise. To obtain the best signal-to-noise ratio, both optics and trajectory in FEL1 have been optimized, to avoid any beam losses which would cause lower signal and a background in the measurements. Considering a vertical beam size of 100 µm means that the vertical aperture of 3 mm is about 30 times the vertical size, so no core electrons are expected to contribute to the background. On the other side, vertical halos due to wakefields may become relevant: the signal from the halos can potentially become of the same magnitude of the one produced by a 10 µm wire if the halo size is so large to hit the frame. During the measurements, the suppression of the contribution from the halos has been monitored. Figure 5.7 (a) shows the beam losses signal measured by the Cherenkov fibers, while scanning the nanofabricated wires position with a step of about 25 µm. The scanning step was chosen in relationship with the expected beam spot size of few hundred microns. Each data point plotted in the figure corresponds to the average over five consecutive shots and the error bars are the standard deviation.
Figure 5.7 (b) shows the beam losses signal measured by the Ionization Chambers IC4, IC5 and IC6. The different signal amplitudes derived from each wire depend only on the width of the wires. The IC6 and the fiber spool signal have a comparable SNR which is better than the other detector. The difference in the relative amplitude of the ionization chambers depends on the position of the chamber with respect to the NF wire which is located in the same position of IC4. IC5, which is located 3.7 meters downstream of the wires, shows a detectable signal but the IC6, which is located at 7.4 meters, shows the largest signal. This is consistent with the expected angular divergence for such a low cross section target. This behaviour is also confirmed looking at the dose amplitude versus distance from impact point.

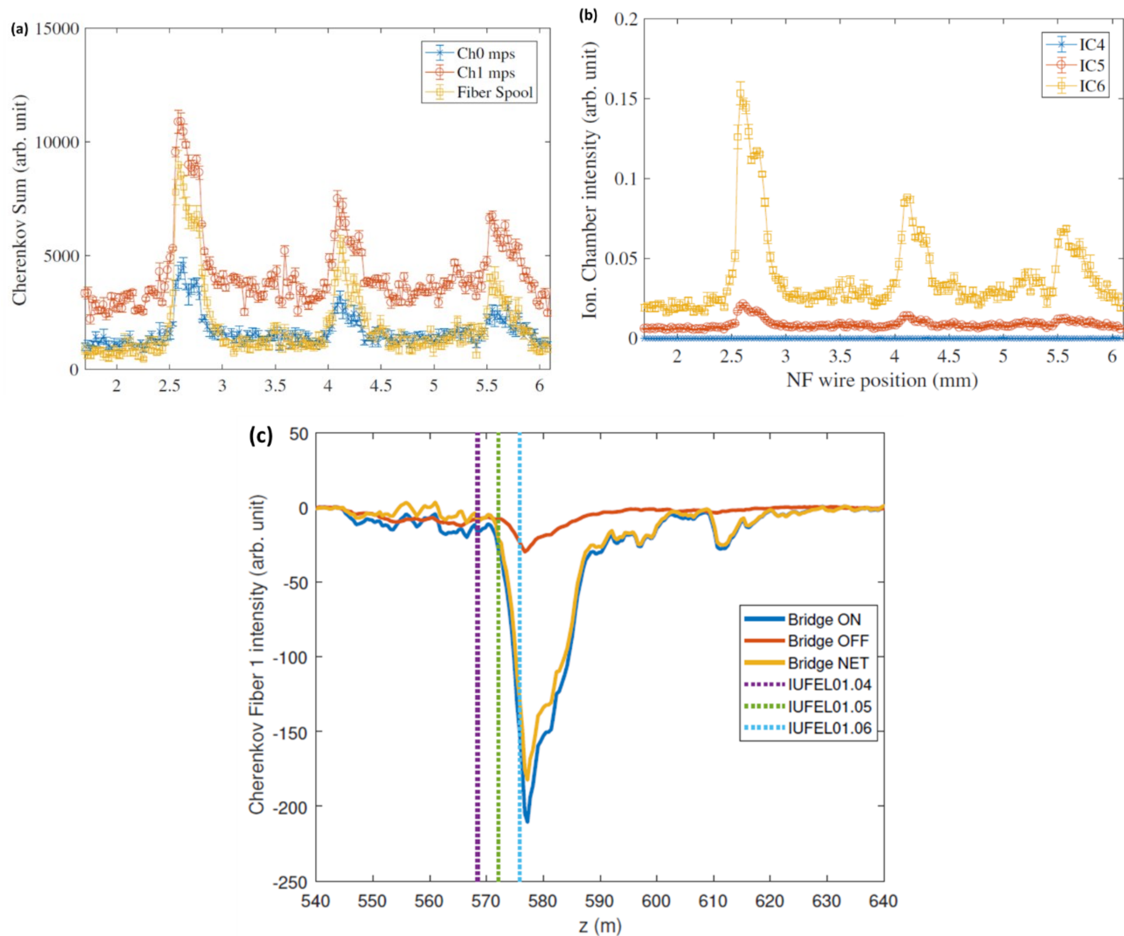

Figure 5.7 – (a) Beam losses measured by the Cherenkov fibers during wire scanner operation for two Cherenkov fibers (Ch0, blue and Ch1, red) and the additional fiber spool (yellow). Horizontal step is 25 µm and each point is the average of five consecutive shots. Error bars for standard deviation. (b) Beam losses measured by the ionization chambers: IC4 (blue), IC5 (red), IC6 (yellow) during wire scanner operation. Horizontal step is 25 µm and each point is the average of five consecutive shots. Error bars for standard deviation. (c) Dose amplitude from the Cherenkov fiber Ch1 along the whole beam path across the FEL1 undulators; the dotted lines depict the position of the ionization chambers. Blue line: dose with bridge on path; red line: dose with bridge off path; yellow line: difference between the two.

The Cherenkov fiber signal is plotted in Figure 5.7 (c) as a function of distance, considering the electron beam traveling from left to right. The location of IC4, IC5 and IC6 is shown as vertical dotted lines. The ionization chambers relative intensities are in agreement with the fiber signal versus distance.

To verify the profile measured with the nanofabricated device, the results of the test have been compared with a typical acquisition performed with the imaging high resolution scintillating screen. These imaging screens employ a COTR-immune detection geometry and they are capable of measuring beam sizes down to 15 µm[4]. The horizontal profile of the electron beam measured by the scintillating screen and by scanning the of 13.5 µm wide nanofabricated wire, averaging step by step over 20 consecutive shots, are compared in Figure 5.8.

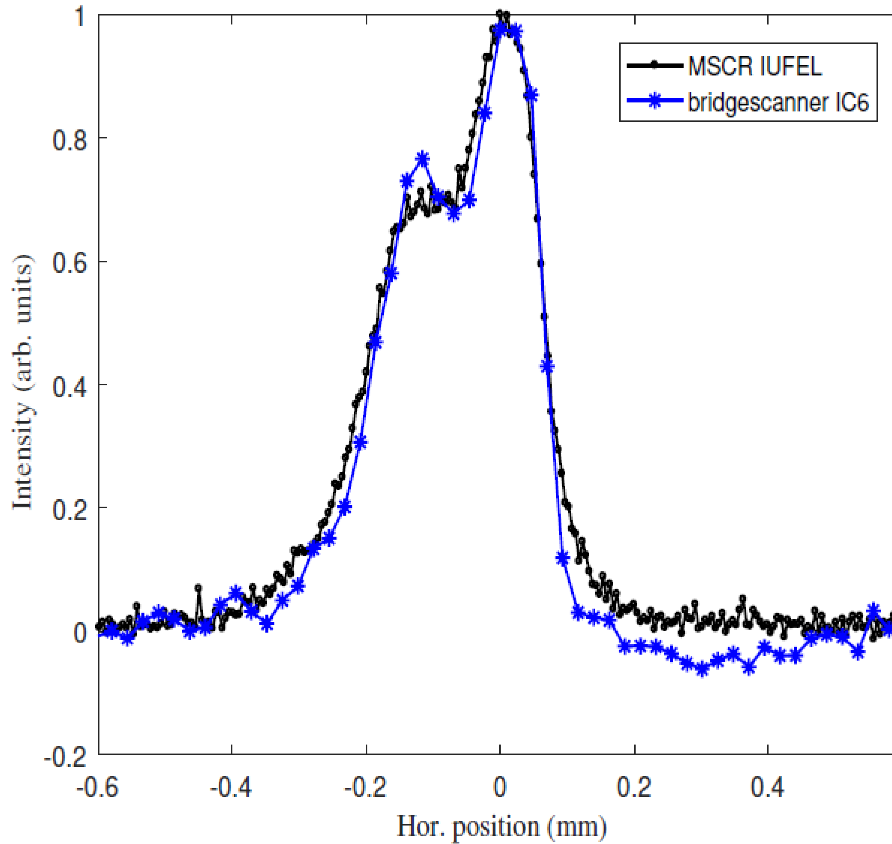

Figure 5.8 - Horizontal beam profile obtained with the 13.5 µm wide nanofabricated bridges (averaged multi-shot measurement), compared with the beam profile as measured by the imaging screen (single-shot measurement).

Despite being the former a single shot acquisition and the latter a multi-shot one, the two plotted profiles are in well agreement. Moreover, one can observe that both methods are able to detect the double peak in the horizontal projection, likely due to a residual transverse wakefield effect.
It is worth remarking that the dose rate of ionizing radiations generated during the measurement with the nanofabricated wire scanner is well below the threshold fixed by the machine protection, allowing a measurement of the beam profile without interfering in the FEL routine operation.

5.4 Focal spot characterization at BEAR beamline

5.4.1 Experimental setup

The experiments in the BEAR beamline of Elettra Synchrotron concern the characterization of the focal spot of a EUV beam in the experimental chamber, after all the extraction, polarization, and focalization chain of the beamline. The beam spot size has been characterized using the silver-coated Si_3Ni_4 wires, supported by a silicon frame. The frame containing the wires has been mounted on the sample holder and put in the center of the experimental chamber; a clamp perpendicular to

the sample holder has been mounted to allow two-dimensional movement of the wire scanner, either in the vertical direction or inside and outside the focal plane.

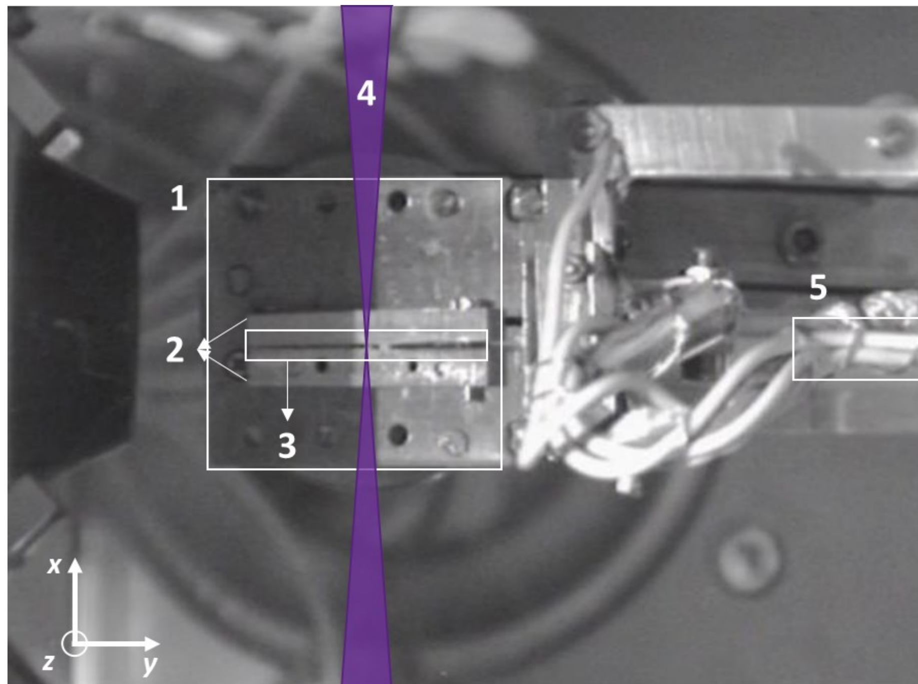

Figure 5.9 - Photograph of the wire scanner mounted inside the sample chamber of the BEAR beamline. 1) sample holder; 2) sample clamp; 3) wire scanner (perpendicular to the image plane); 4) deep UV/soft X-rays incident beam; 5) wires connecting the sample holder to a picoamperometer for the photocurrent measurement. The focal spot has been characterized in the z direction (perpendicular to the image plane).

The sample and its holder are electrically isolated from mass and connected to ground through a Keithley model 6517A picoamperemeter, allowing the measurement of the neutralization current generated by the photoelectron emission of the metal-coated bridges during the scan. With respect to the experiments in the FEL undulators, here the metal coating is required to generate the photoelectrons instead of the ionizing radiations.

5.4.2 Experimental results

The characterization of the focal spot of the EUV/soft X-rays beam of the beamline has been performed measuring the neutralization current of the wires, coated with a metal layer to ensure photoelectron emission. When a photon hits a metallic electrode with the appropriate energy, it can transfer its energy to an electron in the conduction band; this electron is emitted from the metal, thus creating a vacancy in the material which, if the metal sample is connected to ground, is filled by another electron coming from the ground connection. The flow of electrons filling up the vacancies is called neutralization current and is equivalent to the direct photocurrent generated by the photoelectric effect. During a scan, the wire is exposed to a growing section of the beam: since

the photoelectric effect (and thus the neutralization current) is proportional to the integral of the beam spot section hitting the sample, the measured current can be used to reconstruct the beam profile. The vertical size of the beam spot has been measured by scanning along the *z* axis (vertical) the wire scanner, mounted to align the bridges along the horizontal direction (*y* axis in Figure 5.9). The exit slits, placed along the beam path before the focusing mirror and used to adjust the beam dimensions, have been set at 120x5 μm^2 (HxV). Using narrower vertical slits didn't give better results, due to diffraction limits. The measurements have been done at 130, 600, and 1000 eV, the most common values for experimental purposes, well within the utilization range of the beamline. The measurements for each chosen energy have been performed scanning the smallest of the fabricated wires, 4 µm wide, with a step of 25 µm. The results are illustrated in Figure 5.10.

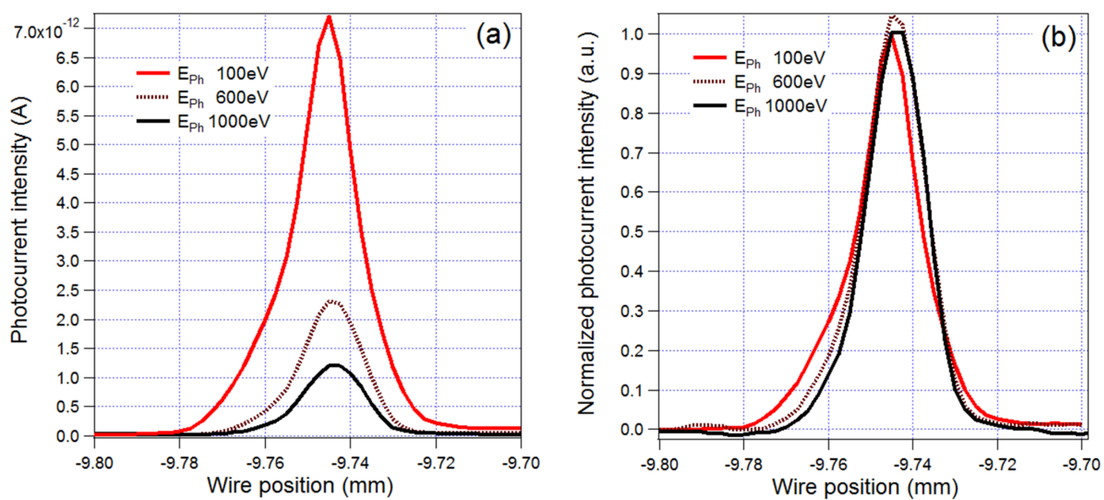

Figure 5.10 - Absolute (a) and normalized (b) photocurrent measurements at different photon beam energies: 100 eV (red curves), 600 eV (purple dotted curves), and 1000 eV (black curves). While the beam profile seems dependent from the photon energy in (a), the normalization reveals an energy-independent vertical beam profile.

The measurements taken at three different energies confirm that the focal spot vertical dimension is energy-independent for fixed vertical slit aperture; the vertical dimension of the beam calculated from the FWHM of the three curves is 16.8±0.2 µm. An additional characterization of the vertical beam profile with two beam energies has been performed moving the wire along the beam propagation direction (the *x* axis in Figure 5.9) to characterize the beam inside and outside the focal spot.

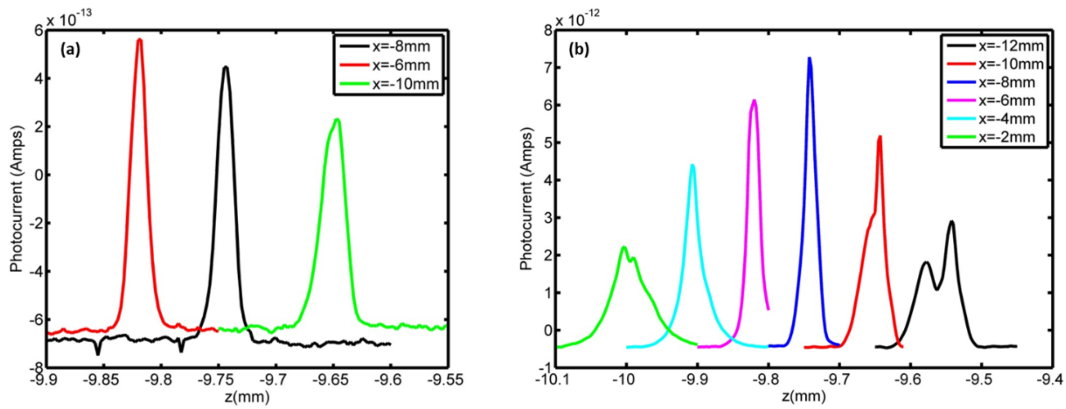

Figure 5.11 - Vertical profile of the beam measured along the beam propagation direction at two different energies. (a) Vertical profile obtained at 1000 eV for three different x positions: -6 mm (red line), -8 mm (black line), and -10 mm (green line). (b) Vertical profile obtained at 100 eV in six different x locations: -2 mm (green line), -4 mm (cyan line), -6 mm (magenta line), -8 mm (blue line), -10 mm (red line), and -12 mm (black line). The focal point for the beam of both energies is at -7 mm on the x axis.

The measurements taken for the beam of energy 1000 eV show that the beam has a narrow distribution of the signal also outside the focal spot location (Figure 5.11 (a)). In Figure 5.11 (b) the same experiment has been performed on six different positions along the *x* axis at 100 eV, confirming the narrow vertical dimension of the beam. Moreover, with this last measurement it is possible to reconstruct the profile of the beam along the propagation direction and the results are compatible with those calculated from theoretical data, thus confirming the good quality of the measurements performed with this sensor. From the results obtained in the most out-of-focus positions (green and black curve in Figure 5.11 (b)) it is possible to appreciate the double-peak configuration typical of the sum of S- and P-polarized electric field, a beam profile qualitatively similar to those calculated from theoretical models. The results of these experiments have been obtained with a very small slit aperture, that is the beamline configuration for high resolution; the performances of the wire scanner are good enough to characterize the beam in this condition and thus would be able to perform the same analysis on lower resolution configurations.

A final test of the nanofabricated wire scanner performances has been carried out measuring the vertical profile of the beam in the focal point for different apertures of the exit slit; the height of the slit is linked to the vertical dimension of the beam and thus the achievable resolution of the measurements. The beam characterization has been successful and the variations in the vertical dimension of the beam in the focal point are compatible with the variation of the slit aperture.

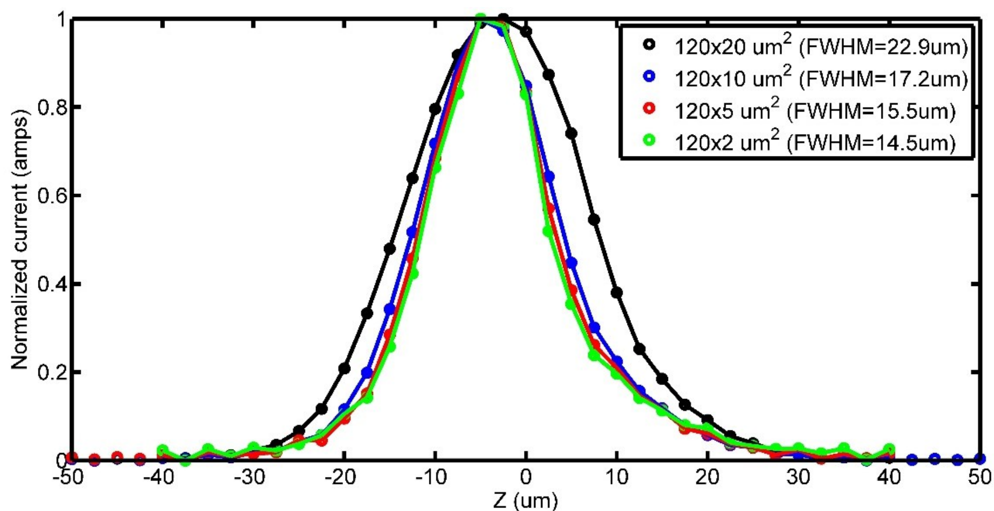

Figure 5.12 - Vertical beam profile as a function of the exit slit aperture. The slit aperture has been varied in height only, from 20 to 2 µm. The full width-half maximum (FWHM) for each measurement profile has been evaluated before the numerical deconvolution.

On these measurements, a numerical deconvolution in the Fourier space has been performed to take into account the size of the wire. The analytical deconvolution of the experimental data could have been possible if the spatial frequency between the data points had been appropriate but, since the bridge width (4 µm) is smaller than the scan step (25 µm), a numerical method with equispaced points has been implemented. The steps are of this algorithm are:

- Interpolate the data points with a third-order polynomial in the sampling range and zero elsewhere;
- Resample the interpolated curve at higher spatial frequency (0.5 µm);
- Apply the discrete Fourier transform (DFT) to the resampled data points;
- Generate a succession with the same spatial frequency of the resampled data (0.5 µm) of zeros only, except in the middle, where a succession of ones matching the width of the bridge represents the bridge itself (9 points in our case, corresponding to a width of 4 µm);
- Calculate the ratio of the DFTs (data points by bridge) and inverse-transform the result from the Fourier space;
- Replot the obtained data in the correct order to reconstruct the beam profile.

With the appropriate scaling, the obtained curve represents the bridge-independent beam profile.

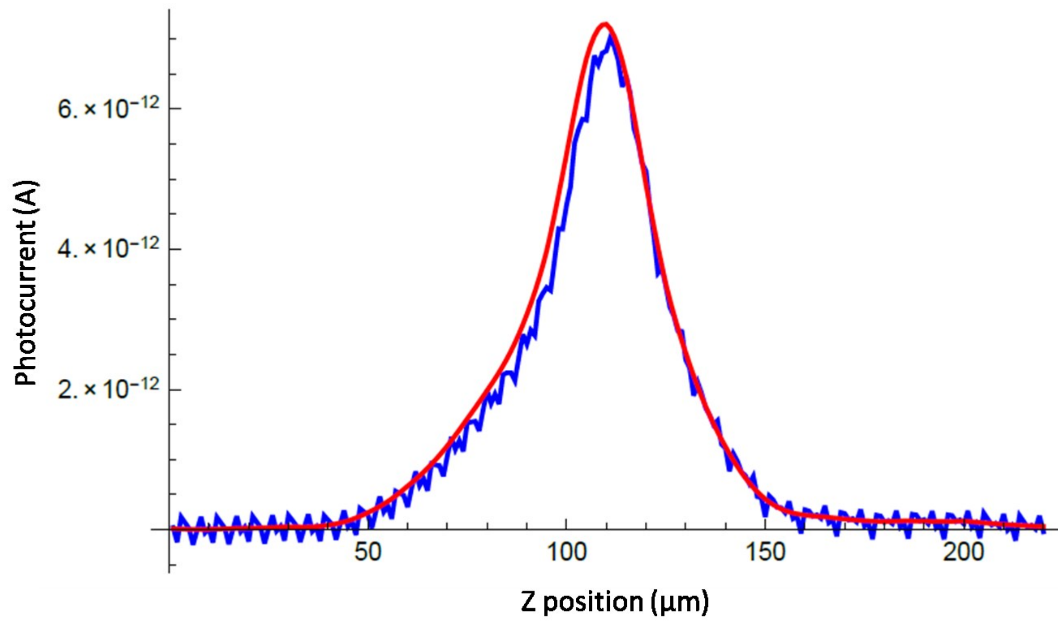

Figure 5.13 - Comparison between the interpolation of the experimental data points (red curve) and the result of the Fourier space deconvolution plotted in the real space (blue curve).

The vertical dimension of the beam calculated with this method has been evaluated to be 13.6 µm for a slit aperture of 2 µm, pushing the applicability of this sensor to the characterization of the beam usually employed in higher resolution measurements.

References

(1) Hemsing, E.; Stupakov, G.; Xiang, D.; Zholents, A. Beam by Design: Laser Manipulation of Electrons in Modern Accelerators. *Rev. Mod. Phys.* **2014**, *86* (3), 897–941.

(2) Lefèvre, P.; Petterson, T. The Large Hadron Collider Conceptual Design. Geneva 1995, p 223.

(3) Ross, M. Very High Resolution Optical Transition Radiation Beam Profile Monitor. In *AIP Conference Proceedings*; AIP, 2002; Vol. 648, pp 237–247.

(4) Veronese, M.; Abrami, A.; Allaria, E.; Bossi, M.; Bucconi M De Marco, A.; Frolich, L.; Ferianis, M.; Giannessi, L.; Grulja, S.; Sauro, R.; Spezzani, C.; Tudor, M.; Borden, T.; Cianciosi, F. Intra Undulator Screen Diagnostic for the FERMI@Elettra FEL. In *Proceedings of IBIC2012, Tsukuba, Japan*; 2012; pp 519–523.

(5) Ischebeck, R.; Prat, E.; Thominet, V.; Ozkan Loch, C. Transverse Profile Imager for Ultrabright Electron Beams. *Phys. Rev. Spec. Top. - Accel. Beams* **2015**, *18* (8), 1–9.

(6) Akre, R.; Dowell, D.; Emma, P.; Frisch, J.; Gilevich, S.; Hays, G.; Hering, P.; Iverson, R.; Limborg-Deprey, C.; Loos, H.; Miahnahri, A.; Schmerge, J.; Turner, J.; Welch, J.; White, W.; Wu, J. Commissioning the Linac Coherent Light Source Injector. *Phys. Rev. Spec. Top. - Accel. Beams* **2008**, *11* (3), 1–20.

(7) Yan, M.; Behrens, C.; Gerth, C.; Kube, G.; Schmidt, B.; Wesch, S. Suppression of Coherent Optical Transition Radiation in Transverse Beam Diagnostics by Utilising a Scintillation Screen with a Fast Gated CCD Camera. *Proc. DIPAC2011, Hamburg, Ger.* **2011**, 440–442.

(8) Nause, A.; Gover, A. *Exact Theory of Optical Transition Radiation (OTR) and Coherent OTR*; 2010.

(9) Matruglio, A.; Dal Zilio, S.; Sergo, R.; Mincigrucci, R.; Svetina, C.; Principi, E.; Mahne, N.; Raimondi, L.; Turchet, A.; Masciovecchio, C.; Lazzarino, M.; Cautero, G.; Zangrando, M. A Novel Approach in the Free-Electron Laser Diagnosis Based on a Pixelated Phosphor Detector. *J. Synchrotron Radiat.* **2016**, *23*, 29–34.

(10) Liu, S.; Bambade, P.; Faus-Golfe, A.; Fusster-Martinez, N.; Bai, S.; Gao, J.; Wang, D.; Tauchi, T.; Terunuma, N. Beam Halo Measurements Using Wire Scanners at ATF2. In *5th International Particle Accelerator Conference IPAC'14, Jun 2014, Dresden, Germany*; 2014.

(11) Orlandi, G. L.; Heimgartner, P.; Ischebeck, R.; Loch, C. O.; Trovati, S. Design and Experimental Tests of Free Electron Laser Wire Scanners. **2016**, *92802*, 1–16.

(12) Ferrari, A.; Sala, P. R.; Fassò, A.; Ranft, J. Fluka: A Multi-Particle Transport Code. 2011, p 464.

(13) Böhlen, T. T.; Cerutti, F.; Chin, M. P. W.; Fassò, A.; Ferrari, A.; Ortega, P. G.; Mairani, A.; Sala, P. R.; Smirnov, G.; Vlachoudis, V. The FLUKA Code: Developments and Challenges for High

Energy and Medical Applications. *Nucl. Data Sheets* **2014**, *120*, 211–214.

(14) Allaria, E.; Appio, R.; Badano, L.; Barletta, W. A.; Bassanese, S.; Biedron, S. G.; Borga, A.; Busetto, E.; Castronovo, D.; Cinquegrana, P.; Cleva, S.; Cocco, D.; Cornacchia, M.; Craievich, P.; Cudin, I.; D'Auria, G.; Dal Forno, M.; Danailov, M. B.; De Monte, R.; De Ninno, G.; Delgiusto, P.; Demidovich, A.; Di Mitri, S.; Diviacco, B.; Fabris, A.; Fabris, R.; Fawley, W.; Ferianis, M.; Ferrari, E.; Ferry, S.; Froehlich, L.; Furlan, P.; Gaio, G.; Gelmetti, F.; Giannessi, L.; Giannini, M.; Gobessi, R.; Ivanov, R.; Karantzoulis, E.; Lonza, M.; Lutman, A.; Mahieu, B.; Milloch, M.; Milton, S. V.; Musardo, M.; Nikolov, I.; Noe, S.; Parmigiani, F.; Penco, G.; Petronio, M.; Pivetta, L.; Predonzani, M.; Rossi, F.; Rumiz, L.; Salom, A.; Scafuri, C.; Serpico, C.; Sigalotti, P.; Spampinati, S.; Spezzani, C.; Svandrlik, M.; Svetina, C.; Tazzari, S.; Trovo, M.; Umer, R.; Vascotto, A.; Veronese, M.; Visintini, R.; Zaccaria, M.; Zangrando, D.; Zangrando, M. Highly Coherent and Stable Pulses from the FERMI Seeded Free-Electron Laser in the Extreme Ultraviolet. *Nat. Photonics* **2012**, *6* (10), 699–704.

(15) Fröhlich, L.; Cautero, G.; Giuressi, D.; Menk, R. H.; Trieste, S.; Giovenale, D. Di. The Machine Protection System for Fermi @ Elettra Introduction. In *Proceedings of FEL2010, Malmö, Sweden*; 2010; pp 667–670.

Conclusions

The objective of this project has been the design, fabrication and characterization of an optomechanical system for the realization of frequency-modulated plasmonic hot spots to achieve a switchable enhancement of SERS analysis.

The first part of the project takes advantage of a class of devices developed and thoroughly studied in our laboratories: pillar micro resonators. By fabricating a steady structure very close to the oscillating pillar, an impact oscillator was obtained that was then exploited for the realization of a localized SERS hot spot. To this purpose the surfaces where coated with a plasmonic active material and a Raman-active molecule was deposited. A combination of e-beam lithography and an optimized dry etching process have been used successfully in the fabrication of the devices, which has demonstrated the required aspect ratio and inverted tapered structure. The expected mechanical behaviour has been demonstrated using the optical lever method both in vacuum, where the onset of the impact oscillator condition has been observed and discussed, and in air. The Raman enhancement has been observed in specific locations along the line where the hot spot formation was expected and thus a plasmonic enhancement factor has been calculated, thus demonstrating the validity of this approach. However, since some issues evidenced during the characterization of this device appear to be limiting its performances, a new device has been designed from scratch, taking advantage of the know-how already developed for and with the first class of devices.

The second part of the project has been dedicated to the design, fabrication and characterization of a novel structure, based on a vertically-oriented cantilever equipped with a tip; this new geometry has been engineered with the aid of finite element modelling to investigate its mechanical and plasmonic properties in order to optimize the main geometrical parameters. The fabrication, carried out using the same well-established approach used in the previous device, has been successful and the functionalization of the plasmon-active top surface has been obtained with a synthetic dye molecule, BT-Azo, specifically designed for resonant SERS experiments: we decided to exploit the resonant condition of the Raman dye because it has proved to be useful in literature for the characterization of SERS substrates. The combination of sample scanning confocal microscopy mapping of the region of interest, where the enhancement was expected to happen, with the lock-in deconvolution of the scattered light signal at different harmonics has allowed the visualization of the hot spot location and the estimation of an enhancement factor for third harmonic demodulation, thus demonstrating the first reported realization of a frequency-

modulated, switchable, optomechanical SERS device. Further perspectives of this project will include the characterization of different molecules, either in resonant or non-resonant Raman condition, first with other Raman dyes and then with common use molecules, towards the investigation of unknown samples. The addition to our instrumentation of an acousto-optical modulator that can modulate the laser in a frequency range compatible with the resonance of the cantilever is in progress: in principle, with this device it is possible to concentrate the highest energy deposited on the sample only during the fraction of period in which the hot spot is created, thus decreasing the light-induced damages to the molecules on the device without decreasing the Raman enhancement factor.

The know-how developed in micro and nanofabrication of MEMS, in course of my PhD period, was employed also to tackle and successfully solve several issues, which were however not strictly related to Raman spectroscopy. In the last chapter, one of these activities is described, chosen for its completeness: the fabrication and characterization of a wire scanner sensor based on metal-coated microbridges suspended across a very wide window. The fabrication of the wire scanner has been performed in the clean room facilities of the CNR-IOM, while the experimental part of this work has been performed in collaboration with the team of the CNR-BEAR beamline at the BEAR beamline of Elettra Synchrotron and the group in charge of the FEL-1 line at the FERMI Free-Electron Laser facility. The performances of the nanofabricated bridge scanner for the characterization of electron or deep UV beams have been demonstrated to be better than those of similar, commercially available wire scanners. In the FEL experiments, a lower emission of ionizing radiation while keeping the resolution intact has been demonstrated, thus opening the way to the beam characterization during normal operation, directly in the undulator section, without damaging the magnetic and electronic equipment. The experiments at the BEAR beamline, concerning the characterization of the vertical distribution of the EUV beam focal spot, proved that the performances of the nanofabricated bridges of this wire scanner are so high that, with the appropriate post-processing of the signal, it is possible to characterize the beam in the focal spot with very high resolution, with the capacity of measuring a beam profile with a theoretical dimension of less than 4 μm, smaller than the width of the bridge itself. The project is still in progress, and a new version of the device for simultaneous 2D measurement is under development in our clean room facilities. More steps towards the realization of an optimized wire scanner sensor include the realization of thinner bridges, to push the resolution to even lower values, and the completion of the cross-bridge scanner for simultaneous 2D measurements.